Inductively Coupled Corrosion Potential Sensor for Remote Passive Monitoring of New and Existing Civil Structures

by

Khalada Perveen

A Thesis submitted to the Faculty of Graduate Studies of

The University of Manitoba

in partial fulfillment of the requirements of the degree of

Master of Science

Department of Electrical and Computer Engineering

University of Manitoba

Winnipeg

Abstract

The thesis describes development and optimization process of an inductively coupled coil corrosion potential sensor for long-term civil structure health monitoring remotely. This is of growing interest for decreasing the maintenance cost, reducing the deterioration significantly and increasing the safety. The thesis is organized accordingly introduction, circuit modeling of the sensor, optimization and fabrication of the sensors and the simulated and experimental results from new and existing civil structure. The two geometrical design, cylindrical shape and Printed Circuit Board (PCB) based sensor parts of this research and their encapsulation technique for long-term enduring in harsh and corrosive environment of the civil infrastructure is described in the thesis. Results of an accelerated corrosion test on an embedded cylindrical shaped sensor indicates that the corrosion potential can be monitored with less than 10 mV resolution with a sensor sensitivity of ~0.73 kHz/mV. The last part describes a novel technique for a PCB sensor to simulate the existing structure already contaminated with corrosive substances such as chlorides. Two encapsulation techniques, non-conductive epoxy sealed and PLEXIGLAS with air gap sealed embedded PCB sensors response are compared from the accelerated corrosion test on new and built-in civil structure. Finally, results from the accelerated corrosion tests using the two encapsulation techniques mentioned above demonstrate that the embedded sensor in an existing structure may take up to 60 days to see the significant corrosion with a sensor sensitivity of ~ 1.53 kHz/mV or ~ 1.63 kHz/mV respectively. Since chlorides take many years to diffuse into concrete used for civil structures these sensors will respond fast enough to be used in existing structures as well as in new structures.

Acknowledgement

I would like to express my deepest appreciation and gratitude to my supervisor Dr. Douglas J. Thomson, who has the attitude and the substance of a genius: he continually and convincingly conveyed a spirit of adventure in regard to research and scholarship, and an excitement in regard to teaching. Without his constant guidance and persistent help the successful completion of this project would not have been possible. I will always appreciate the liberty and independence he gave me to find my own path.

I would like to thank "Dr. Cyrus Shafai and Dr. Norman L. Richards" for taking time out of their busy schedules to read my thesis. Their insightful suggestions helped me to improve my thesis.

Furthermore, the success of any project depends largely on the encouragement and guidelines of many others. I would to thank Dr. Greg E. Bridges, "who taught me two courses related to this research", for the useful comments, remarks and engagement through the learning process of this thesis.

Also, I take this opportunity to appreciate the assistance of Junhui Zhao, Daniel Card, Allen Symmons, Cory Smit, (technical staff of machine shop), Zoran Trajkoski (EM Imaging Laboratory) , Sinisa Janjic (Technical staff of Tech shop) and James Dietrich (Advance RF Systems Lab). I would like to thank Sharmistha Bhadra and Md. Obaej Tareq for their suggestions and help. I would like to acknowledge all of the professors and colleagues that I have encountered throughout my studies at the University of Manitoba. I would like to appreciate the financial support provided by ISIS Canada, FGS and NSERC during my course of study. Moreover, Department of Electrical and

Computer Engineering, Faculty of Engineering and FGS have always provided me financial support to present my papers in conferences.

Finally, I would like to thank my parents, brother, sisters and my best friend Tahriima Sultana for being ever supportive throughout the entire process, both by keeping me harmonious and helping me putting pieces together. Finally, I dedicate this thesis to my parents.

Table of Contents

List of Figures

List of Tables

List of Copyrighted Material for which Permission was obtained

- J.E.I. METALLURGICAL, INC. Retrieved August 8, 2013, from http://www.metallurgist.com/html/DefinitionsR-S.htm . Reprinted with permission from Craig Jerner of J.E.I. METALLURGICAL, INC, August 30, 2013. Used in page 6 of this thesis (as figure 1.3).
- Song, H., & Saraswathy, V. (2007). Corrosion monitoring of reinforced concrete structures - a review. *International Journal of Electrochemical Science , 2*, 1-28. Reprinted with permission from M. Antonijevic of International Journal of Electrochemical science, October 2, 2013. Used in pages 7, 9, 10, 11, 13 and 14 of this thesis (as Figure 1.4, Figure 1.5, Figure 1.6, Figure 1.7, Figure 1.8 and Figure 1.9).
- European Federation of Corrosion. Retrieved August 15, 2013, from http://www.efcweb.org/Working+Parties/WP+Corrosion+of+Steel+in+Concrete/WP+11+History.html . Reprinted with permission from Ines Honndorf, European Federation of Corrosion, Frankfurt Office of the General Secretariat, November 26, 2013. Used in page 5 of this thesis (as figure 1.1).

Nomenclature

RFID: Radio-Frequency Identification

SHM: Structural Health Monitoring

OCP: Open Circuit Potential

SNR: Signal to Noise Ratio

LPR: Linear Polarization Resistance

f_o: Resonant Frequency

ε_o: Permeability of Free Space

μ_o: Permittivity of Free Space

PVC: Poly Vinyl Chloride

Q: Quality Factor

PCB: Printed Circuit Board

Cl^- : Chloride Ions

Chapter 1: Introduction

1.1 Impacts of corrosion on society

The corrosion process is a natural phenomenon that occurs when a metal interacts with its surrounding environment, leading to a deterioration of reinforced structures. Corrosion effects on society on a daily basis leading to damage in household appliances, automobiles, highway bridges, airplanes, and any kind of concrete reinforced structure (Koch, Brongers, Thompson, Virmani & Payer, 2001). The corrosion of reinforced concrete is one of the main contributing factors to the aging of infrastructure causing losses in the billions of dollars. One corrosion study in U.S. in 1998 shows that the direct metallic corrosion cost is $276 billion on an annual basis excluding indirect corrosion costs, which is 3.1% of U.S. gross domestic product (GDP) (Koch, Brongers, Thompson, Virmani & Payer, 2001). Direct costs come from owners and operators of structures, suppliers of services and manufacturers of products. Different factors such as aging infrastructure, delays, failures, and litigation; taxes and extra cost of corrosion of goods and services; and cost of non- owner\operator activities lead to indirect costs, which is equal to the direct costs per annum. So, the total corrosion costs on annual basis have been estimated to be $552 billion which is 6% of U.S GDP (Koch, Brongers, Thompson, Virmani & Payer, 2001).

To protect the public safety and reduce economic losses, efforts are made to control and prevent metallic corrosion. Before using these methods, one of the important things is to know is when corrosion initiated. However, there are few low cost methods

that give useful information prior corrosion initiation. Some of the mechanisms for corrosion initiation are described below.

1.2 Mechanisms of Corrosion Initiations of Reinforced concrete

Generally, a thin layer of brown rust forms on the surface of the steel, if bright steel is left unprotected in the atmosphere which grows quickly. However, if the steel surrounded by a high pH alkaline environment with pH from 9.5 to 13 range corrosion will be inhibited. In this pH range, a passive film of approximately 1 μm thick is formed on the surface of the steel, reducing the corrosion rate to a very low and harmless value (Ervin & Reis, 2008),(Hope et al.,2001), (Portland Cement Association, n.d.). Therefore, concrete is a good choice of materials for this purpose providing high pH of 12 to 13. Also, concrete has high compressive strength compared to its tensile stress arising from the bond between cured cement and the aggregates. As such, concrete is frequently reinforced with the steel which makes the concrete almost stress free ("reinforced concrete", n.d).

There are several factors that contribute corrosion of reinforced concrete, among them two of the most common reasons are breakdown of localized passive film on the surface of the steel by Cl^- ingression and breakdown of passivity of steel by neutralization of concrete reacting with the atmospheric CO_2, which reduces the alkalinity of the concrete (Hope et al., 2001).

1.2.1 Reduction of alkalinity due to carbonation

In the modern environments, one of the main causes of increasing CO_2 concentration is industrial pollution and mankind's production of CO_2.

This gas reacts with the pore water alkalis in reinforced concrete such as calcium, sodium and potassium hydroxides, to form carbonates and at the same time reduces the pH of the concrete leading to the neutralisation of concrete (El-Shazly, Wazzan & Radain, 2012), (Gurten, Kayakirilmaz, & Erbil, 2007),(Roberts, 1981). If the carbonated fronts reach the surface of the steel, the protective film on the surface of the steel is no longer passive and its start to breakdown. To a large extent, the advancement of the carbonated front depends on the exposure condition, porosity and permeability of the concrete. The reaction between atmospheric CO_2 and pore water alkalis is given below (Chemical formula, n.d.), (Hope et al., 2001)

$$Ca(OH)_2 + CO_2 \rightarrow CaCO_3 + H_2O \quad (1.1)$$

The above reaction reduces the pH of the pore water to the 8-9 range by consuming OH ions. When the pH reduces to this level the steel loses its protective passive film and corrosion can begin.

The redox reaction for rust formation are given below

$$\text{Reduction: } 4e^- + 2H_2O(l) + O_2(g) \rightarrow 4OH^-(aq) \quad (1.2)$$

$$\text{Oxidation: } 2Fe(s) \rightarrow 2Fe^{2+}(aq) + 4e^- \quad (1.3)$$

$$\text{Overall: } 2Fe(s) + 2H_2O(l) + O_2(g) \rightarrow 2Fe^{2+}(aq) + 4OH^-(aq) \quad (1.4)$$

$$2Fe^{2+} + 2OH^- \rightarrow Fe(OH)_2(s) \quad (1.5)$$

$$Fe(OH)_2(s) = O_2 \rightarrow Fe(OH)_3(s) \quad (1.6)$$

$$Fe(OH)_3 = \text{dehydrate} \rightarrow Fe_2O_3.nH_2O(s) \text{ [Chemical formula of rust]} \quad (1.7)$$

1.2.2 Reduction of alkalinity due to Cl^- ingression

Another reason for loss of alkalinity of concrete structures is due to Cl^- ingressions from de-icing salts used to keep roads clear of snow and reduce ice in winter (Ervin & Reis, 2008). The Cl^- ion acts to reduce pH and initiate corrosion. The Cl^- ion also acts as a catalyst to initiate the corrosion of steel reinforcement by destroying the passive film locally and promote the corrosion towards the whole structure by dissolving the steel rebar. At lower level of Cl^- concentration, the corrosion rate is negligible. However, de-icing salts increase the concentration of Cl^- in concrete above the threshold level of each specified structure results in a dramatic increase in the corrosion rate (Hope et al., 2001).The reaction of Cl^- and steel rebar are given below

$$2Fe + 6Cl^- \leftrightarrow 2FeCl_3^- + 4e^- \quad (1.8)$$

Figure 1. 1: Chloride induced reinforcement corrosion in concrete exposed to seawater (European Federation of Corrosion, n.d.)

$$FeCl_3^- + 2OH^- \leftrightarrow Fe(OH)_2 + 3Cl^- \quad (1.9)$$

Now, the rust formation follows the above equations 1.6 and 1.7.

1.2.3 Cracks appearing due to mechanical loading

There are several factors that help to form cracks on the surface of the concrete, for example, tensile loading, and concrete shrinkage with curing, expansion and

contraction due to moisture and temperature change. These cracks allow easy penetration of CO_2 and Cl^- from the atmosphere and de-icing salt respectively.

Figure 1. 2: Crack appearing due to Mechanical Loading (Wikimedia commons, n.d.)

Cracks can be a natural part of the aging of structures or may be due to the improper design and construction of the concrete structures, e.g. addition of large mixing water, improper or no curing, improper jointing, improper subgrade preparation (Carino &Clifton, 1995).

1.2.4 Presence of Stray Currents

Presence of stray currents in the reinforced concrete structure arising from, for example, cathodic protection systems, high voltage power lines, railways tracks can helps to corrode the reinforce steel, leading to a severe localized corrosion attack.

Figure 1. 3: Stray current corrosion on a copper water pipe (J.E.I. METALLURGICAL, INC., n.d.)

This current finds a low resistance path by flowing through the metallic structure, where a cathodic and an anodic reaction happens resulting an extremely localized attack and can be severe with time (Bertolini, Carsana, & Pedeferri, 2007). During this time, steel rebar can be contaminated by the atmospheric CO_2 and Cl^- from the windblown salt.

1.2.5 Corrosion of reinforced steel due to moisture pathways

If high moisture conditions persist around concrete structures, water content will eventually penetrates through diffusion or by travelling along the cracks making the structure more vulnerable to corrode.

1.2.6 Water-cement mixing ratio

If the water-cement mixing ratio is higher than expected or specified for making a structures, then the cast concrete becomes more porous in the presence of moisture content (Chan, Ho & Chan, 1999). Therefore, the higher diffusion of water and electrolytes through the concrete leads the concrete more susceptible to cracking and corrosion.

1.2.7 Corrosion of reinforced steel due to Low Concrete Tensile strength

Low tensile strength can initiate the corrosion in two ways. Firstly, it may develop shrinkage and tension, which can easily, crack the concrete making a path for CO_2, moisture and in some cases Cl^- to reach the surface of the reinforcement.

1.2.8 Electrical contacts with dissimilar metals

If any two dissimilar metals come in contact with concrete it forms a galvanic cell, then a current flows from more electro-positive metal to less electro-positive metal by redox reaction. This is known as galvanic corrosion. However, this galvanic corrosion can be caused due to two dissimilar metals in same environment or if the same metals are in two different environments ("Galvanic Corrosion", n.d).

1.3 Existing methods of detecting corrosion

1.3.1 Open circuit Potential Measurements

The most typical procedure to monitor the reinforced concrete structures is via open circuit potential measurements (Song & Saraswathy, 2007), (Elsener, Molina &Bonhi, 1993), (Elsener & Bonhi, 1990), (Broomfield, Langford & Ewins, 1990). Any metal has the tendency to generate a potential, when it comes to a contact with something that can act as an electrolyte. The generated potential gives the information about the surrounding environmental conditions. In the reinforced concrete structure, concrete acts as an electrolyte and the reinforcement will develop a potential depending on the concrete environment. The schematic diagram in fig.1.4 shows a set up for open circuit potential measurement.

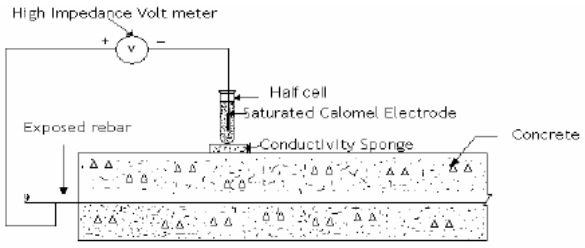

Figure 1. 4: Schematic diagram of Open Circuit Potential Measurements (Song & Saraswathy, 2007)

The principle behind this method is to measure the potential of the reinforcement with respect to a standard reference electrode such as saturated calomel electrode (SCE), copper/copper sulfate electrode (CSE), silver/silver chloride electrode etc. (Song & Saraswathy,2007). *ASTM C 876 Standard Test Method for Half-Cell Potential of Reinforcing Steel* describes the interpretation of open circuit potential measurements (ASTM C 876-91, 2006), (Song & Saraswathy, 2007). This method only gives us the probability of the corrosion in reinforced structure. It does not give the insightful information about prior corrosion or the rate of corrosion (Song & Saraswathy, 2007). Moreover, the measured potentials are affected by a number of factors, which include polarization by limited diffusion of oxygen (Song & Saraswathy, 2007), (Arup, 1983) concrete porosity, and the presence of highly resistive layers.

1.3.2 Surface Potential Measurements

Surface potential measurement is a non-destructive technique to measure the corrosion probability indirectly as potential measurement by identifying the cathodic and anodic regions in the reinforced concrete structure. A schematic diagram of surface potential measurements is shown in fig. 1.5. During the corrosion process, an electric current flows through the concrete from anode to cathode which can be detected as potential drop between two electrodes. In this method, one electrode kept fixed on the structure on a symmetrical point and the other one known as moving electrode is moved along the structure. No electrical connection is necessary in this measurement.

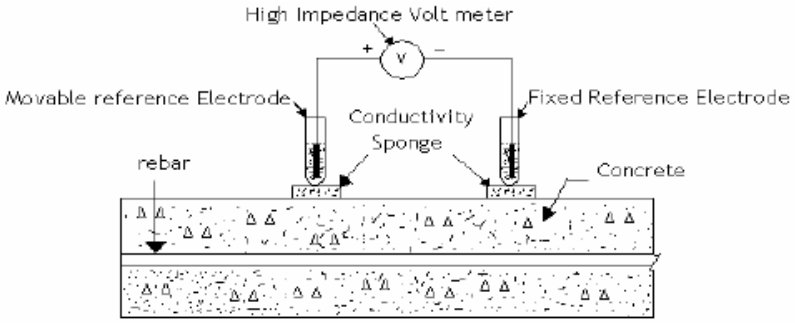

Figure 1. 5: Schematic diagram of Surface Potential Measurements (Song & Saraswathy, 2007)

The potential of the movable electrode is measured with respect to the fixed electrode using a high impedance voltmeter (Song & Saraswathy, 2007).A more positive potential gives the information about the possibility of corrosion. The probability of corrosion is greater, if the potential difference between anodic and cathodic areas is greater (Song & Saraswathy, 2007).

1.3.3 Concrete Resistivity Measurements

The electrical resistivity is an important parameter which determines the intensity of initiated corrosion process. The high electrical resistivity in concrete shows that the corrosion process is slow compared to low resistivity in which the current can easily pass between anode and cathode areas. Two techniques, namely AC and DC measurements are used for determination of electrical resistivity. In these measurements both surface and embedded probes are applied. In DC measurement, a constant electric field is applied between the two embedded electrodes and measure the resulting current as a voltage drop over a small resistance.

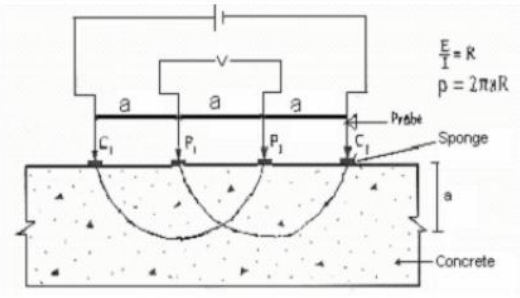

Resistivity (Ohm.cm.)	Corrosion risk
Greater than 20,000	Negligible
10,000 to 20,000	Low
5,000 to 10,000	High
Less than 5,000	Very high

Figure 1. 6: Schematic Diagram for electrical resistance measurements (Song & Saraswathy, 2007)

In AC measurements, two and four-pin methods can be used. A schematic diagram of electrical resistance measurements using four pin methods is shown in fig. 1.6. Among them Wenner array is the most common surface mounted probe. A known alternating current 'I' is applied on the outer probes and the resulting potential drop 'V' between the inner probes is measured and resistance 'R' is given by V/I which is shown in fig.1.6 (Song & Saraswathy, 2007).

The resistivity of concrete (ρ) $=2\pi aR$ (1.10)

Where, 'a' is the inner electrode distance in cm and 'R' is the measured resistance in ohm. The electrical resistivity of concrete is being increasingly used indirectly to evaluate concrete characteristics such as the chloride ion diffusivity, the degree of concrete saturation and its aggressiveness (Song & Saraswathy, 2007), (Berke & Hicks, 1992), (Andrade, Alonso &Goni, 1993). The electrical resistivity of concrete is inversely proportional to the corrosion rate indicated by Feliu and coworkers (Song & Saraswathy, 2007), (Feliu, Gonzalez, Feliu, Jr. & Andrade, 1989). It was supported by Glass et al., who showed that the effect of mortar resistivity on the rebar corrosion rate was strongly dependent on the environmental relative humidity (Song & Saraswathy, 2007), (Glass et al., 1991). It was reported that the electrical resistivity of concrete was proposed as an

effective parameter to evaluate the risk of reinforcing steel corrosion, particularly when corrosion is induced by chloride attack (Song & Saraswathy, 2007), (Morris et al., 2002). However, the threshold level of concrete resistivity is different for different exposure conditions. It is strongly dependent on concrete quality and on the exposure conditions, such as the relative humidity and also temperature affects the degree of concrete pore saturation (Song & Saraswathy, 2007), (Hussain, 1995), (Hope, 1985) and so the resistivity values. Conductivity is a useful additional measurement to aid in identifying problem areas or confirming concerns about poor quality of concrete. Measurements can only be considered alongside other measurements (Song & Saraswathy, 2007).

1.3.4 Linear Polarization Resistance (LPR) Measurements

The Linear polarization resistance measurement is rapid and non-intrusive, requiring only a connection to the reinforcing steel. The obtained data by this technique gives a valuable insight into the instantaneous corrosion rate of the steel reinforcement. It enables a more detailed assessment of the structural condition and is a major tool in deciding upon the optimum remedial strategy to take on (Song & Saraswathy, 2007). A schematic diagram of linear polarization resistance measurement is shown in fig.1.7.

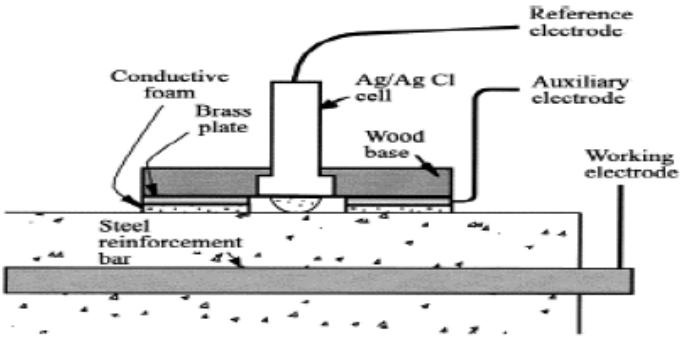

Figure 1.7: Schematic Diagram of Linear Polarization Resistance measurement (Song & Saraswathy, 2007)

In LPR measurement the reinforcing steel is perturbed by a small potential change from its equilibrium potential. This can be done potentiostatically by changing the potential of the reinforcing steel by a fixed amount, ΔE, and monitoring the current decay, ΔI, after a fixed time. Alternatively it can be done galvanostatically by a applying a small fixed current, ΔI, to the reinforcing steel and monitoring the potential change, ΔE, after a fixed time period (Song & Saraswathy, 2007). The conditions are selected in each case such that the change in potential, ΔE, falls within the Stern-Geary range of 10-30mV. The polarization resistance, Rp, of the steel is calculated using the following equation

$$Rp = {\Delta E}/{\Delta I} \tag{1.11}$$

Corrosion current, Icorr, can then be calculated using eq^{n}. 1.12.

$$Icorr = {B}/{Rp} \tag{1.12}$$

Where, *B* is the Stern-Geary constant. The value of *B* is 25mV for active steel and 50mV for passive steel. The corrosion current density, *icorr*, can be calculated using eq^{n}. 1.13.

$$icorr = {Icorr}/{A} \tag{1.13}$$

Where, A is the surface area. For LPR measurement, the surface area needs to be accurately known. In a conventional LPR test the perturbation is applied from an auxiliary electrode on the concrete surface which is shown in fig. 1.7. The surface area of steel assumed to be polarized is that lying directly beneath the auxiliary electrode (Song & Saraswathy, 2007).The difficulty of this technique is to quantify accurately the area, A, being measured.

1.3.5 Galvanostatic Pulse Transient Method

This measurement method is a transient polarization technique which works in the time domain (Elsener, Klinghoffer et al., 1997), (Song & Saraswathy, 2007). In this technique, a short time anodic pulse is imposed galvanostatically on the reinforcement bar from a counter electrode placed on the concrete surface. This anodic current is applied in the range of 10 to 200μA and the typical pulse duration is up to 10 seconds. In the anodic direction, the reinforcement steel is polarized compared to its free corrosion potential which results a change of the electrochemical potential of the reinforcement. This potential change is recorded by a reference electrode as a function of polarization time (Song & Saraswathy, 2007). Usually, the reference electrode is in the center of the counter electrode which is shown in fig. 1.8.

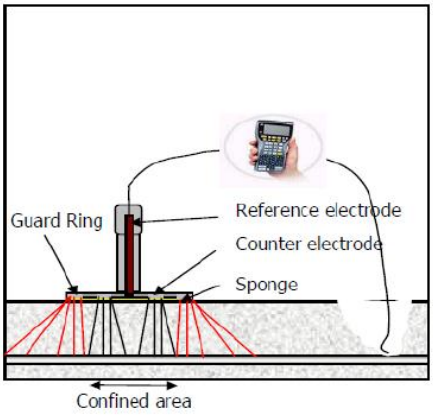

Figure 1. 8:Set-up for Galvanostatic pulse method (Song & Saraswathy, 2007)

However, this technique suffers the same difficulty as LPR technique to quantify the investigated area for reinforced concrete structures in the field.

1.4 Wireless Methods of Detecting Corrosion

1.4.1 Embeddable Corrosion Monitoring Sensor

Commercially produced embeddable corrosion instrument (ECI) incorporates five sensors in a small rugged package, as shown in fig. 1.9. This sensor measures five key factors in corrosion monitoring which are linear polarization resistance, open circuit potential, resistivity, chloride ion concentration and temperature. It is designed to monitor the bridges, buildings, dams, erosion control structures, flood control channels, parking garages, piers, pylons, roadways, and spillways. The embedded corrosion instrument integrate processing electronics with its sensors and thus can use digital communication resulting elimination of data corruption by electro-magnetic interference from power lines, radio waves, and cellular telephones (Song & Saraswathy, 2007).

Figure 1. 9: Installation of ECI (Virginia Technologies, Inc., n.d), (Song & Saraswathy, 2007)

The ECI (Virginia Technologies, Inc., n.d.) is a non-destructive evaluation (NDE) device, it gathers and delivers all data without requiring inspectors to cut samples, interrupt use of a structure, or even visit the site (Song & Saraswathy, 2007). This sensor is based on an active power wireless communication protocols, so it faces the difficulty

of recharging or replacing the batteries of the embedded sensors. This sensor is expensive in per unit basis, making its wide scale deployment costly.

1.4.2 Ultrasonic Pulse Velocity Measurement

Ultrasonic pulse velocity (UPV) is a non-destructive technique involving the measurement of speed of sound through materials in order to predict material strength, to detect the presence of internal flaws such as cracking, voids, honeycomb, decay and other damage (Song & Saraswathy, 2007). The principle of this technique lays on the fact that many solid materials are good conductors of ultrasonic wave. The waves are reflected and refracted at the interface or the boundary of the material. By measuring the received wave, the characteristics of the concrete structure are determined. The main strength of the method is in finding general changes in condition such as areas of weak concrete in a generally sound structure. Sometimes, this method is not practicable to test sound concrete, especially in investigation of crack depth; it is ineffective if the crack is water filled (Song & Saraswathy, 2007).

1.4.3 Unpowered Wireless Corrosion Sensor

This sensor is extremely simple and low cost; it has been developed to detect the onset of corrosion in reinforced concrete structure. The sensor is a simple LC resonant circuit and can be powered and interrogated by inductively coupled magnetic fields. Initially, the resonance behavior of this sensor is the contribution of parallel combination of the two capacitors in the circuit (Andringa, Neikirk, Dickerson, & Wood, 2005), (Pasupathy, Zhuzhou, Neikirk, & Wood, 2008), (Abu Yousef, Pasupathy, Wood, & Neikirk, 2010).

The schematic diagram of the sensor is shown in (fig.2) Andringa, Neikirk, Dickerson, & Wood, 2005. In this sensor, capacitor C_2 is connected with C_1 by a wire transducer.

When, the transducer wire begins to corrode, the phase dip of the impedance becomes smaller and begins to shift in frequency. The main advantage, no active power or battery is required to operate this sensor. Though, it only detects corrosion after it has occurred. This has the disadvantage of giving a signal when it is too late to use methods to decrease or stop the effects of corrosion.

1.4.4 Embeddable RFID based Wireless Corrosion Sensor

Commercial RFID Technology based wireless passive sensors have been reported in (Watters et al., 2003), (Apblett & Materer, 2010), (Leon-Salas, Kanneganti, & Halmen, 2011), (Alamin, Gui, Andrews, & Jackson, 2012). One of the RFID technology based sensor known as Smart Pebble^{TM} is developed by SRI international. This sensor is a passive wireless sensor and can monitor the level of chloride ingress into concrete bridge decks.

It contains a chloride sensor with a low power passive RFID (Radio frequency identification) chip; these are typically a size and weight of a piece of rock aggregate (Watters et al., 2003).

It is “smart” in that it contains a chloride sensor and radio frequency identification (RFID) chip that can be queried remotely both to identify it and to indicate chloride concentration level (Watters et al., 2003). This device is powered remotely, thus it has the longer lifetime than active powered device. It is designed to be embedded in a bridge deck either during the initial construction (or during refurbishment) or a back filled core

hole. Oklahoma Transportation Center (OKTC) proposed a technique for corrosion monitoring using a RFID with a microcontroller, the small portion of the coil on RFID is replaced by a link material which can be used for corrosion sensing (Materer, Apblett & Ley, 2011). Using a custom RFID reader, the presence of corrosion on the link material absorbs the reader's radio frequency radiation causing the sensor not to respond to the RFID reader (Materer, Apblett & Ley, 2011). However, it does not provide the corrosion initiation and intermediate stage before the reader stops to read same as the unpowered binary sensor based on a radio frequency resonance phenomenon developed by Dean Neikirk and their team at University of Texas, Austin (Materer, Apblett & Ley, 2011), (Andringa, Neikirk, Dickerson, & Wood, 2005), (Andringa, Neikirk, Dickerson, & Wood, 2005). However, researchers have identified several limitations using RFID for long term SHM which are the reliability of the data stream coming from the RFID tag, reliability of the reader with proper inclusion of error checking and correcting bits of the received data stream from the RFID tag to establish at different reading speed and distances, the parasitic corrosion may come from the long-term embedment of the RFID electronics inside the harsh and corrosive environment of the concrete and the communication protocols changes over time (Materer, Apblett & Ley, 2011), (Sharmistha Bhadra and Douglas J Thomson and Greg,E.Bridges, 2013).

1.4.5 Inductively Coupled Coil Corrosion Potential Sensor

Inductively coupled coil corrosion sensor is based on a simple LC resonant circuit principle whose resonant frequency (possibly quality factor) is a function of corrosion potential. The idea of detecting bio-potential signals using a LC circuit has been first published in form of a patent application and approved patent in 1965 by Honig

(Riistama, Aittokallio, Verho, & Lekkala, 2010), (Honig, W.M., 1965). In our sensor design, a sensing circuit comprising a Varactor diode and few other components are connected parallel with an inductive coil which is formed a resonant circuit. The other terminal of the sensor circuit is connected with two different types of rebar, one is serving as reference bar and another is a reinforcement bar forming a voltaic cell inside the concrete (Bhadra, Bridges, & Thomson, 2010), (Thomson, Perveen, Bridges, & Bhadra, 2012), (Perveen, Bridges, Bhadra, & Thomson, 2013).

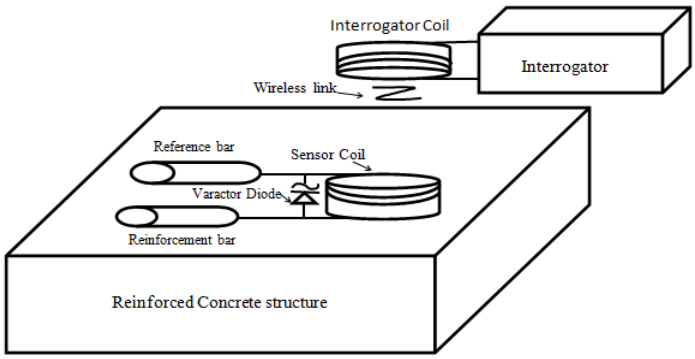

(a)

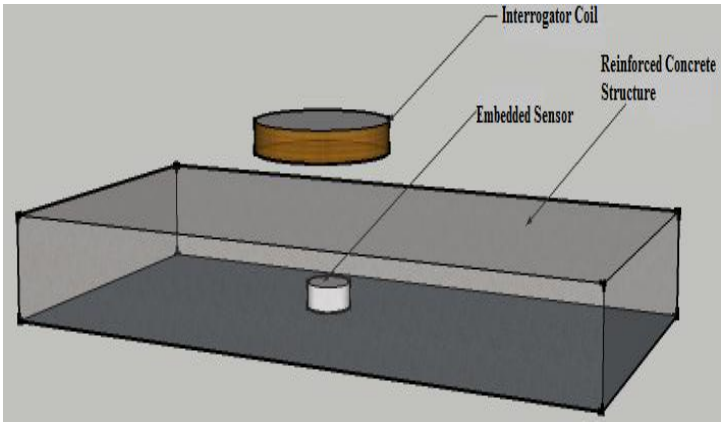

(b)

Figure 1. 10: (a) A Schematic block diagram of embedded corrosion sensor with details (Thomson, Perveen, Bridges, & Bhadra, 2012). b) A block diagram of embedded corrosion sensor

An external interrogator electronics are used to measure the sensor coils' resonant frequency shift produced by the voltage from the two rebar electrodes.

In fig. 1.10, an equivalent circuit of coupled coil sensor and interrogator electronics is presented. The junction capacitance C_j of the reverse biased varactor diode is varied with the corrosion voltage is shown below:

$$C_j(V_{\text{var}}) = C_0(1 - V_{\text{var}}/\phi)^{-\gamma} \tag{1.14}$$

where C_0 is the junction capacitance at zero bias, V_{var} is the voltage across the varactor, ϕ is the junction built in potential (0.5 volts for Si and 1.3 for GaAs) and γ is the doping profile (0.5 for an abrupt junction and 2 for hyper-abrupt junction) factor (Thomson, Perveen, Bridges, & Bhadra, 2012), (Sharmistha Bhadra and Douglas J Thomson and Greg, E. Bridges, 2013).

The sensor circuit resonant frequency shifts with corrosion voltage depending on the junction capacitance Cj, from the fig. 1.10

$$f_0 = \frac{\omega_0}{2\pi} = \frac{1}{2\pi\sqrt{L_2 C_j(V_{\text{var}})}} \tag{1.15}$$

where f_0 is the resonant frequency, L2 is the sensor coil inductance. Therefore as the corrosion voltage changes it causes the voltage across the varactor to change and therefore the resonant frequency to shift. By measuring the shift in resonant frequency the corrosion voltage can be measured (Perveen, Bridges, Bhadra, & Thomson, 2013), (Thomson, Perveen, Bridges, & Bhadra, 2012), (Sharmistha Bhadra and Douglas J Thomson and Greg, E. Bridges, 2013). A comparison among different corrosion detection techniques is shown in table 1.1.

Table 1. 1: Comparison of different corrosion detection techniques

Existing methods of corrosion detection		
Name of the Methods	Advantages	Limitations
Open circuit Potential Measurements	Useful technique to find out the anodic and cathodic site in the reinforced concrete structures	Provides the probability of the corrosion and can not indicate the rate of corrosion
Surface Potential Measurements	The greater the potential difference between anodic and cathodic areas greater is the probability of corrosion	Provides the probability of the corrosion and can not indicate the rate of corrosion
Concrete Resistivity Measurements	Useful additional measurement to aid in identifying problem areas or confirming concerns about poor quality concrete	Provides the probability of the corrosion and can not indicate the rate of corrosion
Linear Polarization Resistance (LPR) Measurements	Can detect the corrosion rate at real time	The area of steel surface being measured is difficult to quantify
Galvanostatic Pulse Transient Method	NDE technique.	The area of steel surface being measured is difficult to quantify
Wireless Methods for detecting Corrosion		
Embeddable Corrosion Monitoring Sensor	It measures five key factors in corrosion which are linear polarization resistance, open circuit potential, resistivity, chloride ion concentration, and temperature	Based on active power communication. It suffers recharging and replacing of battery.
Ultrasonic Pulse Velocity Measurements	NDE technique. Can predict the material strength. Can detect the presence of internal flaws such as cracking, voids, honeycomb, decay and other damage. Main strength of this method is in finding general changes in the structures.	This technique is not always practicable in testing sound concrete. Especially in investigation of crack depth, it is ineffective if the crack is water filled.
Unpowered Wireless Corrosion Sensor	Requires no active power. Wireless and Inexpensive	Cannot provide the information about the corrosion initiation
Embeddable RFID based Corrosion Sensor	Requires no active power. Wireless and Inexpensive	Reliability of the reader coil with different speed and separation distance including their error correction process. Communication protocol changes for long term embedment
Inductively Coupled Corrosion Potential Sensor	Wireless, passive and inexpensive, Can detect the corrosion initiation. Also indirectly detect the chloride concentration in the civil structures	

1.5 Main Contributions

The goal of this research is to optimize and study the behavior of the coupled coil corrosion potential sensor in reinforced concrete structures. For long-term service life of this sensor in the concrete structure, the encapsulation method becomes a very important matter. However, the sensor has been optimized by careful choice of several factors such as coil wire, size of interrogator coil, sensitivity of the sensor to the surrounding environments and choice of encapsulation methods. Therefore, the quality factors (Q-factor) of the sensor and the separation distance between the sensor and the interrogator coil have been increased. This sensor is capable of detecting conditions prior to full-scale corrosion occurring and can give the information about initiation of corrosion reinforced concrete structures. The sensor is embedded during initial construction (new structure) and in the existing structure using back filled core slot technique. In this work an accelerated corrosion test is carried out on both types of sensor to limit the testing time. The accelerated corrosion test results shows that this sensor is capable of detecting conditions at the initiation of corrosion in the concrete structure and can detect the corrosion potential less than 10 mV resolution.

1.6 Organization of Thesis

This thesis focuses the design and optimization of the wireless corrosion potential sensor. Moreover, it focuses the experimental detection of the corrosion condition prior to the initiation of corrosion on both new and existing structures. The thesis is organized as follows:

- Chapter 2 presents the fixed capacitor and varactor based circuit modelling of wireless corrosion potential sensor. It includes the simulation and modelling

of the sensor using both time and frequency domain interrogation technique. Also, it discusses the design of printed circuit board (PCB) based corrosion potential sensor.

- Chapter 3 shows the optimization and fabrication techniques of coupled coil corrosion potential sensor. It also presents the encapsulation steps for a cylindrical shape and a PCB based design of this corrosion sensor.
- Chapter 4 demonstrates all the results from different tests on cylindrical shape sensor. It shows the DC calibration on cylindrical shape sensor and comparison between fixed capacitor and varactor based models. It also describes the comparison of simulated and experimented results which include time domain interrogation and impedance measurement technique. Furthermore, an accelerated corrosion test set up and experiment results cylindrical shape sensor are shown here.
- Chapter 5 describes all the results from different tests on PCB based corrosion sensor. It demonstrates the optimization process of encapsulation of the sensor. A double layer casting technique and experiment set-up on PCB based corrosion sensor and the comparison of accelerated corrosion results among four different percentage (%) salt mixed reinforced structures are shown here. Furthermore, it shows the embedded sensor performance in new and existing structure.
- Chapter 6 describes the conclusion and future work.

Chapter 2: Circuit modeling of Passive wireless corrosion sensor

2.1 Introduction

This chapter focuses on circuit modeling of the passive wireless corrosion sensor and its interrogation by various methods, such as frequency domain and time domain analysis. In frequency domain analysis, we have measured our sensor coupled resonant frequency using a precision Impedance analyzer (Agilent 4294A), but the measurement is limited by background interference (Bhadra, S., 2010).

In time domain analysis, a sinusoidal signal is used to energize the sensor for few microseconds, it will then ring down at sensor's natural frequency. The signal is monitored by an externally coupled interrogator coil. However, this approach is better than the frequency domain analysis; because it can track the sensor resonant frequency shift without being affected by the surroundings and can have an extended separation distance between sensor coil and the interrogator coil. Also a printed circuit board design of the sensor is also modeled in this chapter.

2.2 Basic Model of Sensor-Varactor Modeling

A schematic diagram of embedded sensor and interrogator is shown in fig.2.1. The sensor circuit comprises a Varactor diode and few other components connected in parallel with an inductive coil which forms a resonant circuit. The other terminal of the sensor circuit is connected with two different type of rebar; one is serving as reference electrodes, which along with the second steel reinforcement bar form a galvanic cell

inside the concrete. In this situation the concrete acts as an electrolyte between the two electrodes. Interrogator electronics are used to detect the sensor coils' resonant frequency shift produced by the voltage across the two rebar that is produced when the second reinforcement bar begins to corrode (Thomson, Perveen, Bridges, & Bhadra, 2012).

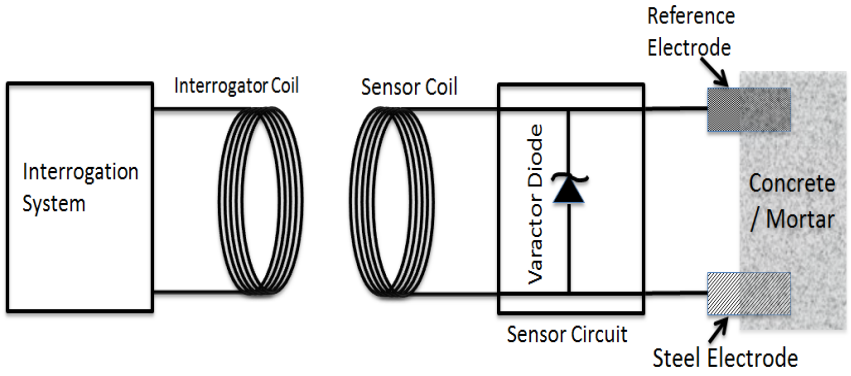

Figure 2. 1: A schematic diagram of a coupled coil corrosion sensor embedded inside the reinforced concrete structure.

In fig. 2.2 an equivalent circuit of coupled coil sensor and interrogator electronics is presented. The junction capacitance C_j of the reverse biased varactor diode is varied with the corrosion voltage is shown in eqn 1.14.

2.3 System Circuit Modelling

2.3.1 Pspice™ Simulation Model of Coupled Coil Corrosion Sensor

A SPICE model has been developed for the sensor coil coupled with the interrogator electronics, shown in fig. 2.2.

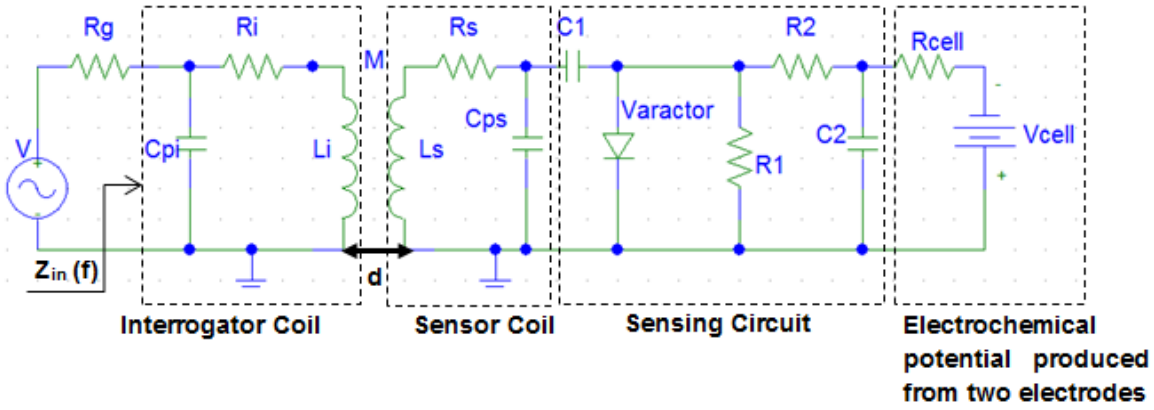

Figure 2. 2 : Equivalent electrical circuit of corrosion sensor coupled with interrogator electronics

The circuit parameters are determined by fitting the experimentally measured results to the model or by direct measurment using an impedance anlyzer (Agilent 4294A). In the above circuit modelling, R_g, 50Ω, is the source impedance; parasitic capacitances of interrogator, C_{pi}, and sensor coil, C_{ps}, are respectively 8.12pF and 2pF. Series resistances R_i and R_s are 0.474Ω and 20.1Ω. Inductances L_i and L_s are 3.32μH and 63.52μH. Moreover, R_2, 1MΩ, and C_2, 100pF, acts as a protection circuit for varactor diode from the static charge when the sensing circuit is not connected with the coil and the electrodes and R_1, 10GΩ, is the leakage path of the varactor diode and also helps to protect from the galvanic corrosion, NXP-BB202. A large capacitor C_1, 1nf, is used to block DC current flow through the sensor coil. The separation distance between interrogator and sensor coil is d, and M is the mutual inductance. R_{cell} and V_{cell} represent respectively the cell resistance and the electrochemical potential difference generated from two electrodes when two electrodes embedded in the concrete. In the simulation, a DC voltage is used instead of corrosion voltage.

2.3.1.1 Time Domain Interrogation

Both time domain interrogator built by Daniel Card and frequency domain interrogator were used. The time domain interrogator used a pulse echo approach, where the sensing coil was excited with a transmit signal and then switched into a receiving mode. The time domain interrogator circuit consists of a transient voltage source whose amplitude and timing are carefully chosen to prevent non-linear driving of the varactor diode. In transmit mode, an exciting signal is used to power the sensor coil whose resonant frequency is chosen close to the sensor coupled resonant frequency (Bhadra, S., 2010). However, sensor's resonant frequency is independent of the source frequency which oscillates near to its resonant frequency. The natural response of the sensor circuit is an exponentially decaying sinusoidal signal, which is the received signal (Bhadra, S., 2010). This signal is analyzed to determine the sensor coil resonant frequency (Bhadra, S., 2010). In order to understand the behavior of this system, SPICE simulation transient analysis equivalent to the time domain interrogation system was carried out. The measured and the simulated results are close in agreement. Using the following formula, the resonant frequency of the sensor is estimated by taking the average time for several cycles using zero crossings of the signal in receive mode

$$f_{res} = \frac{1}{T_a} \tag{2. 1}$$

where, T_a is the average time of few cycles of the signal in receive mode.

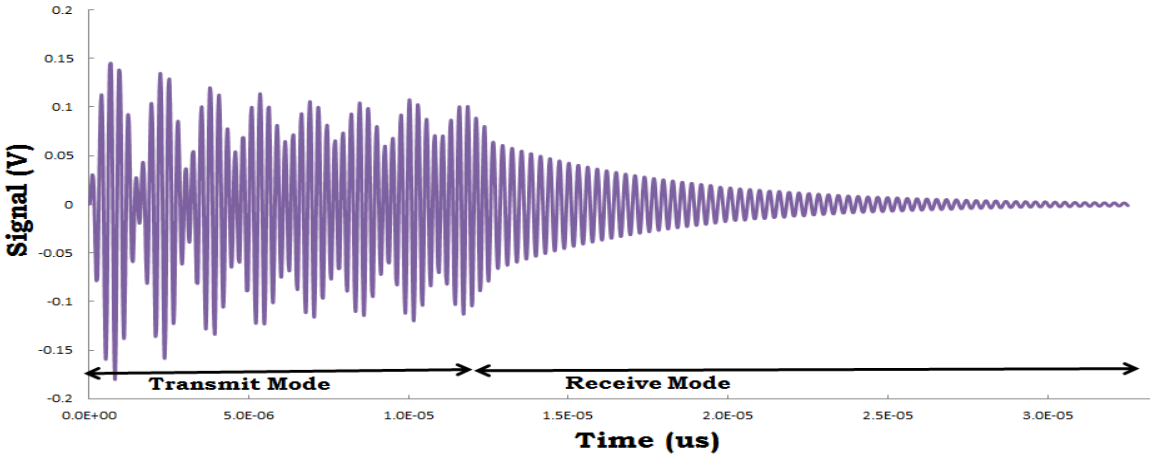

Figure 2. 3: Signal across the varactor diode for source frequency =3.85MHz and the simulated sensor resonant frequency fres =3.3156MHz

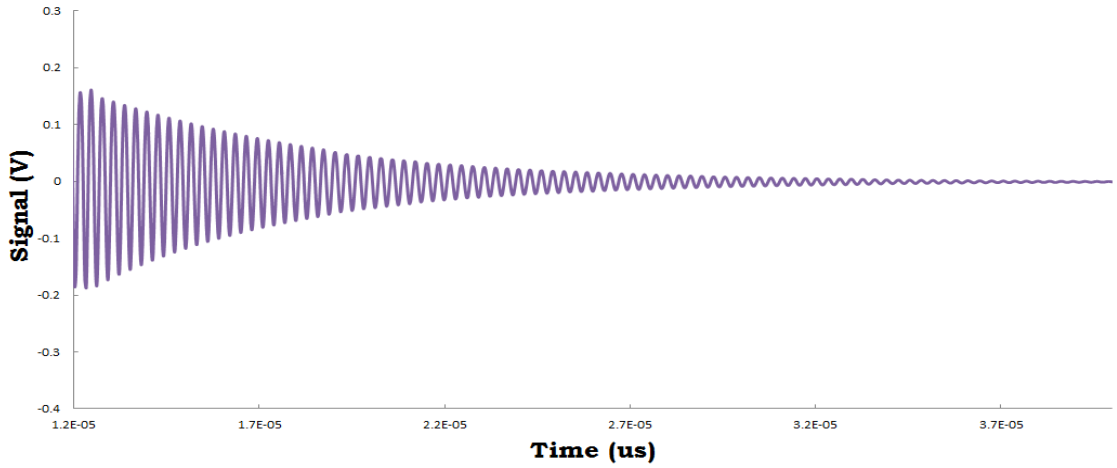

Figure 2. 4: Signal across the varactor diode for source frequency =3.85MHz in the receive mode and the simulated sensor resonant frequency fres =3.3156MHz

In time domain Interrogation (Bhadra, S., 2010), a few μs delay has been used between transmit and receive mode, which is not shown in the simulated response. This delay is used to allow non-idealities in the switching to dissipate. So, when the sensor frequency is estimated from the received signal in receive mode, the first couple of cycles contain the signal from source frequency. Therefore, the sensor resonant frequency is estimated after a first few cycles from the signal in receive mode.

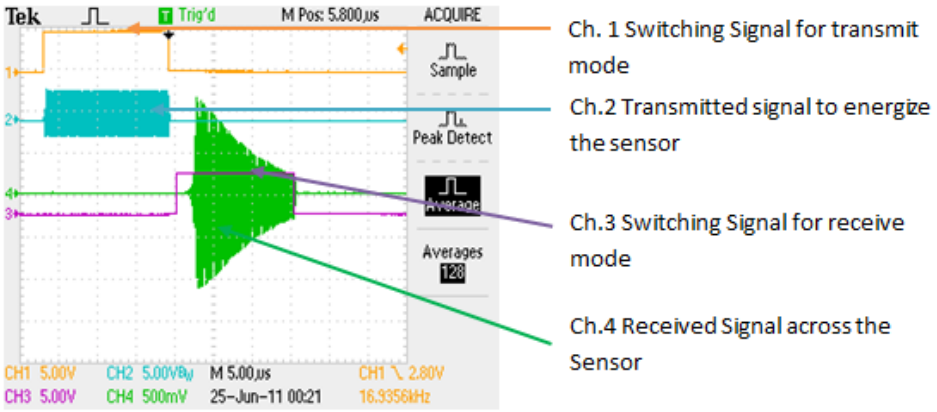

Figure 2. 5: Transmitted, switching and received signal in Time Domain Gating System (TDGS)

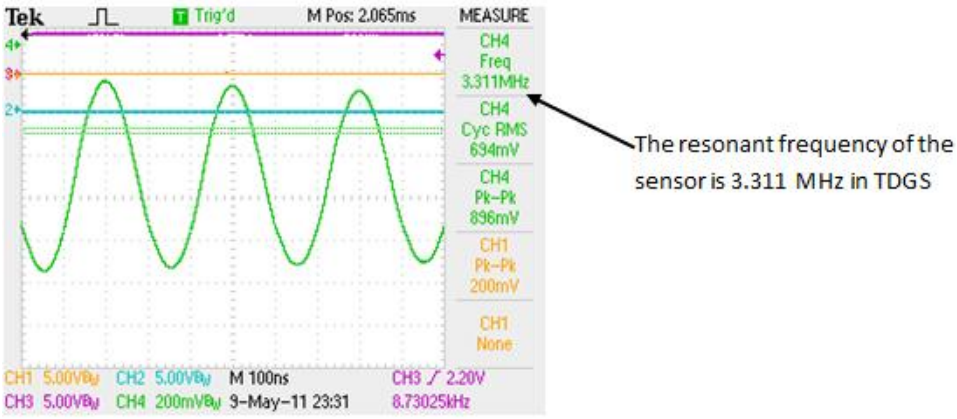

Figure 2. 6: Received signal across the sensor (magnified) in Time Domain Gating System (TDGS)

From the above fig. 2.6 and fig 2.4, the measured resonant frequency of the sensor using TDGS measurement has 4.6 kHz difference from the simulation. In the simulation, measured inductance, L_s= 56.94µH and varactor capacitance at zero bias C_{Var}=34.5 pf were used. The variation may arise from the measured inductance and capacitance with a margin of $L_s = 56.94\mu H \pm 0.16\mu H$ and $C_{Var} = 34.5pf \pm 0.11pf$. Moreover, the effect of lead inductance from the two wires used for shorting the two electrodes was not considered in the simulation.

2.3.1.2 Frequency Domain Interrogation

In frequency domain interrogation, the sensor has been tested using a precision impedance analyzer (Agilent 4294A). Here, the sensor resonant frequency is estimated using a swept frequency by measuring the real part of the impedance from the source end. At resonant frequency, the imaginary part of the measured impedance becomes zero and the real part has a maximum value. This maximum value is extracted at the sensor resonant frequency using a quadratic curve fitting algorithm (Bhadra, S., 2010).

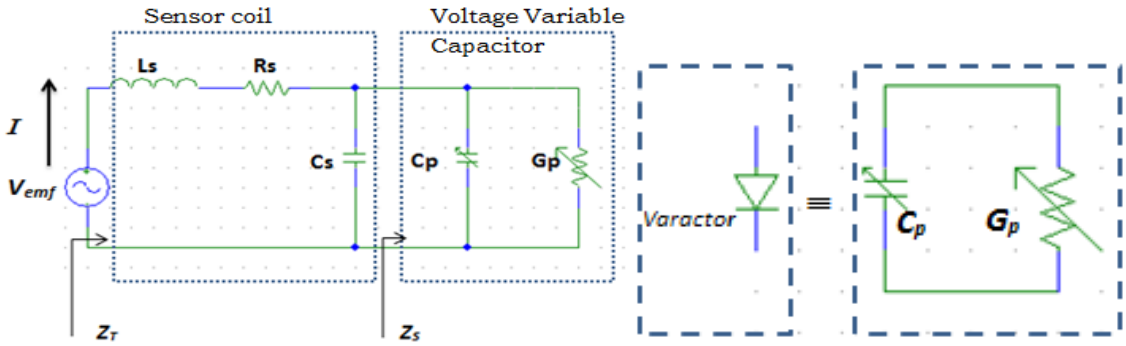

Figure 2. 7: (a) Equivalent circuit diagram of the sensor with induced Vemf, when the sensor coil coupled with the interrogator coil (b) Equivalent circuit of Voltage variable capacitor

In fig. 2.7(a), an equivalent circuit of the sensor coil with induced emf from coupling with interrogator coil is shown. Here, Ls, Rs and Cs are the coil inductance, the series resistance and the parasitic capacitance respectively. Fig. 2.7(b) shows an equivalent circuit of the voltage variable capacitor in which Cp is the junction capacitance, which varies with applied voltage and Gp is the parallel conductance. However, Rs and Gp are considered as losses (Bhadra, S., 2010).

The impedance of voltage variable capacitor in the above fig. 2.7(a) is given as (Bhadra, S., 2010),

$$Z_S = \left(G_p + j\omega C_p\right)^{-1} \quad (2.\ 2)$$

If the losses are small, $G_p \ll \omega C_p$, then the impedance Z_T can be approximated by

$$Z_T \cong j\omega L_S + \frac{1}{j\omega(C_s+C_p)} + R_s + \frac{G_p}{\omega^2(C_s+C_p)^2} \quad (2.\ 3)$$

At resonant frequency, the imaginary part of Z_T goes to zero when

$$f_0 = \frac{1}{2\pi\sqrt{L_s(C_s+C_p)}} \quad (2.\ 4)$$

Usually, $C_s \ll C_p$ then the eqn. 2.4 becomes

$f_0 = \frac{1}{2\pi\sqrt{L_s C_p}}$, where f_0 is the coupled sensor resonant frequency.

Another parameter in interest is the quality factor (Q-factor) of the sensor circuit in fig. 2.7 (a) shown as (Bhadra, S., 2010),

$$Q = \omega_0 \left(\frac{R_s}{L_S} + \frac{G_p}{(C_p+C_s)}\right)^{-1} \quad (2.\ 5)$$

In fig. 2.8, an equivalent circuit of the sensor coil coupled with interrogator coil is shown in which the impedance, Z_{T1}, is measured from the source end. Here, L_I, R_I, C_I and M are the interrogator coil inductance, the series resistance, the parasitic capacitance and the mutual inductance between the interrogator and the sensor coil accordingly. The resonant frequency of the coupled coil is estimated using a frequency sweep and measuring the real part of the impedance from the source end. The impedance looking from the source end in fig. 2.8 is given as (Bhadra, S., 2010),

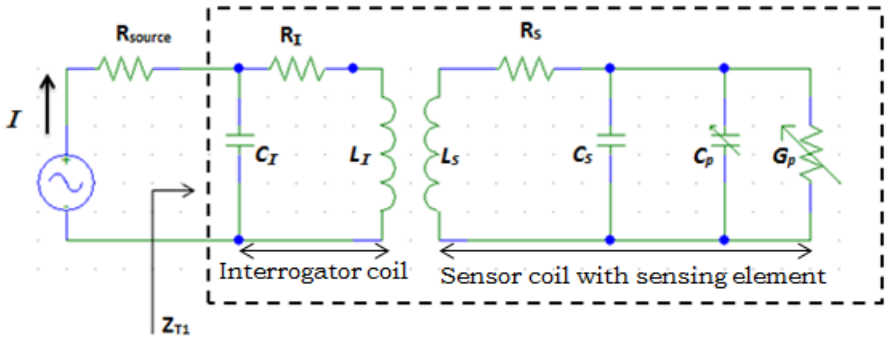

Figure 2. 8: Equivalent circuit diagram of the sensor coil coupled with the interrogator coil in which impedance looking from the source end

$$Z_{T1} = R_I + j\omega L_I + \frac{\omega^2 M^2}{Z_T} \quad (2.\ 6)$$

Where, $\frac{\omega^2 M^2}{Z_T}$, is the reflected impedance of the sensor coil from the source end.

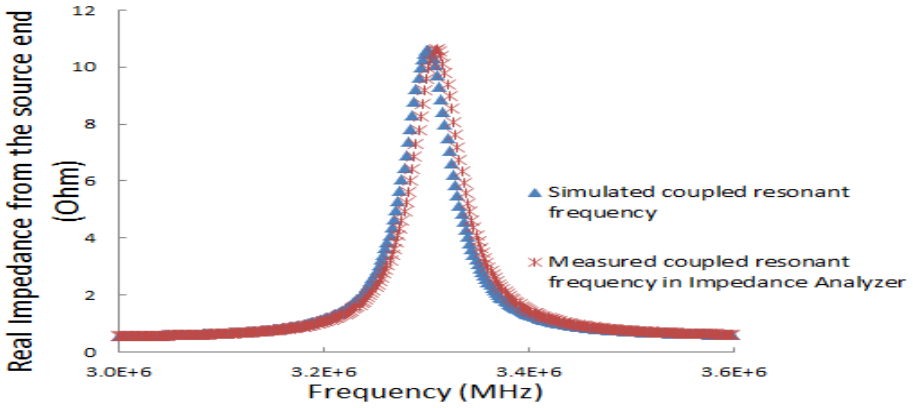

Figure 2. 9: Simulated value of Frequency vs. Real impedance in frequency domain

Fig. 2.9 shows a comparison between the measured and the simulated coupled resonant frequency of the sensor in frequency domain analysis. The simulated resonant frequency is 3.3028 MHz and the measured frequency in impedance analyzer is 3.3088 MHz, which has 6 kHz deviation from the simulated value. This may be due to the sensor resonant frequency using impedance measurement technique being affected by the local background.

2.3.2 Equivalent Circuit Model of Sensor in Transmit & Receive Mode

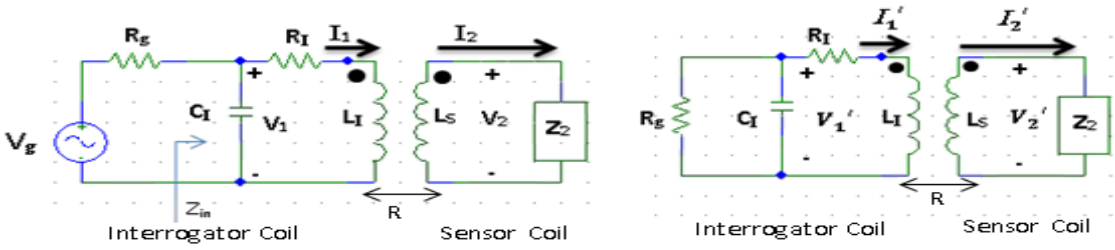

(a) (b)

Figure 2. 10: (a) Equivalent circuit diagram in Transmit mode (b) Equivalent circuit diagram in Receive mode

Fig. 2.10 shows the equivalent circuit diagram for transmit and receive mode of coupled coil sensor. Phasor analysis is used to determine the amplitude of the received signal. Here, the derivation of the received signal is not shown in details which can be found in S. Bhadra, 2010. Only the amplitude of the received signal is given from the receive mode which is of interest.

$$V_1' = \frac{\omega_0 \omega M^2 R_g}{(Z_T Z_R + \omega^2 M^2) Z_R \,|_{\omega_0}} V_g \qquad (2.7)$$

where, $Z_T = Z_2 + j\omega L_s$, $Z_2 = R_s + \frac{1}{j\omega(C_s + C_p) + G_p}$, $Z_R = R_g + R_I + j\omega L_I$ is the interrogator impedance, M is the mutual inductance between the interrogator and the sensor coil and ω is the source frequency (Bhadra, S., 2010).

Under small coupling assumption

$\left(\frac{\omega^2 M^2}{Z_T \,|_{\omega}} \ll Z_R \,|_{\omega}\right)$, then $V_1' \cong \frac{R_g V_g}{Z_R \,|_{\omega_0} Z_R \,|_{\omega}} \left(\frac{\omega \omega_0 M^2}{Z_T \,|_{\omega}}\right)$

V_1' is maximum when $\omega \approx \omega_0$ and $|Z_T|_{\omega_0}$ is minimum. In order to determine the resonant frequency, ω_0, the source frequency, ω, is swept near ω_0 and the maximum received signal, V_1', is obtained using a peak fitting algorithm (Bhadra, S., 2010).

2.3.3 Sensor and Interrogator Coil Modeling Including Mutual Inductance

For a fixed source frequency to excite the sensor, the received signal from the sensor under weak coupling condition $Z_T Z_R >> \omega^2 M^2$, will be proportional to M^2. Thus the received signal and the separation distance between sensor and interrogator coil are directly related to mutual coupling. The self-inductance, L, of sensor or interrogator coil can be approximated in terms of the wire radius, r_w, the loop radius, r, and the number of turns, *n*, as (Tesche, Ianoz & Karlsson, 1997)

$$L = n^2 \mu_0 \sqrt{r(r - r_w)} \left[\left(\frac{2}{k} - k \right) K(k) - \frac{2}{k} E(k) \right],$$

Where

$$k^2 = \frac{4r(r - r_w)}{(2r - r_w)^2} \tag{2.8}$$

K (k) and E (k) are the complete elliptic integrals, which are given below

$$K(k) = \int_0^{\pi/2} \frac{d\phi}{\sqrt{1 - k^2 \sin^2 \phi}} \tag{2.9}$$

$$E(k) = \int_0^{\pi/2} \sqrt{1 - k^2 \sin^2 \phi}\, d\phi \tag{2.10}$$

In the sensor we have used a voltage variable capacitor which has a known capacitance range. The sensor resonant frequency range has been chosen and using the known value of capacitance, we have estimated the required the sensor coil inductance using the eq^n. 1.15. When the sensor's desired inductance is found, then the designer can choose the number of turns, loop radius and wire radius to achieve it. Usually, the self-resonant frequency of both sensor coil and interrogator coil is much larger than coupled resonant frequency.

The mutual inductance, M, for two concentric circular coil can be expressed in terms of the loop radius of the interrogator coil, r_I, the loop radius of the sensor coil, r_S, separation distance between the centers of two coils, D, the number of turns of the interrogator coil, n_I, and the number of turns of the sensor coil, n_S, as (Tesche, Ianoz & Karlsson, 1997)

$$M = n_I n_S \mu_0 \sqrt{r_I r_S}\left[\left(\frac{2}{k1} - k_1\right) K(k_1) - \frac{2}{k_1} E(k_1)\right] \quad (2.11)$$

where

$$k_1{}^2 = \frac{4 r_I r_S}{D^2 + (r_I + r_S)^2} \quad (2.12)$$

If the separation distance between two coils is large, $(r_I + r_S) \ll D$, then the eq^{n}. 2.11 can be expressed as

$$M = \frac{n_I n_S \mu_0 {r_I}^2 {r_S}^2}{2D^3} \quad (2.13)$$

From eq^{n}. 2.13, it can be seen that

$$M \propto \frac{1}{D^3} \quad (2.14)$$

Therefore, the mutual coupling factor, m, between interrogator coil and the sensor coil can be defined in terms of the self-inductance of the interrogator coil, L_I, the self-inductance of the sensor coil, L_S , and the mutual inductance between the two coils, M, as

$$m = \frac{M}{\sqrt{L_I L_S}} \quad (2.15)$$

A MATLAB source code for calculation of the mutual inductance and coupling factor is provided in Appendix A.

2.4 Modeling of the Printed Circuit Board (PCB) Sensor

As will be discussed later in the thesis, printed circuit board technology was chosen as a low cost mass producible sensor technology for a corrosion sensor. A printed circuit board (PCB) sensor modeling is shown in fig. 2.11. The PC board is designed by using EAGLE 6.1.0 CAD software.

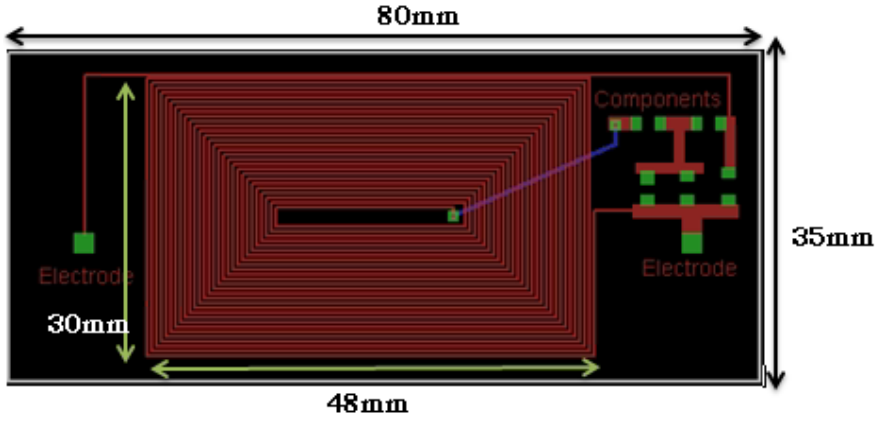

Figure 2. 11: Schematic diagram of Printed Circuit Board (PCB) Sensor

The dimension of the PCB board is 8cmx3.5cm. The designed parameters of PC board are 27 turns rectangular spiral inductor of total length 268.24cm, 0.254 mm conductor trace width, 0.254 mm spacing between conductors trace and 0.07 mm conductor thickness. Moreover, it includes two electrodes and the required components for the sensing circuit. The inductance of the rectangular coil is calculated by calculating the inductance of a square inductor coil and then multiplied by a shape factor (Tang, He, Pan& Chow, 2006). This formula is derived through modifying the duality of inductance and capacitance $lc = \varepsilon_o \mu_o$ of transmission line theory with the assistance of synthetic asymptote and analytical moment method (Tang, He, Pan& Chow, 2006). Since the inductance is dependent on magnetic fields, coil inductance is largely independent of the substrate dielectric. Therefore, the inductor may be assumed in free space with the effect

of added spiral gaps and ground plane (Tang, He, Pan& Chow, 2006), (Tang & Chow, 2002). First of all, the capacitance formula in free space with ground is derived and then the inductance formula is obtained. When the substrate thickness, h→∞, the far ground plane has little effect on the spiral inductor (Tang, He, Pan& Chow, 2006). Compared to the substrate thickness in the above design, we may assume that the spiral inductor has far ground plane and the inductor is in a homogeneous free space without ground (Tang, He, Pan& Chow, 2006).

2.4.1 Capacitance derivation in free space using the far asymptote of substrate thickness h

Consider a solid trapezoidal quarter-plate in free space which is shown in (fig. 2) Tang, He, Pan& Chow, 2006; the capacitance formula is defined based on the "root of area" (Tang & Chow, 2002)

$$C_{1/4\,solid} = c_{f1}\varepsilon_0\sqrt{8\pi A_{1/4}} \tag{2.16}$$

where, $A_{1/4} = {b_2}^2 - {b_1}^2$ is the area of quarter-plate solid trapezoid, $2b_1 = d_{out} + S$ and $2b_2 = d_{in} + S$ are the effective widths of the trapezoid, S is the inductor trace spacing; c_{f1} is the unknown shape factor of the trapezoid obtained by a precise curve fitting from a number of square spiral inductors. Also, d_{out} and d_{in} are the outer most and inner most dimension of the coil respectively.

$$c_{f1} = 1.07(b_1/b_2)^3 - 0.92\left(b_1/b_2\right)^2 + 0.3\left(b_1/b_2\right) + 0.82 \tag{2.17}$$

The area of each quarter spiral of the spiral inductor is divided into N x M equal square segments of area $W_s{}^2$, each segment has a conducting-area WW_s plus the surrounding gap-area , as shown in (fig. 3) Tang, He, Pan& Chow, 2006 .

Here, N is the number of turns, $M = {(b_2 + b_1)}/{W_s}$ (with $W_s = W + S$) is the average number of segments along a straight spiral arm and W is the turn width. In the above design, a grid is formed with a small conducting sub-area deleted from each square segment on a solid plate (Tang, He, Pan& Chow, 2006).

Then the far asymptote of the capacitance of the quarter-spiral is given below

$$C_{1/4far} = \frac{1}{\left[\frac{1}{\left|{1}/{c_{f1}\varepsilon_0\sqrt{8\pi A_1/_4}}\right|} + \frac{(\Delta p_{11} - \Delta p_{110})}{NM}\right] - \frac{1}{4\pi r_0 \varepsilon_0}} \tag{2.18}$$

Where, $r_0 = \frac{4(b_1{}^2 + b_1 b_2 + b_2{}^2)}{3(b_1 + b_2)}$, is the distance of the two centroids of the two opposing trapezoids. Moreover, $\Delta_{p_{11}}$ and $\Delta_{p_{110}}$ are the self-potentials of a segment in grid form and the solid plate form of the quarter-plate respectively (Tang, He, Pan & Chow, 2006)

$$\Delta_{p_{11}} = \frac{1}{c_f \varepsilon_0 \sqrt{8\pi W W_s}} \quad \& \quad \Delta_{p_{110}} = \frac{1}{c_f\, \varepsilon_0 \sqrt{8\pi W_s{}^2}}$$

Where, the shape factor c_f = 0.865 accounting for the charge singularities along only two edges in each segment along the spiral. However, the shape factor, c_{f1} , from eqn. 2.18 is given as a function of fill ratio, $\rho = \left(\frac{d_{out} - d_{in}}{d_{out} + d_{in}}\right)$, (W. tang, X. He & T. Pan, 2006)

$$c_{f1} = 0.90571 + 0.49425e^{-\rho/0.12253} \quad (2.19)$$

2.4.2 Inductance calculation using synthetic asymptote and transmission line duality

The spiral inductor formula is derived in eqn. 2.20 using eqn. 2.18 and transmission line duality, $L = \left(\mu_0 \varepsilon_0 / C\right)(\Delta l)^2$ (Tang, He, Pan& Chow, 2006)

$$L_{sq} = 4\frac{\mu_0 \varepsilon_0}{C_1/4far} N^2 (b_1 + b_2)^2 \quad (2.20)$$

Where, $(b_1 + b_2)$ is the average length of the spiral arms in trapezoid, the factor 4 comes from the four quarter spiral.

2.4.3 The Shape factor for Rectangular Spiral Inductor

Spiral inductors such as rectangular, octagonal or circular can be changed to square spiral inductors by keeping the metal area, the turn width, the turn spacing and the number of turns unchanged (Tang, He, Pan & Chow, 2006). Therefore, the inductance of a square spiral inductor is converted to a rectangular spiral inductor by multiplying with a shape factor i.e.

$$L = l_f L_{sq} \quad (2.21)$$

Here, L is the inductance of the rectangular spiral inductor, L_{sq} is the inductance of the square spiral inductor and l_f is the shape factor (Tang, Zhu, & Chow, 2006).

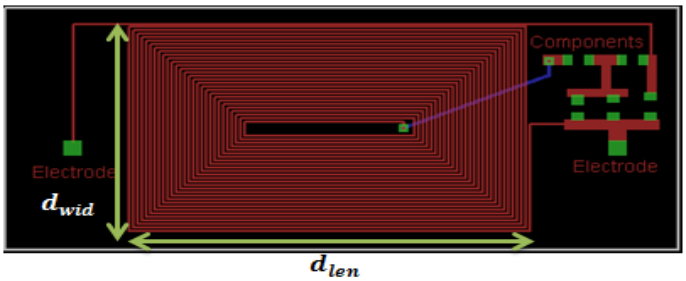

Figure 2. 12: Schematic diagram of Printed Circuit Board (PCB) Sensor with outmost length and outmost width

In fig. 2.12, a schematic diagram of designed PCB sensor with outmost length d_{len} and outmost width d_{wid} is shown in which the number of turns N, the turn spacing S, metal area A, and turn width W are kept same as the square spiral inductor. The shape factor, l_f, is from 0.92 to 1.0 for $\left({}^{d_{len}}/_{d_{wid}}\right) = 2:1$ to 1:1. It varies slowly (8%) in a relative large range of ${}^{d_{len}}/_{d_{wid}}$. So, the shape factor can be taken as a constant (e.g., 0.96) in the range of $\left({}^{d_{len}}/_{d_{wid}}\right) \leq 2:1$ and may not produce large error (Tang, He, Pan & Chow, 2006).

2.5 Comparison of the measured and the simulated inductance

2.5.1 Simulated Rectangular Spiral PCB inductance

In the above fig. 2.12, the number of turns N is 27, the turn spacing S is 0.254 mm, the turn width W is 0.254 mm, the outmost length d_{len} is 48mm and the outmost width d_{wid} is 30mm. However, the area of the rectangular spiral inductor is given as,

$$A_{rect} = d_{len}d_{wid} = 48 * 30\ mm^2 = 1440mm^2 \quad (2.22)$$

Here, the metal area for both shape are kept same i.e., $A_{rect} = A_{sq}$. So, the outmost diameter of the square spiral inductor is given as,

$d_{out} = \sqrt{48 * 30}\, mm$ = 37.947 mm

Using an online inductor calculator, the innermost diameter, d_{in} , of square spiral inductor is 10.007mm. The calculated capacitance for square spiral inductor using eqn. 2.18 is 0.9169pF and the inductance using eqn. 2.20 is 21.921 μH.

From fig. 2.12, the ratio of outmost length and width is

$$\left(\frac{d_{len}}{d_{wid}}\right) = \frac{48}{30} = 1.6 \leq 2:1$$

So, the shape factor, $l_{f,}$ is taken as a constant which is 0.96. Using eqn. 2.25, the simulated rectangular Spiral PCB inductance is 21.044 μH. A MATLAB code is provided in the last part of this thesis in appendix A1.

2.5.2 Measured inductance in Precision Impedance Analyzer (Agilent 4294A)

In fig. 2.13, the PCB inductor measurement set up is shown. The inductance of the rectangular spiral PCB inductor is extracted in precision impedance analyzer by tracking the low frequency 40Hz to 500 kHz measurement. The measured inductance for PCB inductor is 20.33 μH, which is close in agreement with the simulated value. The error in the calculation is 3.4% which is acceptable.

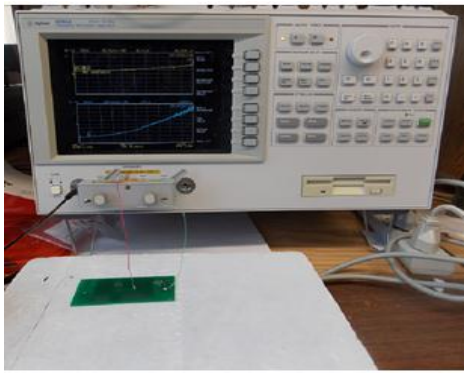

Figure 2. 13: The rectangular spiral PCB inductor measurement set up in Impedance Analyzer (Agilent 4294A)

2.6 Summary

Finally, chapter 2 summarizes the circuit modelling of the sensor and the sensor design on the PCB. It also presents the characterization of sensor performance in a time domain gating system (TDGS) and an impedance analyzer. Moreover, it shows the comparison of the measured and the simulated results of the sensor performance.

Chapter 3: Fabrication Technique of wireless passive corrosion sensor

3.1 Introduction

In this chapter, the fabrication technique, design parameters, and optimization of corrosion sensors are demonstrated. For optimization of sensors with extended separation distance between the sensor and the interrogator coil, different methods have been used, such as by using different types of wire, different size of the interrogator coil and different types of plastic for making the coil. As a result, the optimization process includes the improvement of separation distance, Q factor and lessening the environmental effects on the sensor performance. Here, the encapsulation technique of a cylindrical shape and a printed circuit board (PCB) based design are presented.

3.2 Optimization Process of the Sensor

3.2.1 Choice of Plastic materials

In the very beginning of our fabrication procedure, plastic materials were chosen for constructing the sensor coil. The plastic materials are characterized based on the loss and the Q factors of the sensor coil. However, other parameters are concerned to optimize the sensor performance. Fig.3.1 shows two different low cost plastics which have different thickness and diameter are enwrapped by equal number of wire turns (0.0195") and the end terminals of the wire are connected with a 33pF fixed capacitor. It forms a series RLC resonant circuit whose resonant frequency, f_0 ,can be estimated using eqn. 2.4.

Figure 3. 1: (a) ABS (Acrylonitrile butadiene styrene) plastic enfolded by 0.0195" wire (b) PVC plastic material enfolded by 0.0195" diameter wire

The measured inductance of the two coils is slightly different and the dielectric properties of two materials are different; thus the resonators have slightly different resonant frequency. Fig. 3.2 describes an impedance analyzer measurement of an inductor coil with a 33pf fixed capacitor using both PVC and ABS plastic material.

In fig. 3.2, the quality factor of both sensor coils is estimated based on -3dB points using eqn. 3.1. The Q-factor of the resonators using ABS plastic or PVC pipe type with 33 pf fixed capacitor are respectively 55 and 90. As per the Q factor values of the sensor using both plastic materials, it can be concluded that ABS plastic has greater electrical losses than white plastic.

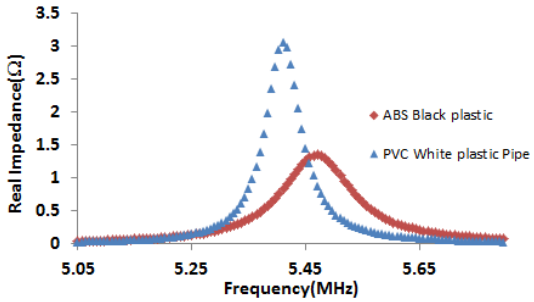

Figure 3. 2: Frequency vs. Real Impedance graph of the sensors using both PVC and ABS Black plastic materials

This may be due to the use of carbon block to fix the black ABS.

$$Q = \frac{f_0}{\Delta f} \tag{3.1}$$

Here, $\Delta f = f_2 - f_1$, f_2 and f_1 are respectively the higher and the lower 3-dB points measured from the peak.

In fig. 3.3, a fixed capacitor test set-up is shown in Impedance Analyzer. The measured capacitance was 33.004 pF and the conductance, $G_{p,}$ was 252.301nS, which is considered as the inherent loss. The inherent loss of the capacitor is so small that it has negligible effect on the Q-factor of the sensor.

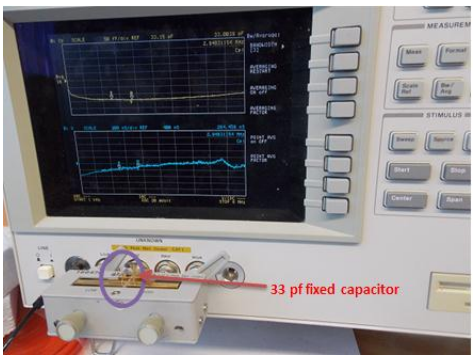

Figure 3. 3: Capacitor testing in Impedance Analyzer (Agilent 4294A)

In our design process, two materials were chosen for enduring the harsh environment of the reinforced concrete structure for a long period of time. These two materials are 3" diameter Schedule 80 PVC Rigid Non-metallic Conduit (RNC) with extra heavy wall and 4" diameter Schedule 40 PVC pipe which are shown in section 3.3.1.

3.2.2 Choice of the sensor coil wires

Several easily available insulated wires were evaluated for fabricating the sensor coils which are two different size of PVC insulated BELDEN manufactured wires and another one is PDVF (Polyvinylidene Fluoride). The wire diameters are 0.059" (8530-

009-1000), 0.036” (9976-002-1000) and 0.0195” inches. Fig. 3.4 demonstrates the different types and size of the wire.

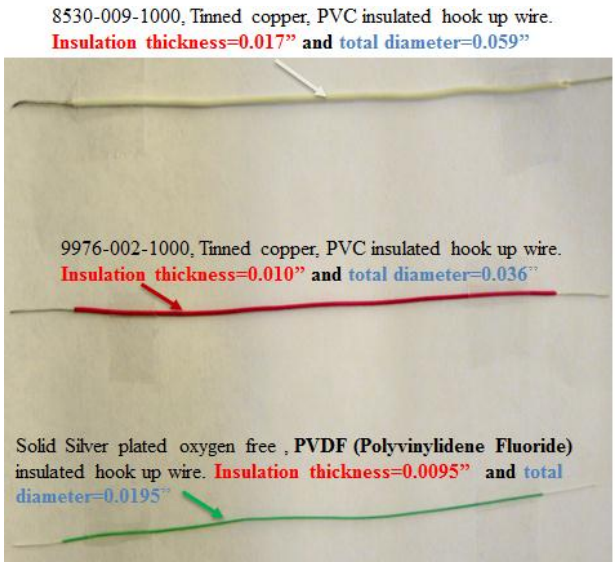

Figure 3. 4: Different types of wire chosen for building sensor coil

Fig. 3.5 shows resonator coil with a fixed capacitor made by three different diameter wires. The wires were tightly wrapped around PVC pipe. The number of turns of the resonator coils was chosen to make the inductance closure of each coil.

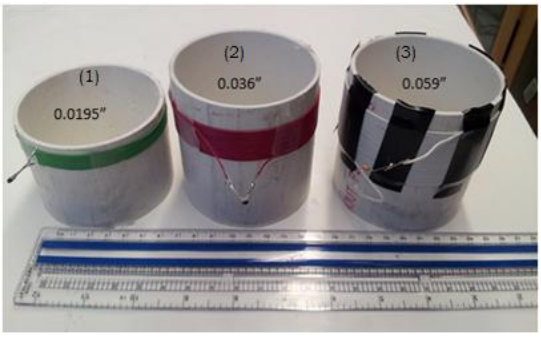

Figure 3. 5: Resonator coil with different types of wire

The diameter of the green, the red and the white wires were respectively 0.0195”, 0.036” and 0.059”. The number of turns for the green, the red and the white wires were

consequently 19, 22 and 25; the measured inductances were 60.2µH, 56.94µH and 55.69µH respectively.

However, the self-resonant frequencies of the above three resonator coils were accordingly 13.375MHz, 16.62MHz and 51.613 MHz. Therefore, the estimated parasitic capacitances using eqn. 3.2 for above coils are respectively 2.35pF, 1.61pF and 3.18pF.

$$f_{self-resonant} = \frac{1}{2\pi\sqrt{L_S C_{parasitic}}} \tag{3.2}$$

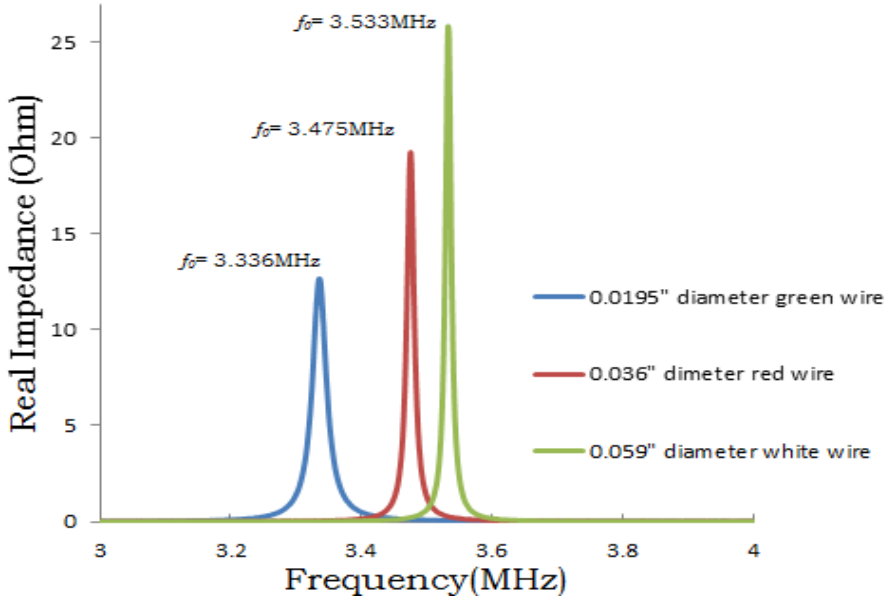

Figure 3. 6: Impedance Analyzer measurement of three resonator coil with fixed capacitor

Fig 3.6 demonstrates some results of three fixed capacitor resonator coils with separation distance, 6 cm, between the resonator and the interrogator coil. Using 5 cm diameter and 5 turns of the interrogator coil, the estimated Q for the above coils using eqn. 3.1 are 103, 402 and 507 respectively. For the size constraints of the sensor, the

0.036” red wire was chosen for the optimized design because the coil widths for the green, the red and the white wires were 1cm, 2.1cm and 4 cm accordingly.

3.2.3 Choice of Reference Electrode

During the sensor construction process, regular black steel grades 400R and stainless steel grade 308/316 were used as two electrodes. As a reference electrode, stainless steel grade 308/316 does not provide good performance in corrosion progress. Therefore, GRADE 2205 DUPLEX stainless steel made by “Salit steel” was chosen for the optimized sensor design. It has a microstructure of austenite and ferrite (duplex) due to its chemical balance (Salit Steel, 2010). Moreover, the addition of nitrogen provides strength levels close to 80% higher than 304 with superior corrosion properties. Chromium and molybdenum content alloy provides superior pitting and crevice corrosion properties and excellent stress corrosion cracking resistance (Salit Steel, 2010). A prototype design of the complete optimized sensor is shown in fig. 3.14.

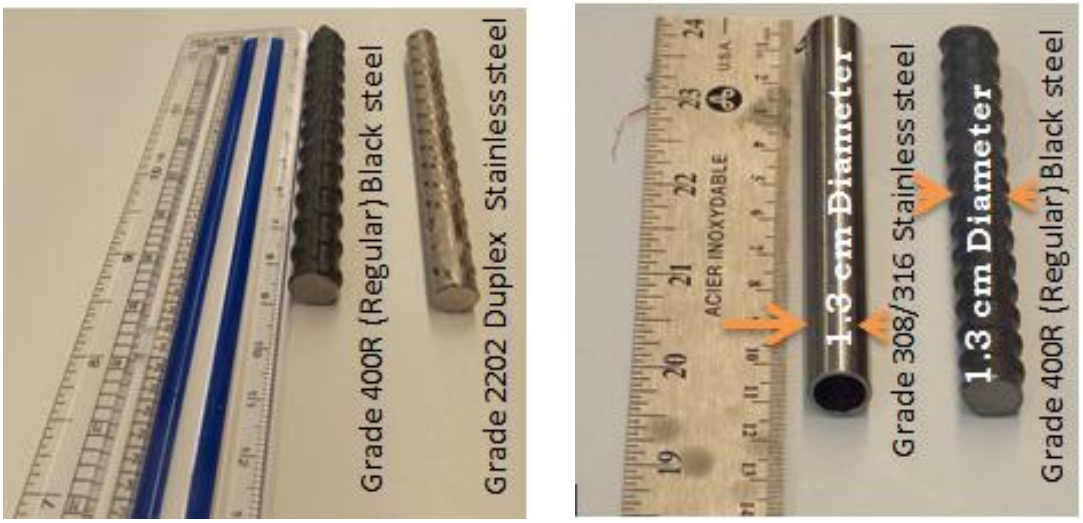

Figure 3. 7: Two types of stainless steel are used for reference electrode and black steel is the reinforcement bar

3.2.4 Size of the Interrogator coil

Several different size interrogator coil dimensions were evaluated to determine the effect on the interrogation distance. The different diameter coils 5cm, 8.4 cm, 11 cm, 14 cm and 17cm were used and the best outcome was chosen based on the energy coupled through the interrogator coil to the sensor coil. The interrogator coils had a different number of turns and making of interrogator coils needed some careful considerations, such as the self-resonant frequency of the interrogator coil should be differed large enough from the coupled sensor resonant frequency otherwise it may overlap with the coupled sensor signal leading to an error of the desired signal. Moreover, large number of turns of the interrogator coil may reduce the freedom of controlling the source voltage to avoid the nonlinearity of the varactor diode in the sensing circuit. Fig. 3.8(a) shows five different diameters of interrogator coil made with different number of turns which were used in the sensor optimization process.

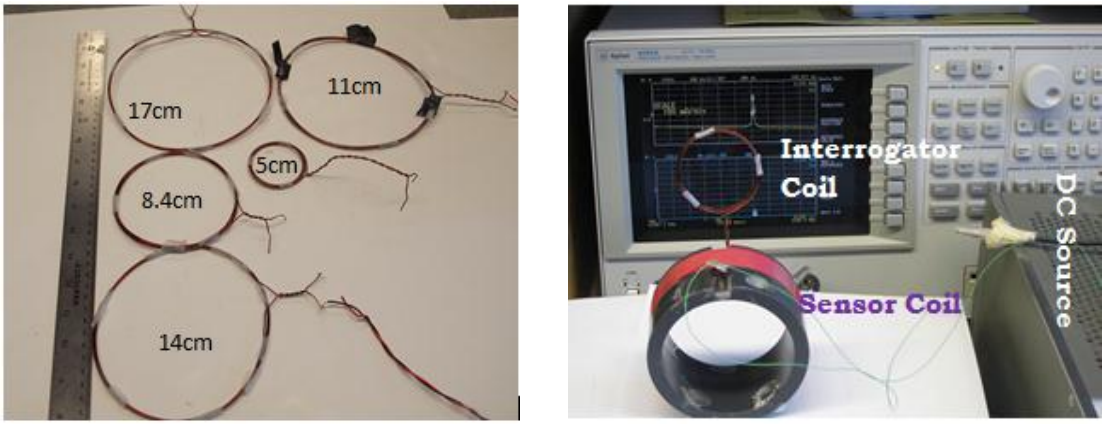

Figure 3. 8: (a) Different Diameter Interrogator coil (b) A prototype coupled sensor measurement set up in Impedance analyzer

Table 3.1 describes the impedance analyzer measurement of the sensor using different interrogator coil in which the resonant frequency, separation distance and mutual coupling are shown.

Table 3. 1: Improved separation distance between the sensor and the interrogator coil and their mutual coupling using different size of the interrogator coil

Interrogator coil diameter (cm)	Separation distance between the interrogator and the sensor (cm)	Resonant frequency (MHz)	Calculated mutual coupling (m) between the interrogator and the sensor coil
5	7	3.4001	0.0313
	10	3.4073	0.0137
	12	3.4073	0.0086
8.4	8	3.3900	0.0376
	10	3.3940	0.0229
	12	3.4001	0.0148
	15	3.4001	0.0084
11	10	3.4073	0.0309
	14	3.4107	0.0141
	20	3.4140	0.0056
14	8	3.3900	0.0522
	14	3.4007	0.0169
	17	3.4007	0.0106
	20	3.4007	0.0070
17	9	3.3923	0.0455
	12	3.4023	0.0272
	14	3.4023	0.0198
	15	3.4023	0.0171

In table 3.1, the mutual coupling was estimated using the measured parameters shown in appendix A.3.

If the interrogator coil's size is same or slightly larger than the sensor coil and it should be concentrically coupled with the sensor coil, then the extended separation distance with optimized Q using 0.036" wire was found. From table 3.1, the maximum separation distance of 20 cm with an obtainable resonant peak with a resolution of 0.83 kHz/mV and 0.84 kHz/mV corresponds to voltage of 8 mV and 13 mV (with respect to

10 cm and 8cm for 11 cm and 14 cm diameter interrogator coils) were achieved for both 11 cm and 14 cm interrogator coils respectively.

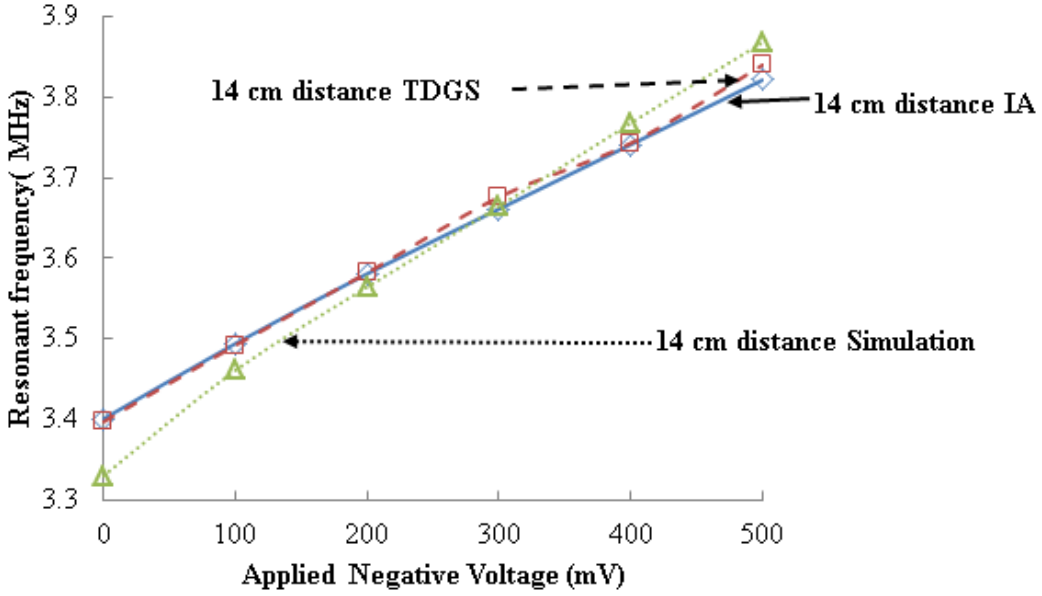

Figure 3. 9: Comparison of different measurement for 14cm diameter interrogator coil

Some results of the coupled sensor coil are shown in fig. 3.9, fig. 3.10 and fig. 3.11 using 14cm and 17cm diameter interrogator coil. Here, a controlled DC voltage was applied to the sensing circuit instead of corrosion voltage produced from two electrodes embedded in the mortar/concrete. Then an external interrogator coil tracked the sensor resonant frequency with a separation distance of 14cm.

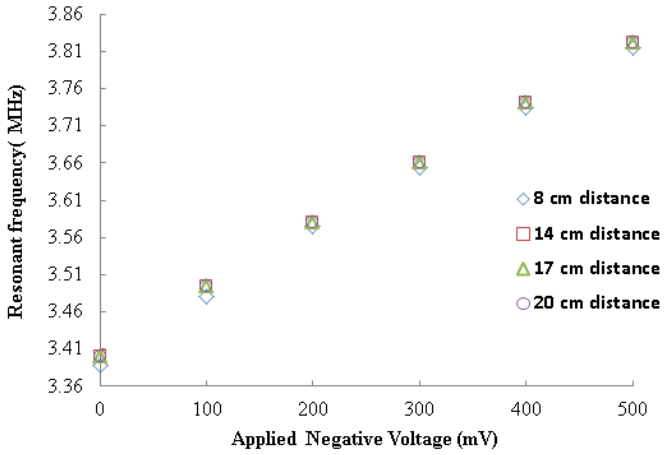

Figure 3. 10: Comparison of different separation distance for 14cm diameter interrogator coil

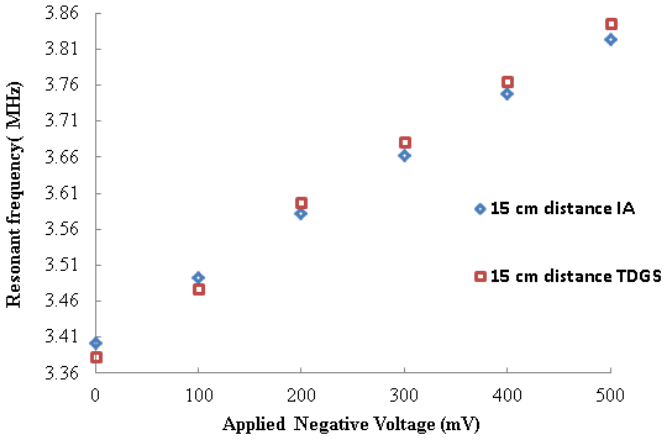

Figure 3. 11: Comparison of Impedance Analyzer and TDGS measurement for 17cm diameter interrogator coil

Both time domain interrogation and impedance measurement technique were used to measure the sensor response. Furthermore, measured results were being compared with a spice simulation.

3.3 Fabrication and Encapsulation Technique of optimized sensor

Two types of geometry for sensor fabrication are studied here. First of all, the sensor was fabricated using a cylindrical (open hoop based) shape PVC pipe and tested

inside the concrete structure. But for design simplicity and miniaturization of the sensor, it was fabricated on printed circuit board (PCB) contains the planar inductor coil and surface mount circuit elements. Moreover, most of our tests were carried out on PCB sensors which are given in chapter 4.

3.3.1 Cylindrical Shaped Sensor

In fig. 3.12(a), an open hoop designed sensor is shown. Here, schedule 80, 3" diameter extra heavy wall PVC nonmetallic conduit was used for making the sensor which can withstand the long-term harsh environment of concrete.

(a) (b) Step-1

Figure 3. 12: (a) PVC conduit schedule 80 (b) PVC conduit schedule 80 plastic enfolded by 0.036" wire

Step-2 Step-3 Sensing Circuit

Figure 3. 13: Sensor Fabrication in different steps (Thomson, Perveen, Bridges, & Bhadra, 2012)

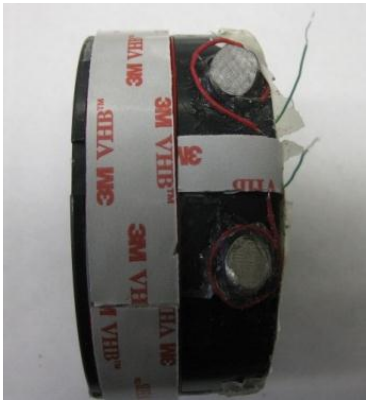

Step-4

Step-5- An encapsulated sensor which is ready to be embedded

Figure 3. 14: Sensor Encapsulation Technique (Thomson, Perveen, Bridges, & Bhadra, 2012)

Fig.3.12 (b) and fig.3.13 show the fabrication steps of the optimized sensor. In step-2, the two electrodes are fixed inside the hole and the gap was filled by RTV silicon. In step-5, the sensing circuit was fixed in the slot by NHP 112 0807 Industrial Grade non-conductive epoxy, the connection of two electrodes with the sensing circuit done by MG Chemicals 8331 conductive silver epoxy. In step-4, a foam tape 3M 4941 -4952 was used to cover the coil and the sensing circuit. Step-5 shows a fully encapsulated sensor which is ready to be embedded in the concrete structure. There is no possibility of crevice corrosion because the edge of both electrodes was sealed in potting compound. Here, the sensor made in step-4 was positioned inside another schedule 40, 4" diameter white PVC nonmetallic conduit and the gap was sealed by MG Chemicals black epoxy 832B. The black potting compound is highly water resistant, chemical resistant and non-conductive acts as an electrical insulator (MG Chemicals, n.d.). In step-5, the clear aperture through the sensor allows the diffusion of ions from below and above (Thomson, Perveen, Bridges, & Bhadra, 2012).

3.3.2 PCB sensor

With the experience gained from the cylindrical sensor and the need to address the existing structures, the sensor was fabricated on single layered printed circuit board. The fabricated sensor on PCB allows the unimpeded transport of reactants from surroundings to the electrodes. The sealing technique for PCB sensor protection was chosen by testing different options under different environment conditions.

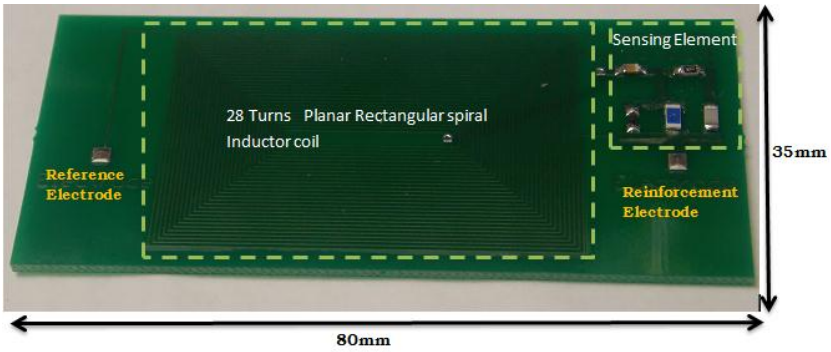

Figure 3. 15: Printed Circuit Board based sensor with sensing element (Perveen, Bridges, Bhadra, & Thomson, 2013)

The printed circuit board contains 28 turns planar rectangular coil with an area of 48mm x 30 mm. Fig 3.16 shows the PCB sensor response under different operating conditions. However, the sensor response under different operating conditions and their results has described in details in chapter 5. This chapter only describes the fabrication and sealing technique for PCB sensor.

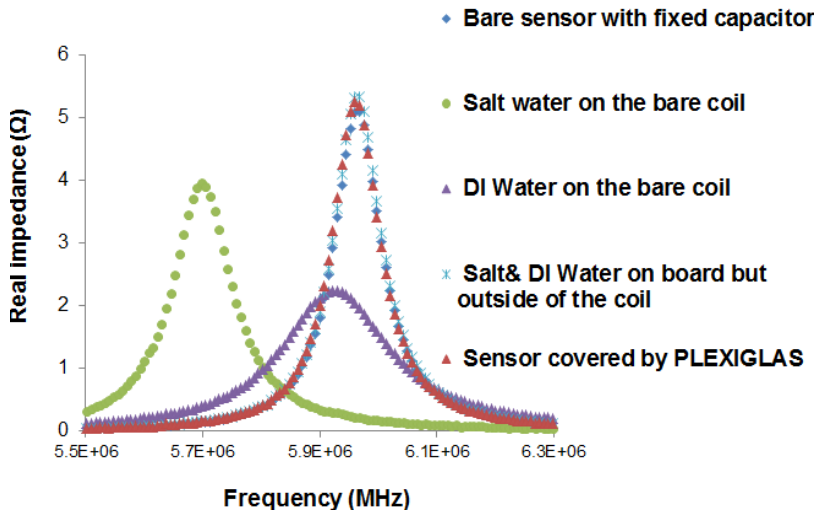

(a)

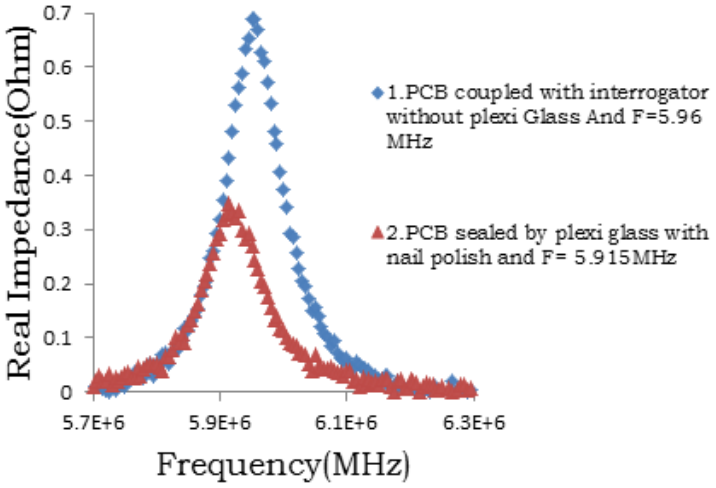

(b)

Figure 3. 16: PCB sensor results in Impedance Analyzer under different environment condition

The plotted measurement curve in fig. 3.16(a) demonstrates the PCB sensor resonant frequency change interacting with the different environment condition. First of all, a bare sensor has been tested in the impedance analyzer, and then tested with DI water and salt water. The variations come from the dielectric permittivity changes (Heidari & Azimi, 2011), (Ong et al., 2008).

3.3.2.1 PLEXIGLAS sealing (2×1.5mm Thick)

The sensor was sealed by 1.5 mm thick PLEXIGLAS. The encapsulation were done in several steps; sensor coil was sealed by 48 mm x 30 mm PLEXIGLAS and PCB back was sealed by 80 mm x 35 mm which were bonded with nail polish (Sally Hansen Hard as Nails Xtreme Wear). The electrode size is 10 mm x 10 mm shown in fig.3. 17 (b).The electrodes were bonded with the sensing circuit using MG Chemicals 8331 conductive silver epoxy (Perveen, Bridges, Bhadra, & Thomson, 2013).

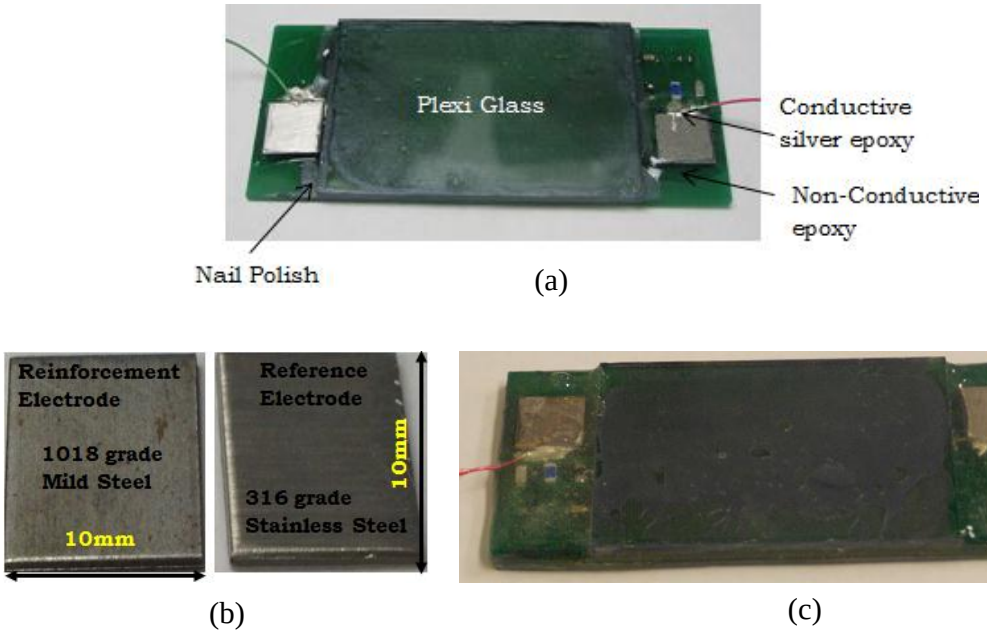

Figure 3. 17: Encapsulation process of printed circuit board based corrosion potential Sensor

The sensing circuit and the exposed area on the top of the sensor were sealed by NHP 112 0807 Industrial Grade non-conductive epoxy. The sensor was left for 2 hours long to cure the epoxy properly. Fig 3.17 describes the encapsulation process of the sensor and a complete encapsulated PCB sensor is shown in 3.17(c). The measurement result in fig. 3.16(b) describes the sensor resonant frequency shift using the encapsulation

related to the fig. 3.17(a) in which the PCB back was not sealed by PLEXIGLAS. The completely sealed sensor ready to be embedded in the mortar/concrete drops the resonant frequency ~ 45-55 kHz as shown in fig. 3.17 (c).However, this enclosing technique with the PCB sensor shifts the baseline of the sensor ~245-425 kHz embedded in the mortar and the Q factor of the sensor drops from 75 to 20, gives a very poor performance and corresponds to a potential shift of ~150.31-260.74 mV (Using sensor sensitivity of ~1.63 kHz/mV). Therefore, three different techniques for sensor sealing are described in sec. 3.3.2.2, 3.3.2.3 and 3.3.2.4. The choice of the hermetic enclosure for sensor protection is explained in detail in chapter 5. To measure the sensor performance in the mortar/concrete, the corrosion potential from the resonant frequency was compared with the directly measured potential at the electrodes. Hence, two wire connections for each sealed sensor were made from the two electrode connection come out from the mortar specimen facilitating the comparison of the directly measured potential and the extracted potential from the resonant frequency giving a better understanding of sensor performance.

3.3.2.2 PLEXIGLAS Sealing (6mm Thick)

Here, 6mm thick PLEXIGLAS were used for sensor sealing instead of 1.5 mm PLEXIGLAS which are shown in fig 3.18. The sealing procedures are same as described in sec. 3.3.2.1. However, the electrode size was 10mm×30mm bonded by conductive silver epoxy with the sensing circuit. This PLEXIGLAS adds a resonant frequency drop of~90-100 kHz at zero bias.

(a)PCB Board with Sensor coil

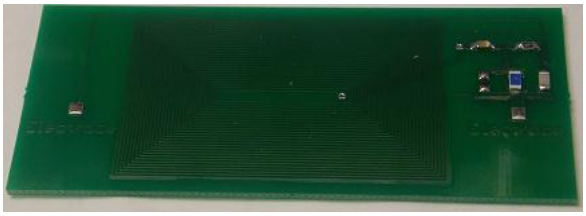

(b) PCB coil connected with sensing element

(c) PCB back sealed by PLEXIGLAS

(d) PCB top coil & back sealed by PLEXIGLAS

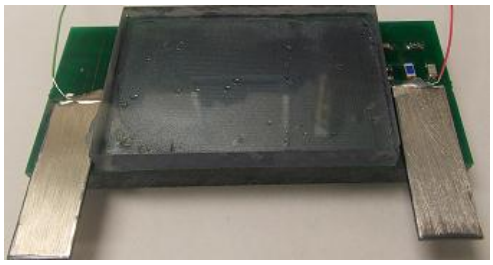

(e)PCB sensor with Electrode connection

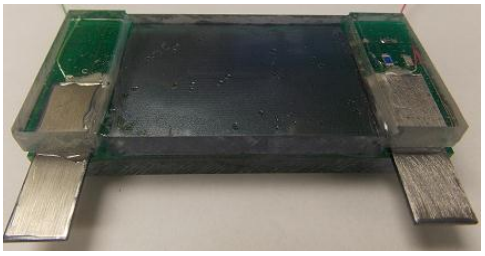

(f) Sealed PCB sensor Back and Top

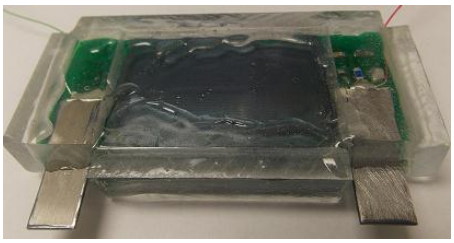

(g) Sealed PCB sensor ready to be embedded in the mortar specimen

Figure 3. 18: PCB sealing step using 6mm Thick PLEXIGLAS

After sealing the sensor, the electrodes were sandblasted using glass beads to avoid any kind of corrosion substances may come during installation and handling of the sensor. The edge of the electrodes were coated by nail polish (Sally Hansen Hard as Nails Xtreme Wear) to avoid the crevice corrosion (Zhang, Forsyth, Hinton & Wallace, 2011).

3.3.2.3 PLEXIGLAS (2×6 mm Thick) with air gap sealing

In fig. 3.19 (c), the sensor was sealed as the same dimension as PCB board 6mm thick hollow (4mm chopped off from inside) PLEXIGLAS as a cap covering PCB bottom and top of the inductor coil to reduce the fringing fields into the surrounding materials. The edge of the plexi glass was bonded with the PCB using nail polish (Sally Hansen Hard as Nails Xtreme Wear) and epoxy (NHP 112 0807 Industrial Grade). Electrodes are connected with the sensing circuit using conductive silver epoxy (MG Chemicals 8331). The edge of the PC board are sealed by industrial grade non-conductive epoxy (NHP 112 0807 Industrial Grade). Only extended portion of two electrodes of size 15mm×10mm×1.575mm were left contact with the concrete. This sensor sealing technique adds a resonant frequency drop of ~10-15 kHz at zero bias.

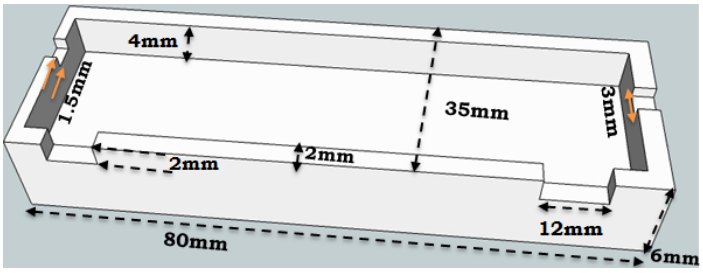

(a) Top Cap

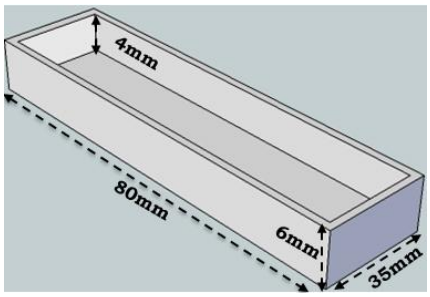

(b) Bottom cap

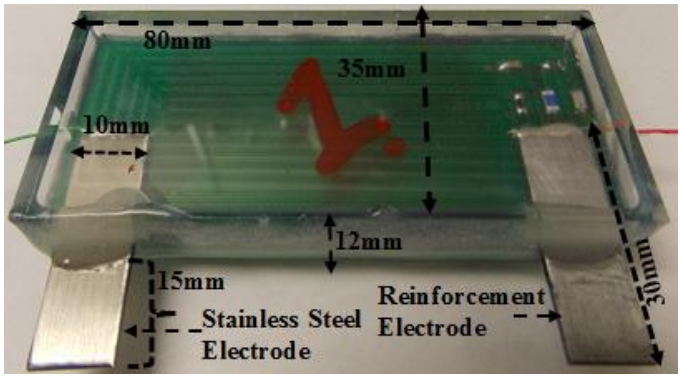

(b) Sealed Sensor Ready to be embedded

Figure 3. 19: Hollow PLEXIGLAS Sealed Sensor

3.3.2.4 Epoxy sealing (6 mm thick)

Fig. 3.20(b) shows a non-conductive epoxy (NHP 112 0807 Industrial Grade) sealed sensor. All the connections were made same as the hollow PLEXIGLAS sealed sensor, only non-conductive epoxy was used to seal the sensor using a mold shown in fig. 3.20(a). The sensor was left open for one day to set the epoxy properly. The epoxy thickness on top, bottom and two sides of PCB sensor was 6mm. Only extended portion of two electrodes of size 15mm×10mm×1.575mm were left contact with the concrete. This non-conductive epoxy drops the resonant frequency ~120-130 kHz.

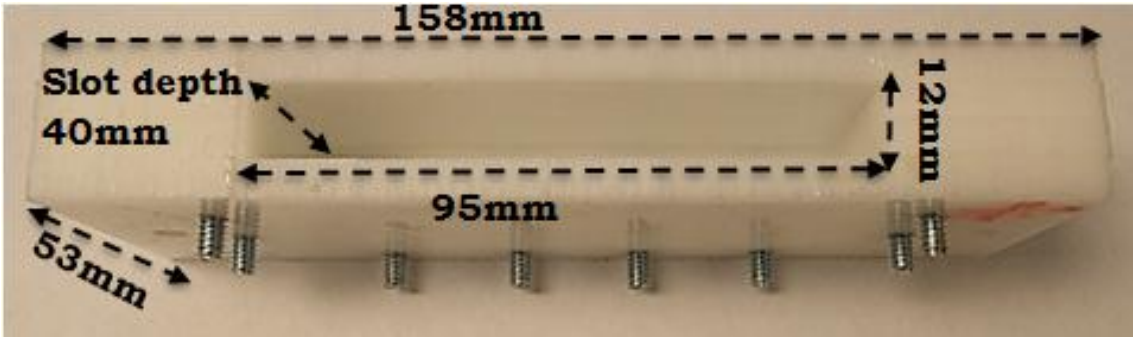

(a)

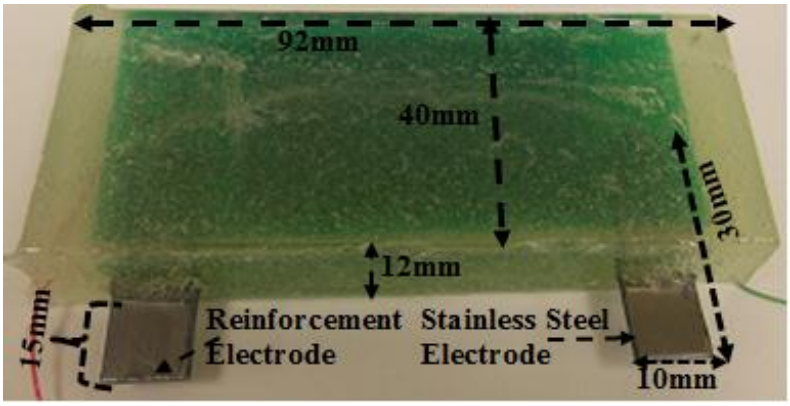

(b)

Figure 3. 20: (a) Mold for Epoxy Sealing (a) Epoxy Sealed Sensor ready to be embedded

Table 3. 2: Summary of sealing materials on PCB sensor response at zero bias

Sealing Technique	Frequency Shift(Δf=kHz)	Capacitance Change (ΔCp=pF)	Q-factor (fo/Δf)
PLEXIGLAS(2×1.5mm Thick)	~45-55	~0.536-0.656	~78-82
PLEXIGLAS(2×6mm Thick)	~90-100	~1.084-1.207	~78-82
Hollow PLEXIGLAS(2×6mm Thick)	~10-15	~0.118-0.177	~78-82
Epoxy Sealed (6mm Thick)	~120-130	~1.456-1.582	~72-79

Table 3.2 shows the effects of encapsulation technique on the sensor response. The above table concludes that if there is some air gap between the sensor coil and the enclosure, then it shows minimal shifts of resonant frequency and fringing capacitance explained in detail in chapter 5.

3.3.2.5 Some Results for Bare and Sealed Sensor

Fig. 3.21 shows a horizontally and a slightly tilted PCB sensor coupled with a 5 cm diameter interrogator coil in impedance analyzer.

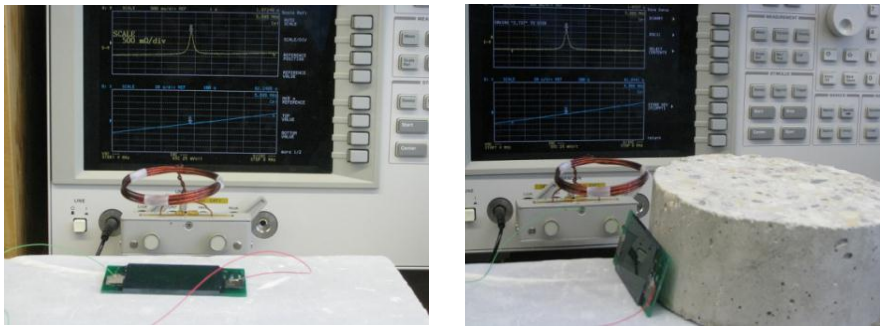

(a) Horizontally coupled sensor (b) Tilted Sensor

Figure 3. 21: PCB sensor test set-up in precision Impedance Analyzer (Agilent 4294A)

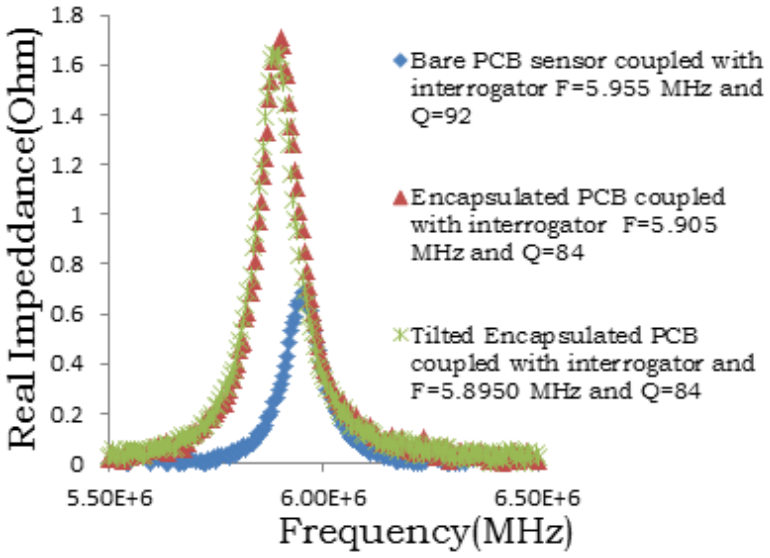

Figure 3. 22: Impedance Analyzer measurement results of both Encapsulated and Bare sensor

Fig. 3.22 defines the measured result of bare sensor, encapsulated sensor and tilted sensor in impedance analyzer which has 10 kHz variations corresponding to ~6.135 mV between horizontally placed and tilted sensor.

3.4 Summary

In conclusion, chapter 3 shows the fabrication techniques of the two geometrical designs, the cylindrical shaped sensor and the PCB sensor. It also demonstrates the optimization process of the cylindrical shaped sensor. Furthermore, it shows different encapsulation techniques for the PCB sensor.

Chapter 4: Results of the Cylindrical Shaped Sensor under different operating conditions

4.1 Introduction

The sensor response has been characterized under different test conditions. A controlled DC voltage was applied across the varactor at each step of the sensor encapsulation to embedment of the sensor for calibrating purposes. Inaccurate measurement leads to an error of sensor response which could affect the result. In this process we studied the encapsulation and environmental effects on the two geometries of sensor tested as part of this thesis. PCB sensor results are presented in chapter 5. Chapter 4 compiles the cylindrical shape sensor response under different operating conditions as well as the accelerated corrosion test of the cylindrical shape sensor in the new structure.

4.2 Sensor response Under Different Operating Conditions

4.2.1 Fixed Capacitor Model

The cylindrical shaped sensor response was tested with a 33pFfixed capacitor instead of the sensing circuit with the varactor (NXP BB202) diode junction capacitance at zero bias to reduce the uncertainty. These tests were carried out in a precision impedance analyzer (Agilent 4294A). From fig. 4.1, when the sensor coil (L_s=63.52μH, R_s=20.1Ω, C_p=2pF, n_s= 22 turns) was bare and kept in the air, the sensor resonates at a frequency of 3.3108 MHz with the fixed capacitor. The losses are small and the quality factor of the sensor is ~207, as determined based on a 3dB point. The sensor is an open hoop design in which the electrodes were fixed inside the hoop allows the easy flow of

reactants through the hoop. So the tests were done using salt and tap water inside the hoop. For testing purposes, a bottle with no water was put inside the coil/hoop leading to a drop of 6.7 kHz from 3.3108 MHz and Q-factor was ~190. Salt water was used to simulate the lossy dielectric medium of wet concrete. The conductivity of the salt water was measured by Agilent 85070E dielectric probe kit, where performance probe was used to determine the conductivity. At 22 °C room temperature, the conductivity was 103.7 mS/cm at 379.6 MHz. Furthermore, another low frequency (several kHz) conductivity meter was used to measure the conductivity of the salt water. At 21.2° C room temperature, the conductivity of the salt water was 111.2 mS/cm. Changes in the surrounding medium lead to the sensor's resonant frequency shift and the addition of loss causing the reduction of Q factor is related to the dielectric conductivity of the medium (Heidari & Azimi, 2011).

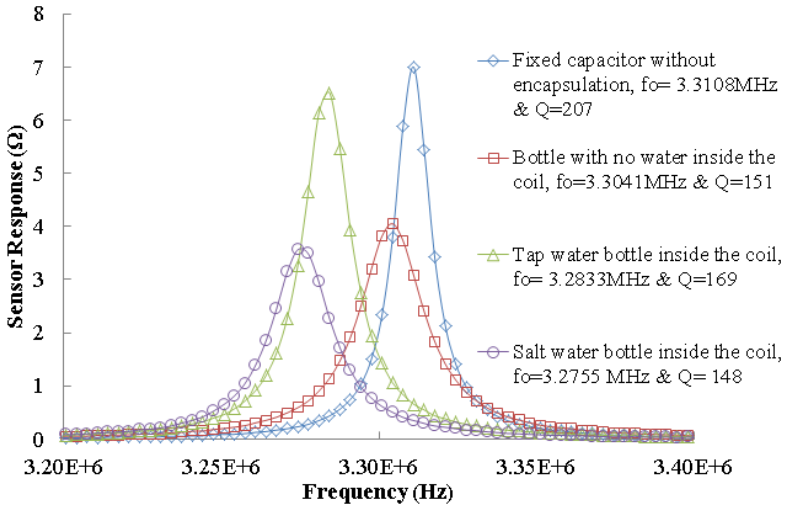

Figure 4. 1: Cylindrical shape sensor response with fixed capacitor under different operating conditions

Tap water with a bottle inside the coil added a frequency shift of ~20.79 kHz from 3.3108 MHz equivalent to a potential induced shift of 28.48mV. However, the frequency

shift arouse from salt water inside the coil was ~28.60 kHz from 3.3108 MHz equivalent to a potential induced shift of 39.18 mV and Q factor was ~148. As mentioned before, that open hoop design allows the easy flow of reactants to the electrodes referring to inevitable resonant frequency shift. The enclosing technique of the sensor to protect the coil and sensing circuit has been described in chapter 3 and the frequency shift arises from the sealing materials has shown in sec. 4.3.

4.2.2 Varactor Based Model

Fig. 4.2 shows the sensor response with the sensing circuit at zero bias under different operating conditions. The bare sensor resonates at 3.2647 MHz without perturbing by the surroundings. The empty bottle inside the coil/hoop added a frequency shift of 5.953 kHz from 3.2647 MHz giving an equivalent potential of 8.15mV.

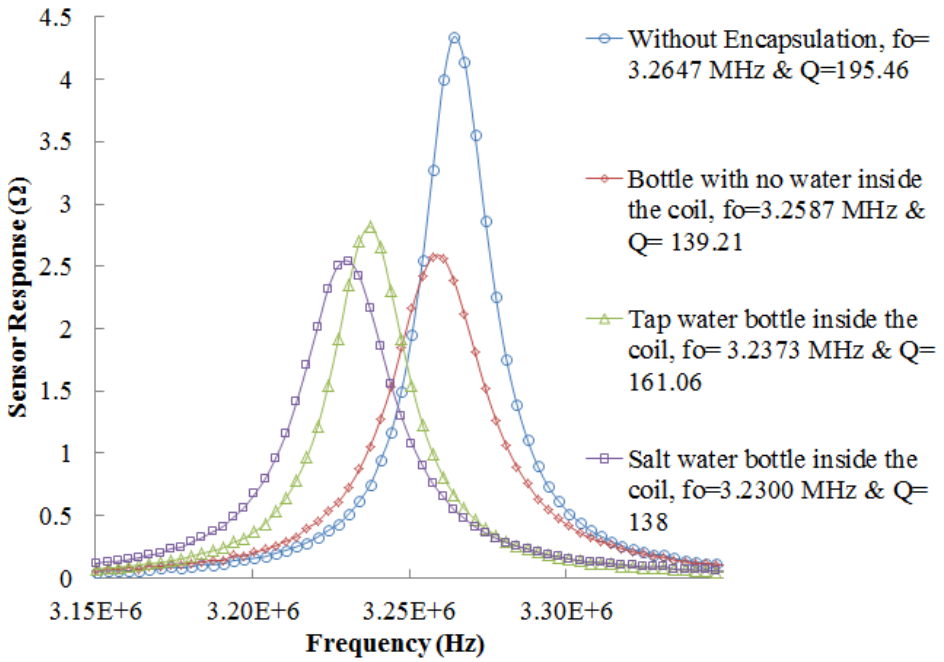

Figure 4. 2: Cylindrical shape Sensor response with sensing circuit under different operating conditions

Assuming the losses are small; salt and tap water caused a resonant frequency shift of ~27-35 kHz correspond to 36.99-47.95mV and the Q of the sensor response was ~ 138-161. The embedded sensor response at zero bias inside the concrete in presence of moisture, water and chlorides was simulated using salt and regular water causing a frequency drop of 409 kHz correspond to 560.274 mV. This geometrical design of the sensor inside the mortar/concrete gave a large base line shift. Therefore, for design simplicity and in an effort to improve repeatability the sensor was designed on the PCB as described in chapter 5.

4.3 DC Calibration on Cylindrical Shape Sensor

Initially a DC voltage was applied to the sensing circuit using a controlled DC voltage source to simulate the corrosion potential. The sensor coil was concentrically aligned with the interrogator coil (5cm diameter) with separation distance, d=7cm and the source amplitude, V_G was set to 5mV to avoid the nonlinearity of the sensor response. However, the cylindrical shaped sensor resonant frequencies as a function of applied negative voltage to the sensing circuit are shown in fig. 4.4.

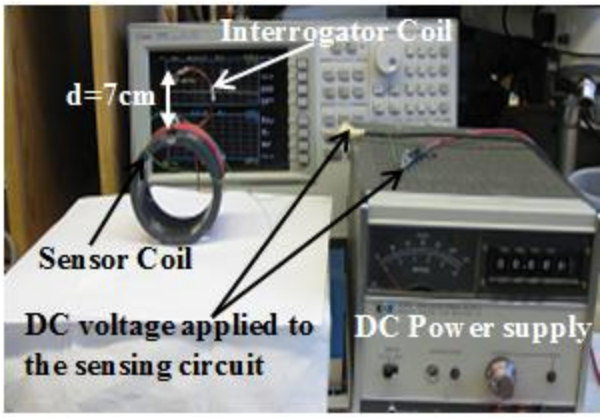

Figure 4. 3: A prototype DC voltage test set up on cylindrical shaped sensor

A prototype DC voltage test set up on cylindrical shape sensor (L_s=63.52μH, R_s=20.1Ω, C_p=2pF, n_s= 22 turns) where sensor coil is concentrically coupled with the interrogator coil is shown in fig. 4.3. The negative voltage applied to the sensing circuit in cylindrical shape sensor was varied 0 mV to 500 mV. It can be seen that from fig. 4.4, the linear curve fits well with the measured resonant frequency values. The slope of the linear curve is 0.0841MHz/100 mV. From the linear curve fit eqn. 4.1 is obtained which relates the negative voltage applied to the sensing circuit, *V* to the resonant frequency of the sensor, f_0.

$$V(mV) = 1188.5 f_0(MHz) - 4049.6 \quad (4.1)$$

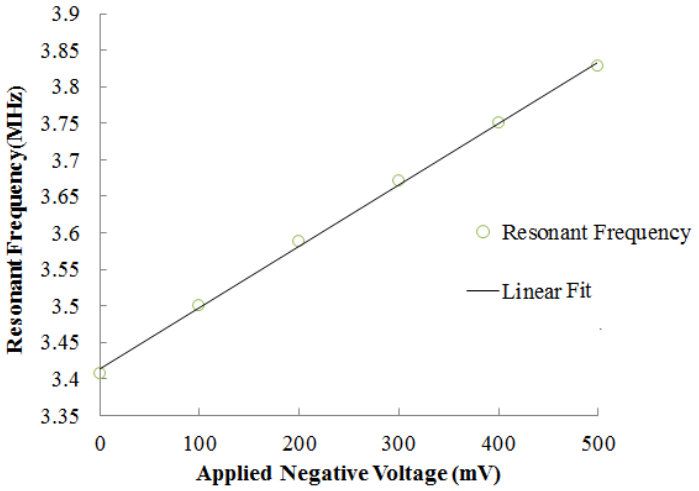

Figure 4. 4: Resonant Frequency as function of applied negative voltage to the sensing Circuit of Cylindrical Shape Sensor

The encapsulation procedure for the cylindrical shape sensor is explained in sec. 3.3.1. The materials (foam tape, potting compound, conductive silver epoxy, non-conductive epoxy, PVC Conduit) used for encapsulation leads to a frequency drop of <195 kHz. The error from the linear fit arises from the non-linear relation between C_j and V_c as seen from eqn.1.14 and higher order parasitic. Note that the source impedance in

this calibration is very small; whereas the galvanic cell produced from reinforcement steel/stainless steel embedded in concrete will have larger source impedance (Bhadra, Bridges & Thomson, 2010), (Perveen, Bridges, Bhadra, & Thomson, 2013).

Fig. 4.5 shows the resonant frequencies of the cylindrical shape sensor as a function of applied negative voltage is influenced by surrounding dielectric changes. The DC calibration on sealed sensor gives a slope of 0.073 MHz /100 mV from fig. 4.5. Therefore, from the linear curve fit eqn. 4.2 of the cylindrical shape sealed sensor was obtained which relates the negative voltage applied across the two electrodes connected with the sensing circuit, V to the resonant frequency of the sensor, f_0 .

$$V(mV) = 1369.9 f_0(MHz) - 4400.7 \tag{4.2}$$

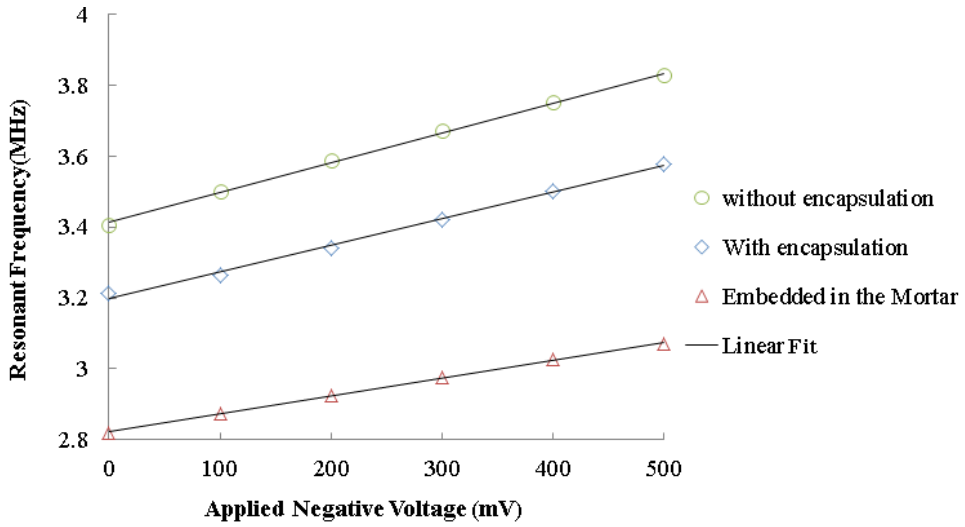

Figure 4. 5: Resonant Frequency vs. Applied negative voltage to the sensing circuit of cylindrical shaped sensor under different condition

Using equation 4.2, the frequency response of the embedded sensor in the mortar with applied negative DC voltage gives a conversion error of 12.73% and corresponds to a correction factor in voltage is 560.274mV.

Table 4. 1: Sensor response under different conditions

Condition of the sensor	Resonant Frequency (MHz)	Equivalent Voltage, ΔV, mV	Capacitance Change, ΔCp, pF	Q factor
Without Sealing	3.4073	N/A	N/A	~120
Sensor Sensitivity [Sealed]= 0.73 kHz/mV				
Sealed	3.2125	N/A	4.29	~80-100
Embedded in the Mortar Specimen	2.8035	560.3	16.39	~20-30

4.4 Comparison of results from Different System Measurements

In this section, the sensor response has been compared in Time Domain Gating System (TDGS) and Impedance analyzer (Agilent 4294A) to get a viable result of how the sensor response affected by the measurement instrumentation.

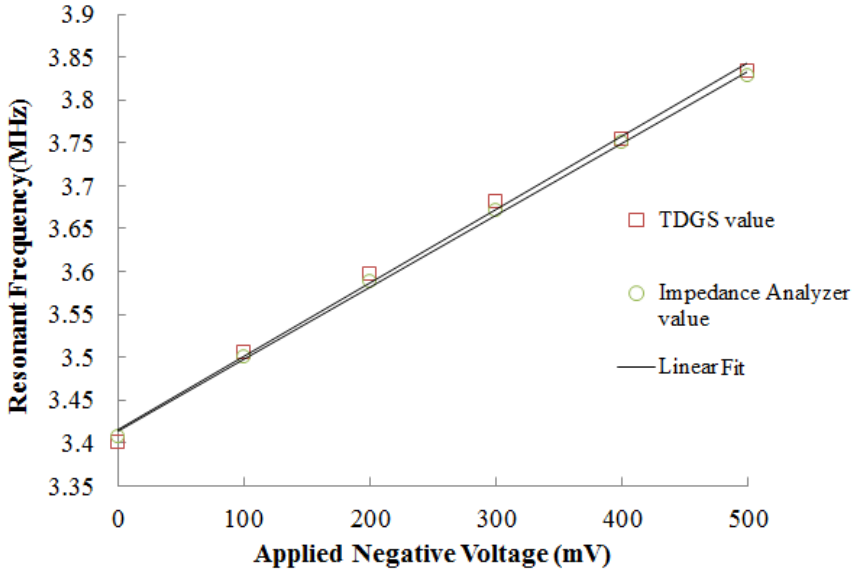

Figure 4. 6: Comparison of the cylindrical shaped sensor response without encapsulation in different measurement system

However, the operation principle of TDGS is beyond this thesis which was explained in details in Bhadra, S., 2010. Fig. 4.6 explains the cylindrical shape sensor

(L_s= 63.52μH, R_s = 20.1Ω, C_p = 2pF, n_s = 22 turns) response as a function of applied negative voltage to the sensing circuit in TDGS and Impedance Analyzer (Agilent 4294A). The cylindrical shape sensor coil was concentrically coupled with 11cm diameter interrogator coil (L_I = 6.212 μH, Rs = 0.721Ω, C_p = 23.3 pF, n_I = 5turns) with separation distance, d = 10 cm. Therefore, the slopes, 0.0866 MHz /100 mV and 0.0841 MHz /100 mV are obtained from the linear fit curve of TDGS and impedance analyzer measurement respectively. The measurement result of time domain interrogation has not affected by its surrounding environments unlike impedance measurement system. The estimated average measurement error, 0.185% which was 6.3 kHz deviation corresponds to 8.63 mV was found in Precision Impedance Analyzer (Agilent 4294A) comes from surroundings than time domain interrogation.

4.5 Sensor performance with distance

The sensor response was measured in an impedance analyzer to find out the sensor system performance with different distances. During this measurement the bandwidth of the system was set to 16.7 kHz and frequency was swept from 3.2 MHz to 3.4 MHz with 300 evenly distributed measurement points with no averaging. Fig. 4.7 shows the spectrum measured with the impedance analyzer at different interrogation distances. With this method the maximum interrogation distance where a measurable peak was obtainable was 20 cm which provides a 16.160 dB SNR at resonance as shown in table 4.2. The resonant frequency of the sensor was obtained using a curve fitting algorithm (Robinson & Clegg, 2005) having an average variation of ±1.71 kHz from 3.2643 MHz equivalent to 2.34 mV for different interrogation distance as shown in table 4.2.

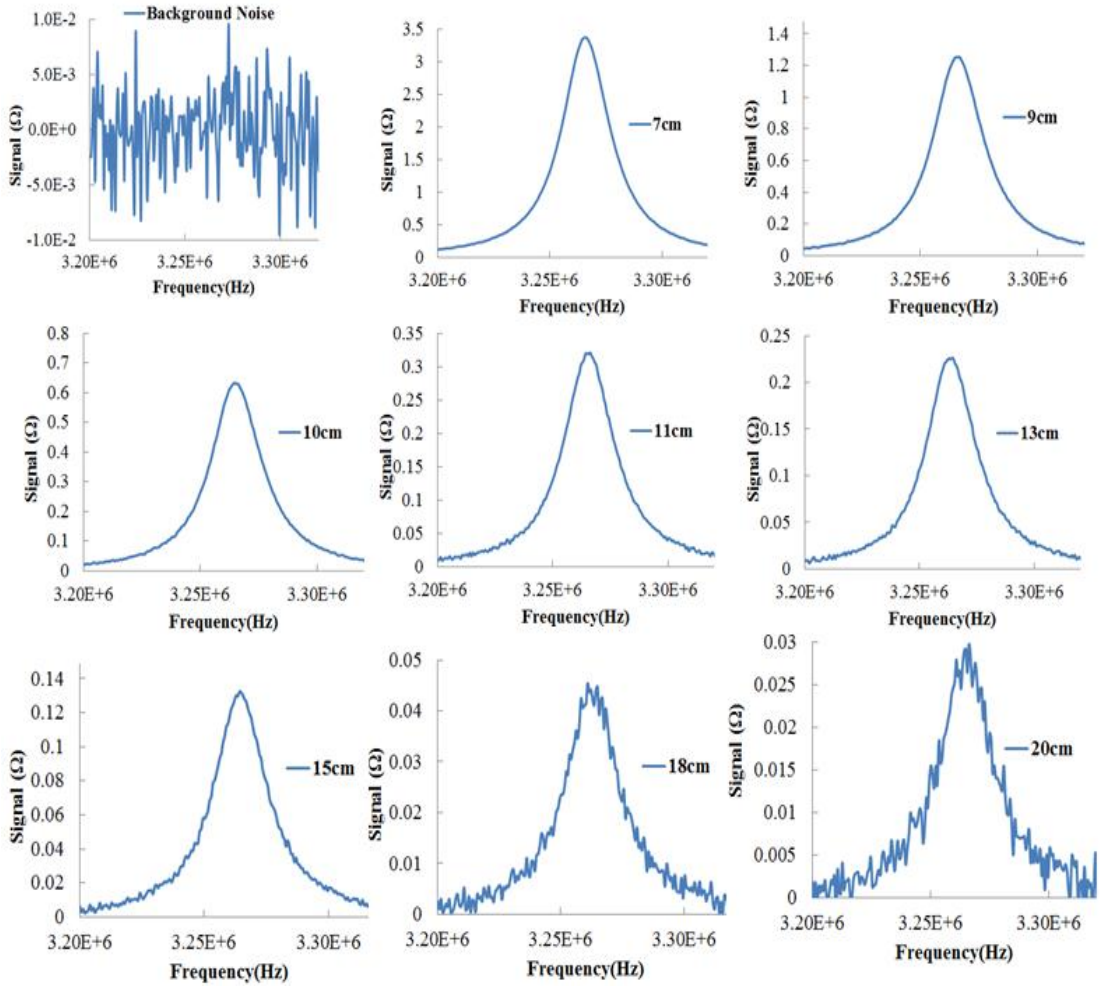

Figure 4. 7: Sensor Response with different interrogation distances in Impedance Analyzer

During this measurement the source voltage was varied several times to operate the sensor in the linear region. The source voltage was set to 25 mV for 13 to 20 cm, 15 mV for 10 to 11 cm, 10 mV for 9 cm and 5 mV for 7 cm. First the sensor performance was measured without changing the source voltage, 25 mV, and the obtained minimum separation distance was 13 cm. However, the separation distance can be increased by increasing the source voltage and increasing the number of turns of the sensor coil

(Sharmistha Bhadra and Douglas J Thomson and Greg, E. Bridges, 2013) but it imposes surrounding noise on the sensor signal.

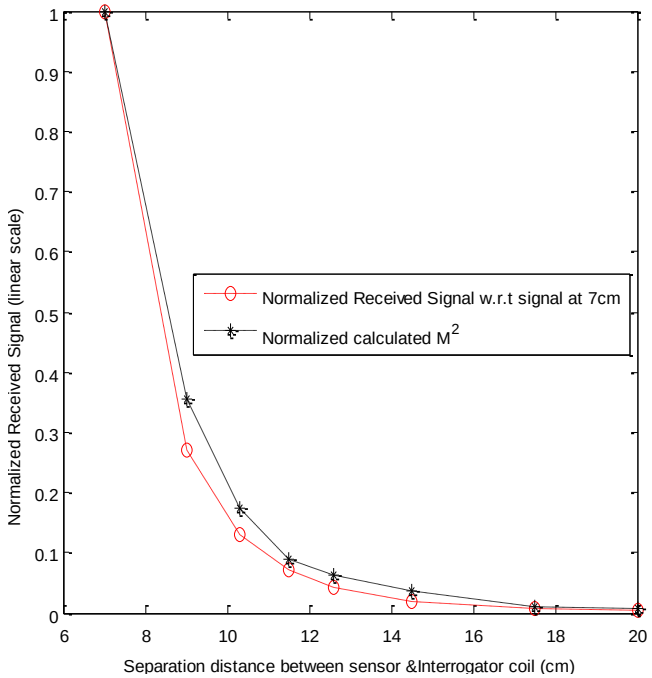

Figure 4. 8: Normalized Received Signal and M^2 for the sensor with distance

The mutual inductance, M between the sensor and the interrogator coil was calculated for different distances using eqn.2.11.

Table 4. 2: Resonant frequency and SNR for different distances for impedance Measurement (Concentrically coupled sensor)

Separation Distance(d=cm)	Resonant Frequency(MHz)	SNR(dB)
7	3.266	59
9	3.266	50
10	3.265	44
11	3.265	38
13	3.264	37
15	3.265	30
18	3.261	22
20	3.262	16

In section 2.3.2, it is already been mentioned that the signal from the sensor in the receive mode is proportional to the square of the mutual inductance, and the mutual

inductance is inversely proportional to the cubic of the separation distance. Thus, the received signal from the sensor drops sharply with increasing distance. The normalized received signal from the sensor for a fixed exciting frequency *f=3.2660* MHz is plotted in fig. 4.8 with the normalized M^2 value for different distances. Signal normalization is used to plot different scale data in single plot. From fig. 4.8, the normalized received signal is in good agreement with the normalized M^2, showing that the path loss follows the theory in section 2.3.2 (Bhadra, S., 2010).

4.6 Accelerated Corrosion Test

The development of passive wireless corrosion sensor for structural health monitoring is of growing interest. Corrosion is a major problem for civil infrastructure causing significant deterioration, increasing maintenance costs and decreasing safety (Koch, Brongers, Thompson, Virmani & Payer, 2001). One of the main reasons for active corrosion initiation is Cl^- ingress from the de-icing salt, which is extensively used in winter to keep roads clear of snow and ice (Ervin & Reis, 2008), (Montemor, Simoes, & Ferreira, 2003). If the structure is exposed in significant gradient of Cl^- environment then it is more prone to macro cell corrosion, especially when subjected to cycles of wetting and drying (Hope et al., 2001), (Yin, Hutchins, Diamond, & Purnell, 2010). However, Cl^- is one of the main responsible factors to initiate active corrosion in reinforced structure but it appears to play an indirect role to determine the rate of corrosion of steel reinforcement (Hope et al., 2001), (Yu, Chiang & Yang, 2012). The corrosion rate of the reinforcement steel is influenced by several environmental factors such as carbonation of the Portland cement paste, pH of the concrete pore water, availability of Oxygen, temperature, relative humidity which of all is interrelated (Hope et al., 2001). Normally,

concrete's inherent protective attributes provide excellent corrosion resistance to reinforcement steel by preventing the ingression of highly corrosive substances from the nature when it is properly designed for the service environment (Hope et al., 2001). This corrosion resistance is due to concrete being an electrolyte, where initially sound concrete maintains a very high pH in the range of 13.0 to 13.5 (Ervin & Reis, 2008), (Hope et al., 2001), (Apostolopoulos & Papadakis, 2008), (Du, Hu, Huang, & Lin, 2006). With this high pH concrete creates a tightly adhering thin film on the surface of the reinforcement, which passivates the steel and protects it from corrosion (Hope et al., 2001), (Apostolopoulos & Papadakis, 2008), (Du, Hu, Huang, & Lin, 2006), (Bhadra, Bridges, Thomson, & Freund, 2011), (ASTM C 876-91, 2006). This passive film does not stop the corrosion of steel, but reduces the corrosion to an insignificant level. Typically, the passive corrosion rate of the reinforcement steel is 0.1μm/yr.; the reinforcement steel would corrode at least thousand times higher with no presence of passive film (Hope et al., 2001). The ingression of chlorides in the civil structure alters the pH in the concrete and causes the passivation layer to become compromised at the level of pH (< 9.5). After a threshold pH level the reinforcement becomes active and corrosion initiation happens (Hope et al., 2001), (Du, Hu, Huang, & Lin, 2006), (Apostolopoulos & Papadakis, 2008). Once corroded, the load carrying capacity of reinforcing steel is reduced and also leads to secondary effects such as cracking, spalling (ASTM C 876-91, 2006), (Cabrera, 1996).

To test the corrosion potential sensor in the civil structure, the specimen where the sensor being embedded, are made of cement based mortar. This allows the easy diffusion of moisture, oxygen and chloride ions. By using cement based mortar the accelerated corrosion experiments can be carried out in months rather than years required for

concrete. However, the chemistry of the two materials is similar. Once the specimens are cured, they are submerged in a strong salt solution to provide a source of chloride ions. Therefore, oxygen, moisture, and chlorides are readily available at the surface of the reinforcing steel and the corrosion potential increase much more rapidly as opposed to the gradual potential change during a natural corrosion process.

4.6.1 Making of Mortar Specimen

The cylindrical specimen was made from Quickrete mason mix (type S mortar, no. 1136). The procedures of specimen block are shown in fig. 4.9. The encapsulated sensor which is ready to be embedded in the mortar specimen, demonstrated in sec. 3.3.1 in step 5. The two glass rods are used to support the sensor inside the mold. After thoroughly mixing of 2.720kg mortar with 420gm of water, the mortar paste was placed in the mold shown in fig. 4.9(b). The height and diameter of the specimen are 17cm and 15 cm respectively. The spacing between the reinforcement steel bar and the stainless steel electrode is 2.8 cm.

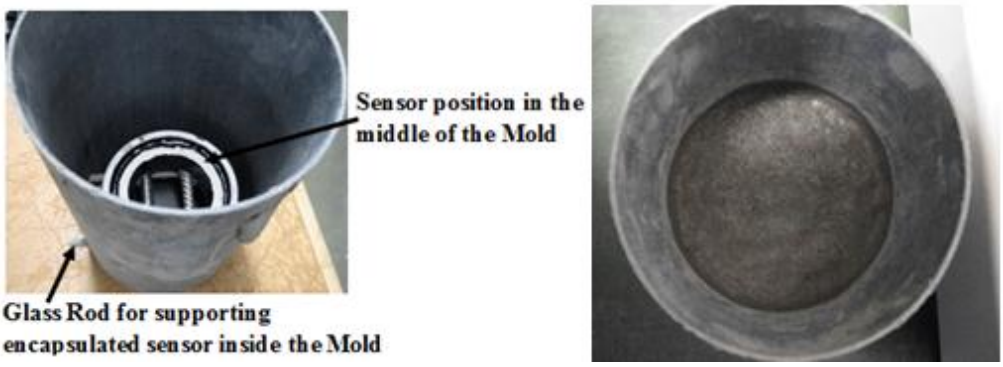

(a) (b)

Figure 4. 9: (a) Sensor position inside the Mold (b) Embedded Sensor in the Mortar specimen

The encapsulated sensor was embedded in the middle of the specimen, the two rebar were close to the bottom level of mortar than the top level, as shown in 4.9(a). However, the sensor coil was closer to the top level of mortar than bottom level. In fig. 4.10, the distance of 60 mm from the top and the bottom of the sensor, represents the distance from the encapsulated sensor (two end edge of the PVC pipe) level. After 7 days the specimen block was taken out from the mold. Then the specimen was air cured for 23 days. The stainless steel made with grade 2205 microstructure alloy (It has superior corrosion resistance than other stainless steel (Salit Steel, 2010)) is used as a reference bar which is more electropositive than reinforcement bar. Also this stainless steel and reinforcement bar is connected with the negative and positive ends of the sensing circuit elements respectively. After curing 23 days this specimen was submerged in water for 4 days and then in 5% NaCl solution (by weight of water) for the remainder of the test as shown in Fig. 4.10. The sensor coil was aligned concentrically with that of the interrogator coil (17 cm diameter) with a separation distance, d=8cm.

Figure 4. 10: A prototype experiment set up of cylindrical shape sensor in salt water bath

4.6.2 Results

The sensor's resonant frequency and the corrosion potential of the reinforcement steel, V_{cell} were monitored continuously. The corrosion potential generated from the reinforcement steel was determined from the sensor resonant frequency shift using eqn. 4.2 obtained from the DC calibration. Fig. 4.11 shows the direct measurement of cell potentials and the potentials that obtained from sensor resonant frequency. In this test, the specimen block was submerged 4 days in tap water and rest of the test was carried out in 5% salt (NaCl) mixed (by weight) tap water.

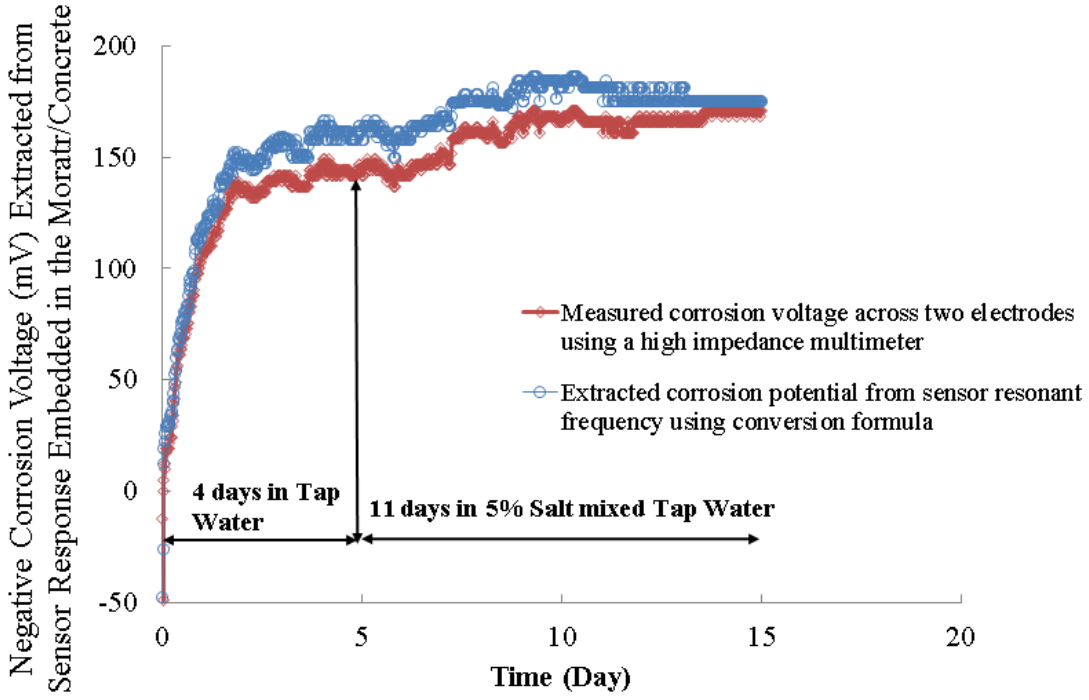

Figure 4. 11: Extracted corrosion potential using equation 4.2 and measured corrosion potential. Note the uncertainty in the measurement is less than 10 mV.

The salt mixed solution was used to simulate the chloride induced corrosion which penetrates through the mortar specimen and eventually reaches to the electrodes initiating the corrosion process. In the 4 days tap water experiment, the potential

increased up to 130 mV and remained constant around 125 mV in direct measurement using a high impedance digital multimeter. Then the specimen was submerged in 5% salt mixed tap water for 11 days and the corrosion potential rose up to 180 mV indicating the initiation of corrosion. The potential difference between the direct measurement and the extracted value using eqn. 4.2 is less than 20mV. The possible reason for the offset difference is the finite resistance of the cell. The cell source resistance, R_{cell} =0.755MΩ was measured at V_{cell}= -130mV.

The possible reasons for this difference is the finite impedance of the cell rather than low impedance which was used to obtain equation 4.2, 5 mV resolution of A/D which was used to log cell potential and the precision of the power supply used for the DC calibration, the parasitics due to mortar around the PCB coil and the linear fit errors from equation 4.2.

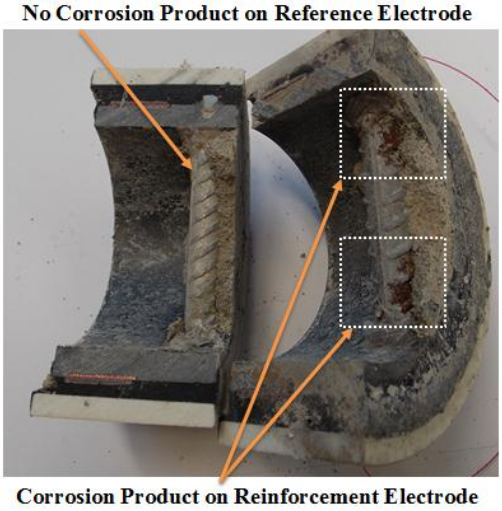

Figure 4. 12: Rust products on the steel reinforcement of the cylindrical shape sensor taken out from the mortar specimen almost 14 months after the accelerated corrosion test ended.

After 14 months of the corrosion test ended, the sensor was taken out from the mortar specimen having some corrosion (rust) product on the surface of the steel reinforcement as shown in fig. 4.12.

4.7 Summary

Finally, chapter 4 demonstrates the fixed capacitor and the varactor modelling of the cylindrical shaped sensor and their test results under different operating conditions. It also presents the sensor performance with the different separation distance between the interrogator and the sensor coil. Moreover, it shows the embedding procedure of the cylindrical shaped sensor in the cement based mortar and an accelerated corrosion test results from the embedded sensor.

Chapter 5: Results of the PCB sensor under different operating conditions

5.1 Introduction

In this chapter the results obtained from tests of the PCB based sensor are described. The sensor response was tested under conditions that simulated embedding in new and existing structures. The simple and one sided design of the sensor on the PCB make it a very cost effective viable option for long-term monitoring of large civil structure. Using PCB technology will allow this sensor to be mass produced and widely deployable for monitoring new as well as existing civil structures. As mentioned in chapter 3, the PCB sensor was enclosed by 2×1.5 mm thick Poly (methyl methacrylate) (PMMA) transparent thermoplastic (brand name as PLEXIGLAS, ε_r= 2.6-3.5) (PMMA, n.d.), (Dielectric Constants, n.d.) causing a deviation of 45-55 kHz. Furthermore, the embedded sensor in the cement based mortar resulted in a 245-425 kHz drop of resonant frequency, due to the parasitics from the mortar around the sensor coil, corresponding to a 175-303.6 mV changing corrosion potential.

This chapter compiles all the experimental results that have been done on the PCB sensor including calibration, choosing the sealing technique and the sensor test results in new and existing civil structures. Sec. 5.8 explains the accelerated corrosion test on the corrosion sensor in different % salt (NaCl) mixed layered structure to simulate the chloride induced corrosion from the top and bottom of the mortar specimen. In sec. 5.7, the corrosion sensor test has been done on new structure (sound concrete) containing corrosion causing substances below the threshold level, which can hardly show a significant level of corrosion. But in sec. 5.8, the sensor performance is characterized in

the civil structure that has been contaminated by the corrosive substances at the time of installation. For this purpose, the sensor was embedded orthogonally in the mortar specimen. At the time of installation a thin layer of salt mixed mortar was cast on top end edge of the electrodes to avoid the instant corrosion. Sec. 5.9 and 5.10 describes the sensor performance in different dielectrics using the sealed sensor, as described in sec.3.3.2.1 - sec.3.3.2.4. Sec. 5.11 shows the sensor performance in simulated field conditions if it is surrounded by other corrosion potential sensors. Moreover, a diffusion test is shown in sec. 5.12. Sec. 5.14 explains the moisture effect on the measured and extracted (from resonant frequency) corrosion potential from the accelerated corrosion test. Sec. 15 demonstrates the accelerated corrosion tests on new and existing civil structures using a new embedment procedure of the sensor in the mortar specimens mixed with different percentage of salt.

5.2 Sensor response Under Different Operating Conditions

5.2.1 Fixed Capacitor Model

In the process of encapsulation of the sensor, several tests have been done on the PCB coil with a 33pF fixed capacitor instead of the sensing circuit representing the varactor (NXP BB202) diode junction capacitance at zero bias. These tests were carried out in a precision impedance analyzer (Agilent 4294A). From fig. 5.1, when the sensor coil is not perturbed by the surroundings, the sensor resonates at a frequency of 5.9323 MHz with the fixed capacitor. The losses are small and the quality factor of the sensor is ~84.51, as determined based on a 3dB point. When salt water is put on the bare coil, the sensor resonant frequency is reduced ~185 kHz from 5.9323 MHz and Q-factor is ~40.

Salt water is used to simulate the lossy dielectric medium of wet concrete. Changes in the surrounding medium lead to the sensor's resonant frequency shift and the addition of loss causing the reduction of Q factor is related to the dielectric conductivity of the medium.

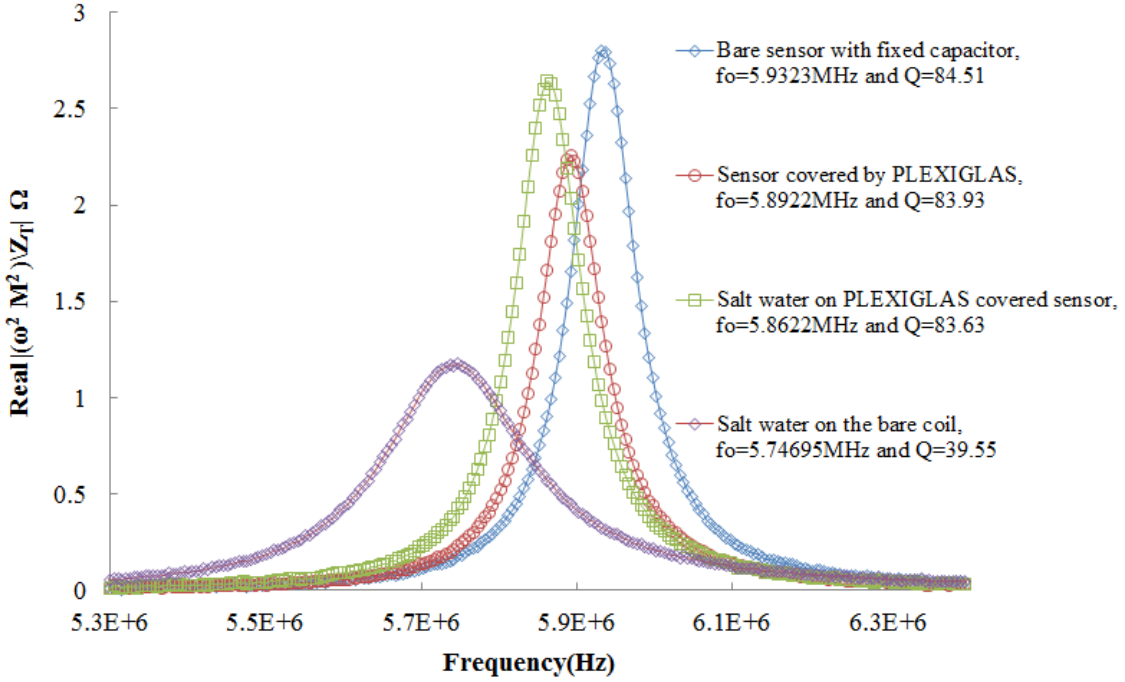

Figure 5. 1: PCB Sensor response with fixed capacitor under different operating condition

Thus, to protect the sensor from the harsh environment of the concrete, THE sensor is sealed by 2x6mm thick PLEXIGLAS cover or cast into a 12mm thick epoxy case. This results in a resonant frequency drop of 35-70 kHz. With the sensor encased the response of salt water is minimized and immersing the sensor in salt water results in a shift of less than 30 kHz. Since the sensor sensitivity is 1.53 kHz /mV or 1.63 kHz/ mV (sensitivity corresponds to Epoxy sealed or PLEXIGLAS with air gape sealed respectively), this results in an error of less than 20 mV.

5.2.2 Varactor Based Model

Fig. 5.2 shows the sensor response with the sensing circuit at zero bias under different operating conditions. The bare sensor resonates at 5.955MHz. Without encapsulation the sensor sitting on a dry concrete block shows the highest frequency drop of 85 kHz resulting from the dielectric change of the medium (Mortar/concrete). Assuming the losses are small, the sensor encapsulated by PLEXIGLAS shows 15 kHz drop of resonant frequency and the Q of the sensor response is calculated same as fixed capacitor sensor. The embedded sensor response at zero bias inside the concrete in the presence of moisture, water and chlorides is simulated using salt and regular water causing a frequency drop of 30-70 kHz.

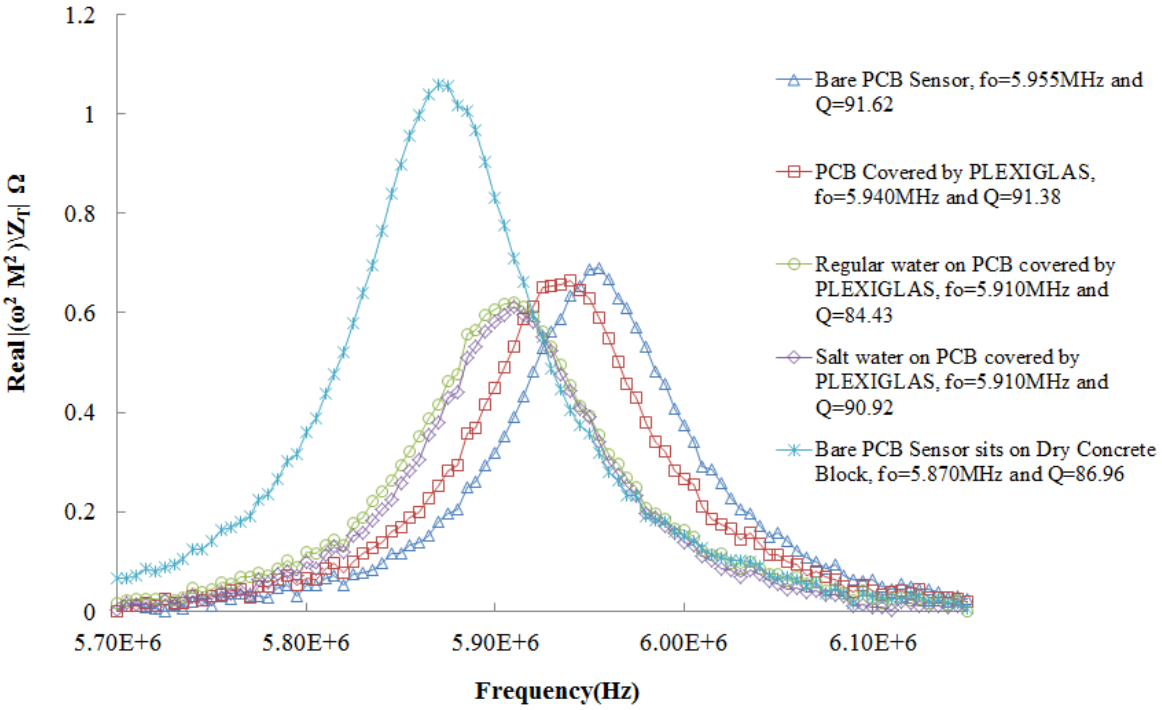

Figure 5. 2: PCB Sensor response with sensing circuit under different operating conditions

5.3 Sensor performance with different separation distance

The sensor response was measured using the Impedance analyzer to determine the sensor performance with different distances. For fabrication simplicity, most of our tests were carried out on the PCB sensor. For signal to noise ratio (SNR) calculation the bandwidth of the system was set to 66.9 kHz and frequency was swept from 5.8 MHz to 6.0 MHz, with 800 evenly distributed measurement points with no averaging, as shown in table 5.1. Fig.5.3 and fig. 5.4 show the measured spectrum in the impedance analyzer at different interrogation distances. With this method the maximum interrogation distance where a measurable peak was obtainable was 15cm which provides a 17.6 dB SNR at resonance. The resonance peak from the sensor response was obtained using a curve fitting algorithm as shown in appendix A (Robinson & Clegg, 2005), (Bhadra, Bridges, & Thomson, 2010). The curve fitting algorithm gives a resonant frequency deviation of ± 1.15 kHz (using standard deviation) from 5.913 MHz among 6 set of data points as shown in table 5.1

Table 5. 1: Resonant frequency and SNR for different distances for impedance Measurement (Concentrically coupled sensor)

Separation Distance(d=cm)	Resonant Frequency(MHz)	SNR(dB)
6	5.913	59
7	5.914	53
9	5.912	39
11	5.914	30
12	5.914	27
15	5.911	18

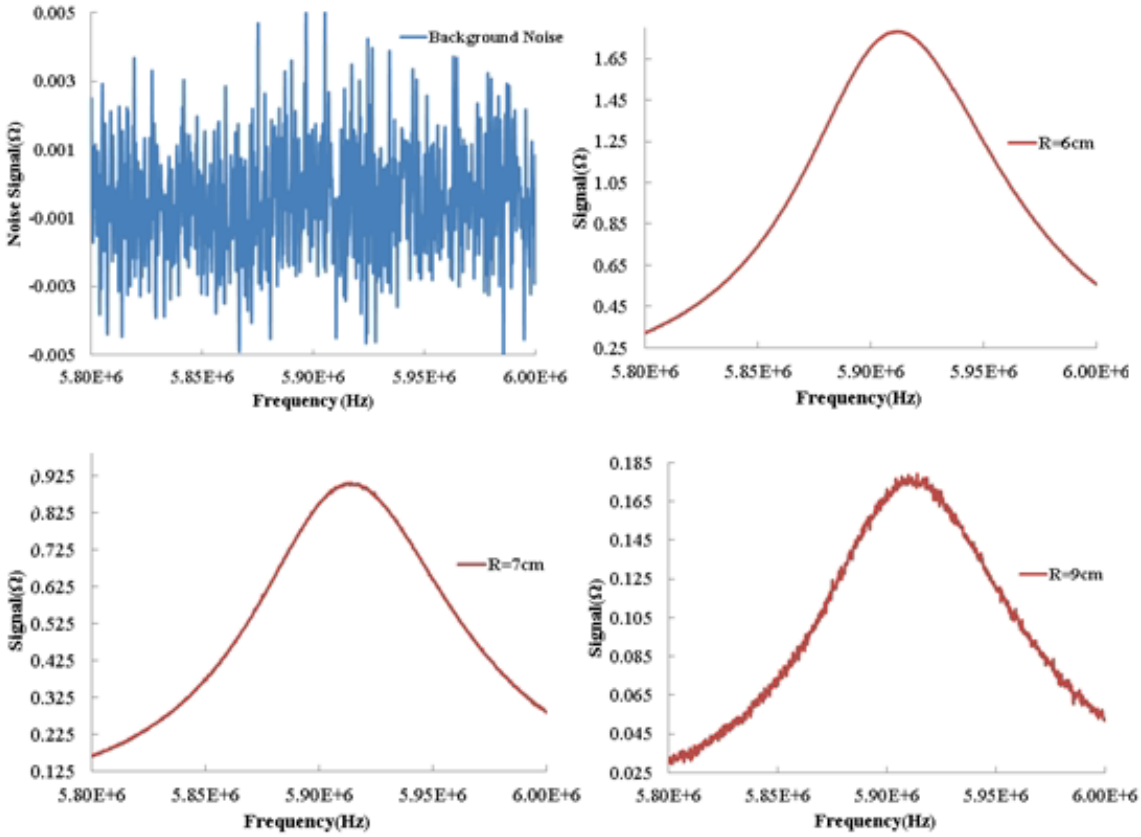

Figure 5. 3: Real part of the impedance measurement in Impedance Analyzer

For measuring the sensor performance with different interrogation distances, the source voltage was set to 150 mV for 9 to 15 cm and 50 mV for 6 to 7 cm to avoid nonlinearity. For further designs, the separation distance could be increased by increasing the source voltage and the number of turns of the PCB coil (Sharmistha Bhadra and Douglas J Thomson and Greg, E. Bridges, 2013).

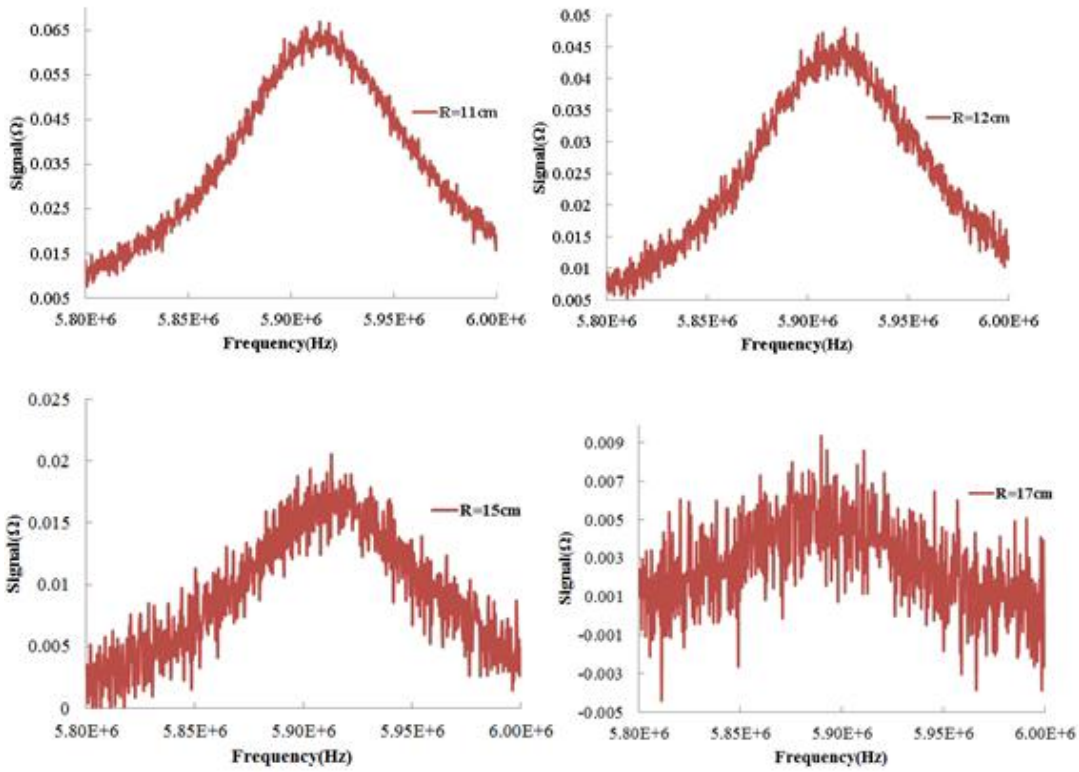

Figure 5. 4: Real part of the Impedance Measurement in Impedance Analyzer continued

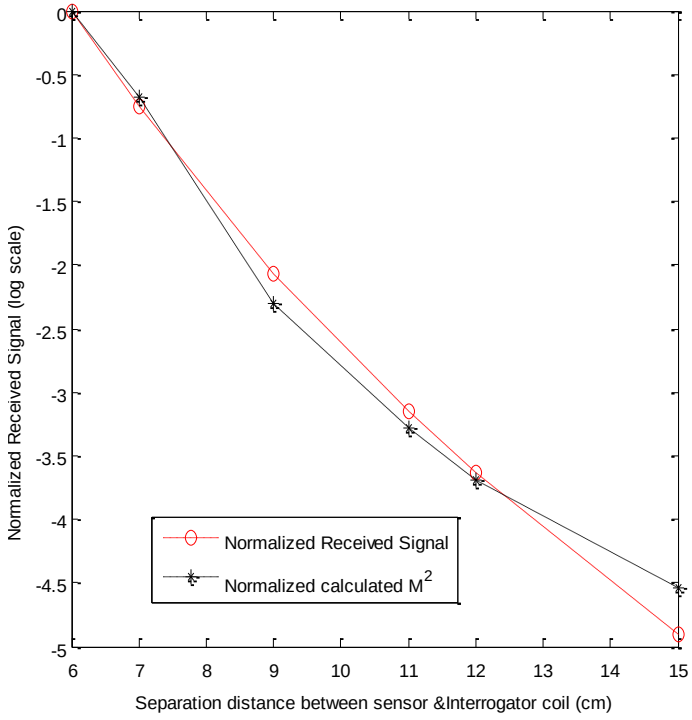

Figure 5. 5: Normalized received signal and M2 for the sensor with distance

The mutual inductance, M between the sensor and the interrogator coil was calculated for different distances using eqn. 2.11 The normalized signal for a fixed exciting frequency *f=5.914* MHz is plotted in fig. 5.5 with the normalized M^2 value for different distances. From fig. 5.5, the normalized received signal is in good agreement with the normalized M^2, showing that the path loss follows the theory in section 2.3.2 (Bhadra, 2010).

5.4 DC Calibration on PCB Sensor

Initially a DC voltage was applied to the sensing circuit using a controlled DC voltage source to simulate the corrosion potential (Bhadra, 2010), (Perveen, Bridges, Bhadra, & Thomson, 2013). The sensor coil was concentrically aligned with the interrogator coil (5cm diameter) with separation distance, d=7cm and the source amplitude, V_G was set to 15mV to avoid the nonlinearity of the sensor response. The PCB (L_s=20.33μH, Rs=12.76Ω, Cp=1.84pF, n_s= 28 turns, $f_{self\text{-}resonant}$= 28.069MHz) sensor resonant frequencies as a function of applied negative voltage to the sensing circuit are shown in fig. 5.6. The negative voltage applied to the sensing circuit was varied 0 mV to 900 mV and the measured resonant frequency is a linear fit shown in fig. 5.6. The slope, 0.1617 MHz/100 mV is obtained from a fit to the curve. From the linear curve fit, eqn. 5.1 of PCB sensor relationship of voltage applied to the sensing circuit, *V* to the resonant frequency of the sensor, f_0 can be estimated.

$$V(mV) = 595.2 f_0(MHz) - 3529.8 \quad (5.1)$$

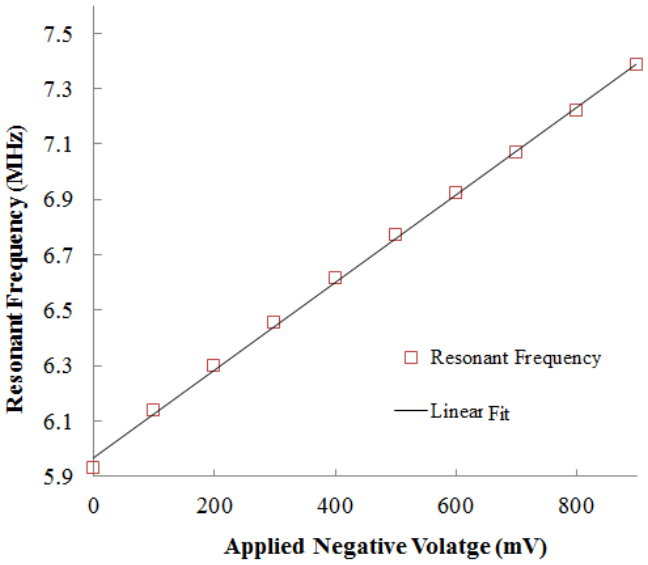

Figure 5. 6: Resonant Frequency vs. Applied negative voltage to the sensing Circuit of PCB Sensor in air [without encapsulation]

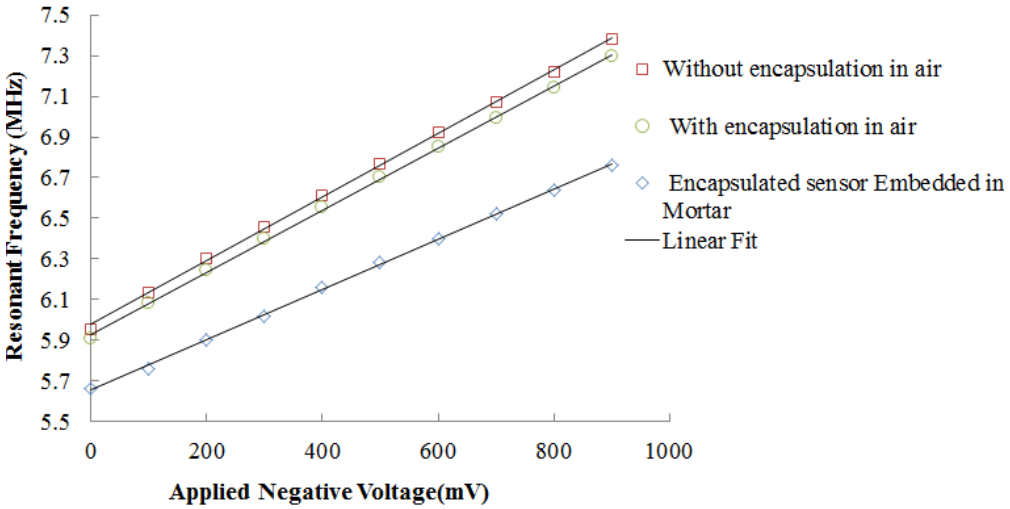

Figure 5. 7: Resonant Frequency vs. Applied negative voltage to the sensing Circuit of PCB Sensor under different condition [2×1.5 mm PLEXIGLAS sealed sensor]. See fig. 3.17(c) or 5.14 for details.

Fig. 5.7 shows the resonant frequencies of the PCB sensor as a function of applied negative voltage is influenced by surrounding dielectric changes. However, using eqn. 5.1 the encapsulated sensor gives an error of 0.9% in the conversion of the resonant

frequencies. On the contrary, the embedded sensor in the mortar gives a significant 4.95% conversion error arising from the parasitics due to mortar around the sensor coil and the large source impedance.

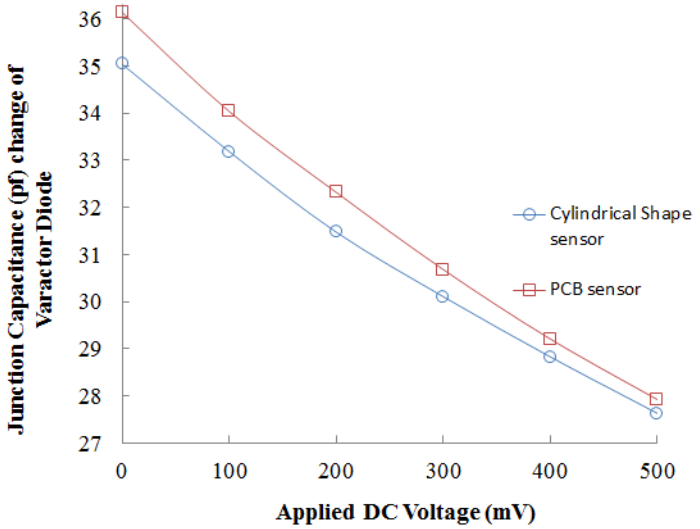

Figure 5. 8: Resonant Frequency vs. Applied negative voltage to the sensing Circuit of PCB Sensor under different condition

Therefore, the eqn. 5.1 is not valid for the sensor embedded in the mortar. So, from the linear curve fit eqn. 5.2 of the PCB sensor embedded in mortar is obtained,

$$V(mV) = 806.5 f_0(MHz) - 4564.5 \qquad (5.2)$$

The slope of the linear curve is 0.124 MHz/100 mV for the embedded PCB sensor. Fig. 5.8 shows the comparison of junction capacitance change of varactor diode as a function of applied negative voltage to the sensing circuit for both cylindrical and PCB sensor. The average variations of junction capacitance, 0.67pF between cylindrical and PCB sensor comes from the parasitic capacitance of the closely spaced inductor loop of the two sensors coil.

5.5 Comparison of results from Different System Measurements

In this work two different approaches were used to determine the resonant frequency. One was a frequency domain measurement with a precision impedance analyzer (Agilent 4294A). The second was a time domain based system. In this section the measurement approaches are compared. For this purposes a DC calibration was done on 2×1.5 mm PLEXIGLAS sealed PCB sensor using a precision power supply (HP 6115A) having less than 5mV resolution. The sensor response was measured both in Precision impedance analyzer (Agilent 4294A) and Time domain gating interrogation system (TDGS). The PCB sensor (L_s=20.33μH, Rs=12.76Ω, Cp=1.84pF, n_s= 28 turns, $f_{self\text{-}resonant}$ = 28.069MHz) coil was concentrically coupled with 5cm diameter interrogator with separation distance, d= 7cm. Fig. 5.9 shows the PCB sensor response as a function of applied negative voltage to the sensing circuit measured by the TDGS and Impedance Analyzer (Agilent 4294A).

A linear fit from the impedance analyzer measurement, as shown in fig. 5.9 is given by

$$f_0(MHz) = -0.00156 \times V(mv) + 5.8801 \qquad (5.\ 2)$$

From fig 5.9, a slope of 1.56 kHz / mV (corresponds to a slope of 0.641 mV /kHz) is determined from impedance analyzer measurement over a potential range of 0 to -400 mV. Using eqn. 5.2, TDGS value gives the maximum deviation of 0.72% from impedance analyzer value having a slope of 1.578 kHz / mV (a very negligible deviation of less than 4.6 mV over 0 to 400 mV range).

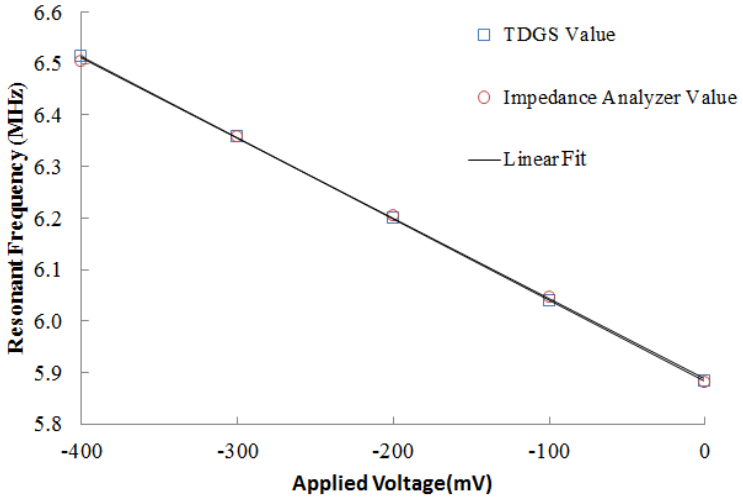

Figure 5. 9; Comparison of PCB sensor response in different measurement system

The results in fig. 5.9 demonstrate that both measurement approaches are very similar with a measured deviation less than 5 mV over a 0 to -400 mV range.

5.6 Off Axis coupled Sensor performance with different separation distance

In order to easy transportation of reactants from surrounding media to the electrodes, the sensor was installed in the mortar specimen vertically with respect to the interrogator coil. Table 5.2 explains the off axis coupled sensor performance in Impedance analyzer with different separation distance. A curve fitting algorithm was used to obtain the resonance peak (Bhadra, S., 2010).The off axis coupled sensor resonant frequency has a deviation of ~7.9-8.4 kHz corresponding to a ~5.2-5.5 mV from the concentrically coupled sensor.

Table 5. 2: Resonant frequency and SNR for different distances for impedance Measurement (Off Axis Coupled Sensor)

Separation Distance (d=cm)	Resonant Frequency(MHz)	SNR(dB)
3	5.9212	61
5.5	5.9207	42
6	5.9212	38
8	5.9214	26
9	5.9212	0.16

An off axis embedded sensor coupled with interrogator coil is shown in fig. 5.10.

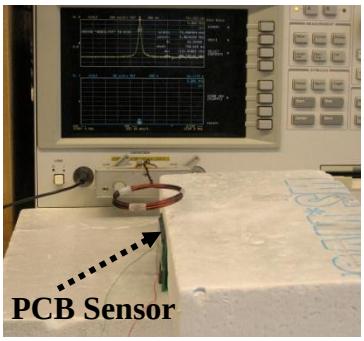

Figure 5. 10: An off axis Coupled Sensor with Interrogator coil

The two coils coupled off-axis limits the energy transfer by magnetic induction. The mutual coupling is the fraction of the flux of the interrogator coil that cuts the secondary coil, and is a function of the geometry of the system ("Resonant inductive coupling", n.d.). Hence, the separation distance, as shown in table 5.2, between the sensor and the interrogator coil is reduced compared to concentrically coupled sensor, as shown in table 5.1, with increasing separation distance. For the off-axis coupled sensor, less energy is coupled with the sensor coil which limits the interrogation distance of the sensor.

5.7 Accelerated Corrosion Test on PCB Sensor

5.7.1 Making of Mortar Specimen

The procedure for making a square shaped mortar specimen was same as the cylindrical specimen. The specimen was made from 2.463 kg of mortar (Quickrete mason mix-type S mortar, no. 1136), thoroughly mixed with 463gm of water. In our early accelerated corrosion test, the sealed sensor using 1.5 mm thick PLEXIGLAS which is shown in fig. 3.17 (a) was embedded in the mortar specimen. Only the PCB top coil was sealed by PLEXIGLAS and the sensing circuit was sealed by non-conductive epoxy left the PCB back side exposed in the mortar specimen. It was kept 7 days in the plastic mold shown in fig. 5.11; afterwards it was taken out and cured for 23 days in the air. The specimen was 7 cm in height and 13 cm in length. The electrodes were separated 5.7 cm from each other.

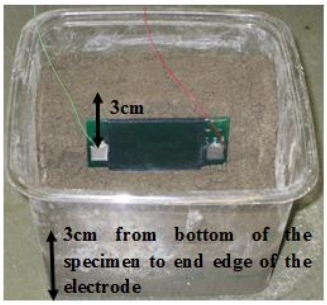

Figure 5. 11: PCB sensor (Top) sealed by 1.5mm thick Plexi glass embedded in Mortar

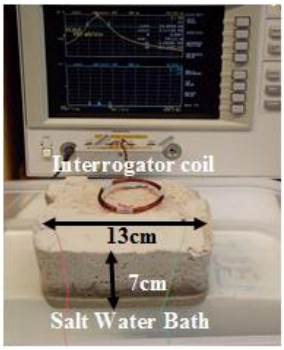

Figure 5. 12: A prototype test set up in Impedance Analyzer

The electrodes were grade-1018 mild steel for the reinforcement electrode and grade-316 stainless steel for the reference electrode. The sensor was embedded in the middle and the electrode distance from the bottom and top of the specimen were both 3cm. After air curing, the specimen was submerged in tap water and rest of the procedure as same as the cylindrical shape sensor experiment. Fig. 5.12 shows an experiment set up in Impedance Analyzer (Agilent 4294A) for PCB sensor in salt bath.

5.7.2 Results

In this experiment, the potential across the electrodes went up to 65 mV and then remained stable in plain water over the 4 days of the measurement, which is shown in fig. 5.13.

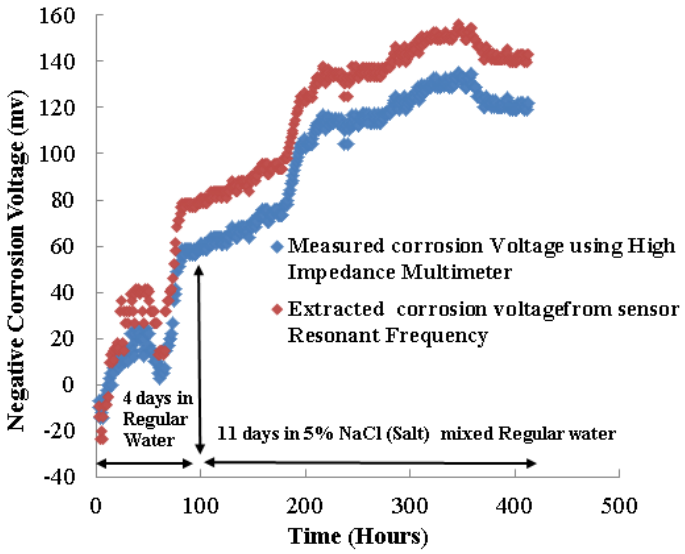

Figure 5. 13: Extracted corrosion potential using equation 5.2 and measured corrosion potential using an A/D (Perveen, Bridges, Bhadra, & Thomson, 2013)

In 5% salt mixed water, the potential further started to increase and it went up to 135 mv over the 11 days of the measurement. It indicates that the chloride front has reached the reinforcing bars and the corrosion process is in progress. The difference of

potential between measured and extracted value is less than 30mV. The cell source resistance, R_{cell} = 0.837MΩ was measured at $V_{cel\ l}$ = -*1*69.2mV.

The measured potential for both cylindrical and PCB sensors were not identical. The generated potential is a measure of the transfer of electron charge between the metal and its environment, here between the steel and the cement pore solution. This is a property of the steel/concrete interface and not of the metal itself. Thus, it is impossible to determine the absolute value of this electrochemical potential and it is necessary to have a reference electrode to measure the potential difference of the steel with respect to this reference electrode (Hope et al., 2001). The possible reasons for this offset difference is the finite impedance of the cell, rather than low impedance which was used to obtain equation 5.2, base line shift of the sensor in different dielectric medium and the 5 mV resolution of A/D, which was used to measure the cell potential (Bhadra, Bridges, & Thomson, 2010), (Perveen, Bridges, Bhadra, & Thomson, 2013).

5.8 Accelerated Corrosion Test on PCB sensor in layered Structure

5.8.1 Making of the mortar specimen

In sec. 5.7, the accelerated corrosion test was done on the new structure containing no chlorides at the time of installation of the sensor. But in this section the sensor has been installed on the mortar specimen that contains a thin layer of salt mixed mortar, < 1.5 cm, from top level of the electrodes to the top level of the orthogonally installed PCB sensor shown in fig.5.14.

Table 5.3 compiles the ingredients that were used to make 0%, 1%, 3% and 5% mortar specimen and the sensor was installed at the time of making the mortar specimen.

Table 5. 3: Composition of ingredients for making mortar specimens

No. of % salt Mixed Block	Mortar weight (gm)	Water (gm)	Salt (NaCl), gm	Water/Mortar Ratio	Curing Time (day)
0	2202	342	NIL	~ 0.155	52
1	2154	334	3.34	~ 0.155	56
3	1956	303	9.09	~ 0.155	55
5	2029	314	15.7	~ 0.153	73

First the mortar was thoroughly mixed with water containing no mixed chlorides (Salt) and casted in the mold having the diameter same as mentioned in chapter 4, however, the mortar specimen height was 6 cm. Afterward the sensor was pushed 2cm through the middle of the mortar vertically as shown in fig. 5.15. At the time of installation careful handling was necessary to avoid any kind of corrosion causing substances may arise from the salt mixed layer, for this purpose two electrodes should be fully embedded in the fresh mortar.

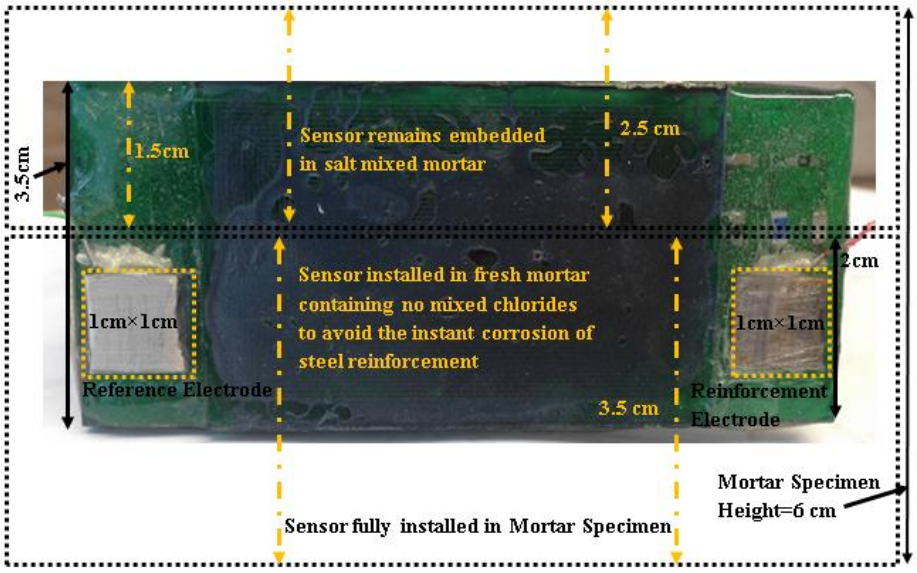

Figure 5. 14: A diagram of the orthogonally installed sensor in the layered mortar specimen

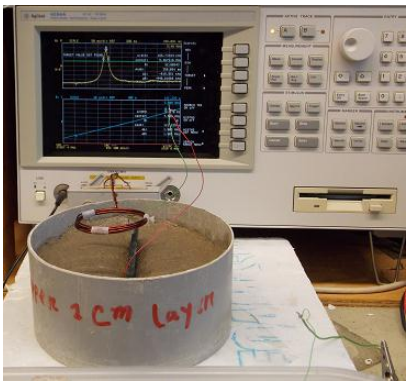

Figure 5. 15: Installed sensor in the fresh mortar and the exposed portion will be covered by salt mixed layer

After installing half of the PCB sensor in the fresh mortar, it was left 30 minutes for curing. Then, the salt mixed layer was casted from the top of the PCB sensor that was come out from the fresh mortar. After that, different %salt mixed mortar blocks were left 7 days in the mold then the mortar blocks were taken out from the mold and left for air curing. Fig. 5.16 shows the cured embedded sensor in different %salt mixed mortar specimens. However, the time duration for curing of each block was not same as shown in table 5.3, which had an effect on the results of accelerated corrosion test of those mortar specimens. The curing time shown in table 5.3 includes the curing time in the mold as well as the time of air curing in the lab.

Figure 5. 16: Different % salt mixed mortar block

5.8.2 DC Calibration

An applied controlled DC voltage using a precision power supply (HP 6115A having a resolution less than 5mV) test was done on each embedded sensor for calibration purposes. The source voltage was varied from 0 mV to 500 mV. Fig. 5.17 shows the DC calibration on embedded sensor which is a linear fit. The sensor used for this accelerated corrosion test was sealed by 2×1.5 mm thick PLEXIGLAS except for 1% salt mixed block which was sealed by 2×6mm Thick PLEXIGLAS (each side and sensing circuit of the PC board was sealed by non-conductive epoxy). Though the sealing technique was similar as described in sec. 3.3.2.1, the electrodes size was 1cm×1cm. The behavior of the 1% salt mixed block was similar as for the epoxy sealed sensor, as demonstrated in sec. 5.15.2. The DC calibration for no salt, 3% and 5% salt mixed specimen were close to each other. Thus, a frequency conversion formula can be derived from one of these three specimens, and using a correction factor the corrosion potential can be extracted from collected data for other sensors, as shown on table 5.4. From the linear curve fit of 3% salt mixed block, eqn. 5.4 of embedded PCB sensor in the mortar specimen was obtained which relates the negative voltage applied across the two electrodes, V to the resonant frequency of the sensor, f_0.

$$\mathrm{V(mV)} = 769.2 \times \mathrm{f_0(MHz)} - 4230.8 \qquad (5.3)$$

The sensor performance was affected by dielectric permittivity changes in the medium that caused a base line shift of the sensor. This base line shift has been reduced a large scale and is described in sec. 5.10. Furthermore, the fringing field effects triggered from the dielectric permittivity changes in the medium is described in sec. 5.9.

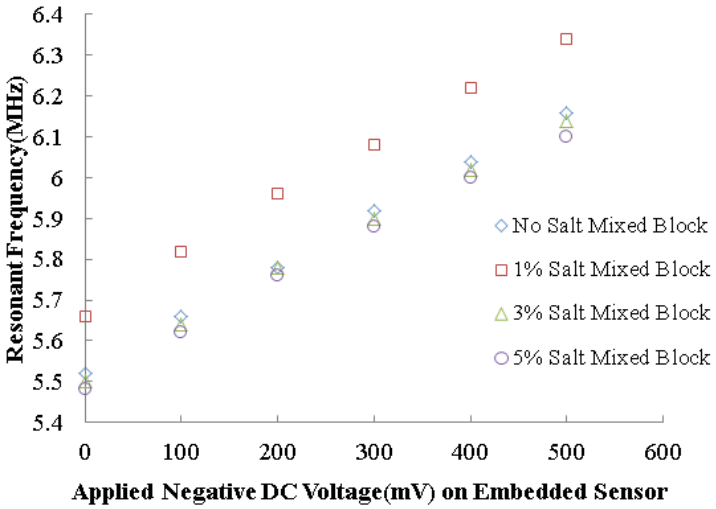

Figure 5. 17: DC Calibration Results of Embedded Sensor (2×1.5 mm thick PLEXIGLAS Sealed Sensor for No Salt, 2% and 3% salt mixed block and 2×6 mm thick PLEXIGLAS Sealed Sensor for 1% salt mixed block). See details in fig. 3.17(c) for No salt, 2%, 3% and fig. 3.18(g) for 1% salt mixed block

Table 5. 4: PCB Sensor Response under Different Operating Conditions

Sensor no. (no. refers to % Salt)	Frequency in air (MHz)	Frequency (MHz) of sealed sensor	Frequency (MHz)after fully Installed	Capacitance Change (ΔC), pF, after fully Installed	Equivalent Voltage (mv), ΔV, after fully Installed	Q-factor(f0/Δf) After installation
PLEXIGLAS (2×1.5 mm thick) Sealed Sensor [Sensitivity of the sealed sensor = ~1.6 kHz/mV]						
0	5.960	5.905	5.550	4.72	221.9	
1	5.960	5.875	5.684	2.47	119.4	
3	5.960	5.905	5.270	9.13	396.9	~20-30
5	5.960	5.905	5.305	8.54	375.0	

5.8.3 Results

Fig. 5.18 demonstrates the results from the 1% salt mixed mortar specimen. The sensor resonant frequency and the corrosion potential generated from two electrodes, V_{cell}, were monitored continuously using an external interrogator coil and a high

impedance multimeter respectively. The corrosion potential from sensor resonant frequency was obtained from eqn.5.4 using a correction factor described in table. 5.6.

During first 5 days in fig. 5.18, 1% salt mixed mortar specimen was submerged in tap water and 18 days were submerged in a 5% salt solution. In tap water, the sudden rise of corrosion potential went up to 217 mV, and then gradually decreased following this trend in 5% salt solution as well. In the 23 days experiment, the potential decreased gradually and became slightly stable at 122 mV. The corrosion potential from sensor resonant frequency followed the pattern of the directly measured potential having a less than 30 mV difference from the directly measured potential. However, the reasons for this offset difference have been explained in sec. 5.7.2 and 5.15.3.

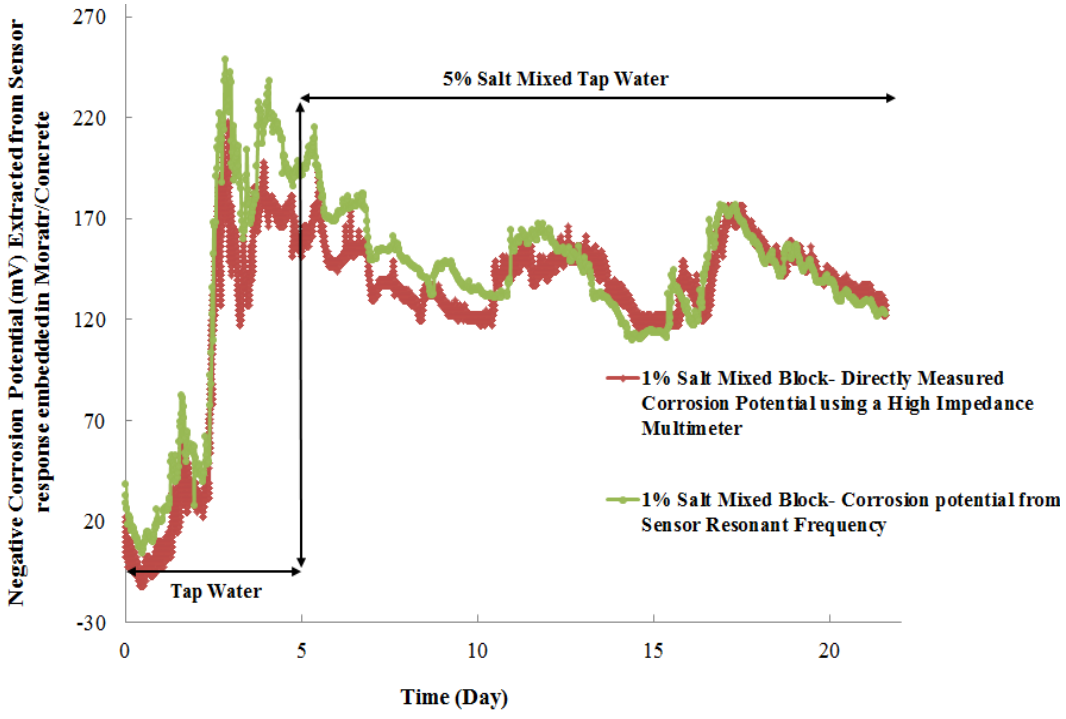

Figure 5. 18: Extracted corrosion potential from sensor resonant frequency using equation 5.4 and measured corrosion potential. Note the uncertainty in the measurement is less than 10 mV.

Fig. 5.19 shows the chloride effects on the corrosion process of steel reinforcement. For 5% and 1% salt mixed block, accelerated corrosion test was carried out for 22 days and for other two blocks the test duration was 15 days. The potential rise for salt mixed mortar was relatively higher than no salt mixed block.

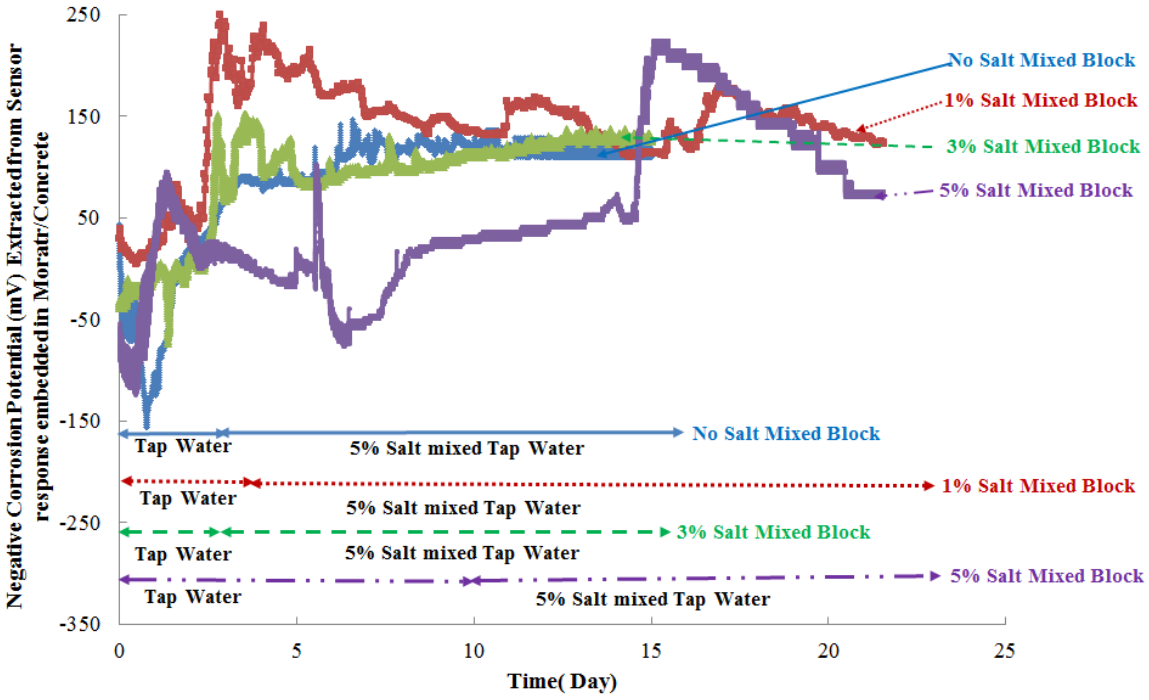

Figure 5. 19: Chloride effects on the corrosion potential of steel reinforcement in civil structure made with no salt, 1%, 3% and 5% salt mixed (by weight of mixing water) layered mortar specimen. The PLEXIGLAS sealed sensor (details are mentioned in fig. 5.17) was embedded orthogonally in the middle of the mortar specimen. See details in fig. 5.14 and fig. 5.15.

However, the potential for a 1% salt mixed block was relatively higher than for the other three blocks over the first 14 days. The potential for the 5 % salt mixed block suddenly increased after 15 days submerged in tap water and 5% salt mixed solution, afterwards it gradually reduced for the rest of the test duration, and became stable at ~60 mV. Furthermore, the 5% salt mixed block had the longest curing time of 73 days, as

shown in table 5.3. During this time the electrodes may have become corroded which may lower the potential difference. Therefore, after a certain time the reference electrode start to corrode and eventually the potential difference between steel reinforcement and reference rebar becomes smaller. The potential level for these salt mixed layered mortar blocks was lower than described salt mixed mortar block in sec. 5.15.3.

As mentioned in sec. 5.15, the mixed chlorides with the mortar/concrete mixing water have an effect on the corrosion process of steel reinforcement (Pakshir & Esmaili, 1998). The mortar specimens were made with a thin layer of salt mixed mortar, however, the sensor was also installed almost at the same time with a 30 minutes gap. To avoid the instant corrosion of the two electrodes, the salt mixed mortar was overlaid on the fresh mortar with a 30 minutes gap but the mixed chlorides may leech through the wet mortar/concrete. The Quickrete mortar takes almost 1 to 4 days to be cured depending on the curing conditions. Therefore, the mixed chlorides eventually reach to the electrodes and initiates corrosion with presence of moisture and O_2. Also these differences may come from the presence of corrosion substances on the surface of the steel reinforcement arising during handling and installation. This simulation of the sensor in the salt mixed layered structure facilitates the understanding of the sensor behavior embedded in the new civil structure and contaminated by corrosion causing substances at the time of installations. However, it is hard to conclude a lot from the scattered behavior of the corrosion potential extracted from the sensor response. Because of the curing time of each block, the test duration in tap water and for the 5% salt solution for each block was not same. Also, each block was cured in the lab environment and the accelerated test was not carried out in 100% relative humidity, so the humidity may change anytime which

has an effect on the corrosion process of the steel reinforcement. Fig. 5.20 shows the sensors embedded in mortar specimen, were taken out from the mortar specimen almost 9-10 months after the accelerated corrosion tests ended. From fig.5.20, it can be seen that the reinforcement steel is rusted with corrosion products.

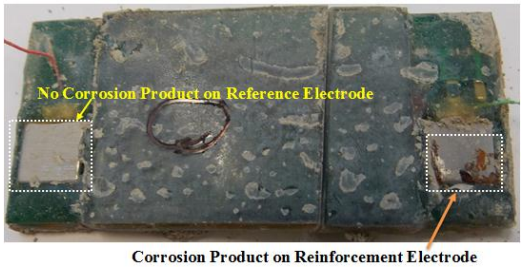

(a) No salt mixed block

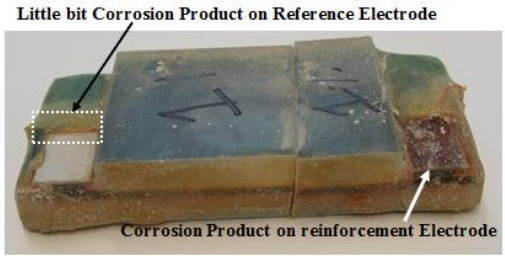

(b) 1% salt mixed block

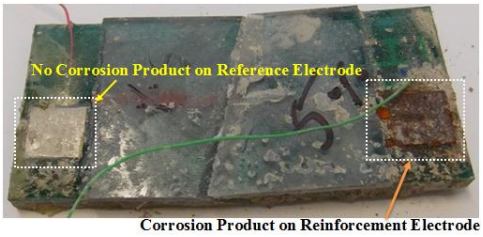

(c) 5% salt mixed block

Figure 5. 20:The sensors embedded in no salt mixed, 1% and 5% salt mixed mortar specimen were taken out from the mortar specimen almost 9-10months after the accelerated corrosion tests ended. The sensor from 5% salt mixed has the largest corrosion (rust) product than the sensors from 1% and no salt mixed mortar specimen.

5.9 Sensor performance in DI and Salt water [Using 1.5 mm thick PLEXIGLAS encapsulation]

The described result in sec. 5.4 shows that the sensor response has been shifted in every step since encapsulation to embedment inside the mortar. The sensor performance was affected by the dielectric response of whole system (Heidari & Azimi, 2011), (Ong et al., 2008). In the sensing circuit, the used BB 202 NXP varactor diode as the main sensing element has a junction capacitance of~22-34.5pF for an applied voltage of 0-1V respectively.

Table 5. 5: Sensor response under different test condition [see the encapsulation procedure in fig. 3.17] (Heidari & Azimi, 2011)

Sensor in different medium	Frequency(MHz)	Capacitance(pF)	Q-factor
Air (Bare Sensor)	5.955	35.12	92
Encapsulated by 2×1.5 mm thick PLEXIGLAS using Nail polish, Non -conductive Epoxy, Conductive Silver Epoxy	5.905	35.73	78
Encapsulated Sensor in DI water	5.554	40.40	60
Encapsulated Sensor in 3% Salt mixed Tap water	5.058	48.70	39
Encapsulated Sensor Embedded in mortar (Cured)	5.660	38.90	20

Table 5.5 explains the capacitance variations of the sensor when it comes to an interaction with the different medium of dielectric (Heidari & Azimi, 2011), (Ong et al., 2008). From table 5.5, the materials providing a hermetic enclosure to the sensor for protection inside the harsh environment of the civil structure drop the sensor resonant frequency 40 kHz adding extra capacitance of 0.5975 pF. The PLEXIGLAS sealed sensor

(fig. 3.17(c)) performance was measured in DI and Salt water. The sensor response was affected by DI water with a dielectric constant of 80 imposing a change of ~ 350-355 kHz resonant frequency from 5.905 MHz and ~4.662-5.2pF capacitance from 35.135pF. Theoretically, the sensor embedded in the mortar (cured) having a dielectric constant of ~ 8-10 (0.1-0.125 of DI water) gives ~ 0.466-0.52 pF/ ~0.583-0.65pF fringing capacitance variations. However, from table 5.5, the embedded sensor in the mortar specimen shows fringing capacitance, Cp= 3.1605pF. These offset differences may come from the electrode polarization and the bulk dielectric response of the cement based mortar (a constant bulk capacitance) (Berg, Niklasson, Brantervik, Hedberg, & Nilsson, 1992).

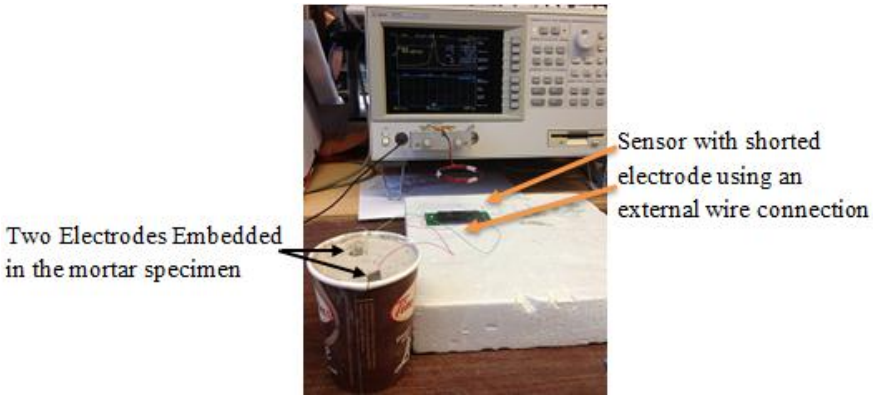

Figure 5. 21: A prototype test set up where sensor was kept outside mortar specimen and two electrodes embedded in the mortar specimen

To find out the contribution of electrodes in the mortar for fringing capacitance calculation, a different test has been done on the PCB sensor having electrode shorted. For this test PCB was kept in the air and two electrodes of size 1cm×7cm embedded in the mortar with a separation distance, d=3cm gave ~3.5 kHz variations from both sensor and electrodes(shorted) in the air.

The electrodes embedded in the mortar contribute 0.035pFin the total capacitance of 3.1605pF. A prototype test set up is shown in fig 5.21. An equivalent impedance model of the sensor embedded in the mortar specimen is shown in fig. 5.22 where C_1 is due to electrode polarization, C_3 arises from fringing field and other circuit components of the PCB , parallel C_2 and R_2 describe the bulk dielectric response of the cement based mortar (Berg, Niklasson, Brantervik, Hedberg, & Nilsson, 1992).

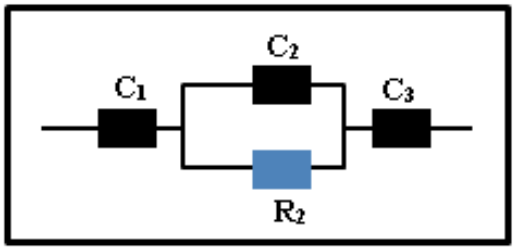

Figure 5. 22: An equivalent Impedance Model of embedded sensor

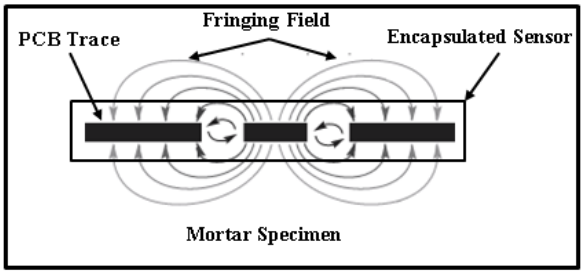

Figure 5. 23: Capacitance arising from fringing field

The inverse of R_2 is due to ionic conduction (DC conductance) in the bulk of the pores, while C_2 gives a dispersive contribution (conduction at the pore surfaces) to the bulk dielectric response. From table 5.5 when sensor was submerged in 5% salt mixed tap water resonant frequency drops leading to a raise of fringing capacitance of 12.97 pF.

From table 5.5 the Q factor was obtained from the resonance peak of the sensor and the width of the resonance referred as eqn. 5.5.

$$Q = \frac{\omega_0}{\Delta\omega} = \frac{f_0}{(f_2 - f_1)} \quad (5.4)$$

According to table 5.5, the Q factor of the sensor submerged in DI water larger than salt water and the sensor embedded in mortar, indicating the change of effective conductivity of the medium. The ionic conduction of both 3% salt solution and salt mixed mortar specimen is much greater than DI water emerging a large loss tangent, which increases the resonance width of the sensor and results a drop of Q factor. When an external electric field is applied across an object, the medium conductivity, σ_s, can be expressed in terms of the electric mobility of the medium, μ_e, and electron charge, q as (Balanis, A., 2012)

$$\sigma_s = -q\mu_e \quad (5.5)$$

The relative permittivity, ε_r, of the medium is generally a complex quantity and the imaginary part of the permittivity changes as a function of material and frequency. The larger the imaginary part, the more energy being dissipated through motion of the charges. Thus, the imaginary part of the relative permittivity directly relates to loss of the system (Balanis, A., 2012). So, the absolute permittivity of a system can be expressed as eqn. 5.7.

$$\varepsilon = \varepsilon_0\varepsilon_r = \varepsilon' - j\varepsilon'' \quad (5.6)$$

Therefore, an effective conductivity of a medium using Maxwell's equation which is not shown here, can be found in terms of medium static conductivity, σ_s, and the conductivity, σ_a, due to an alternating electric field (Balanis, A., 2012)..

$$\sigma_e = \sigma_s + j\varepsilon'' = \sigma_s + \sigma_a \quad (5.7)$$

Then, the loss tangent is defined as,

$$tan\delta_e = \frac{\sigma_e}{\omega\varepsilon'}$$

Therefore, the sealed sensor test in DI and salt water concludes that the 1.5mm thick PLEXIGLAS was not adequate for enclosing of the sensor to protect from the harsh environment inside the mort/concrete.

5.10 Epoxy sealed and PLEXIGLAS (6mm) sealed Sensor performance in DI water [Using 6mm thick PLEXIGLAS /Epoxy Encapsulation]

The previous encapsulation method was not adequate to protect the sensor performance in changing dielectrics, and add a large base line shift of the sensor, as shown in table 5.4. Therefore, other encapsulation techniques were tested. In chapter 3, (sec. 3.3.2.2- sec.3.3.2.4) the details of the fabrication techniques can be found. Table 5.6 demonstrates the sensor performance using the mentioned encapsulation technique in different dielectrics, Q factor and the capacitance change. The tests results mentioned in the table 5.6, demonstrates that the three techniques were capable of dramatically reducing the effects due to environmental coupling, as described in table 5.12. From table 5.6, the PLEXIGLAS with air gap sealed sensor has the most optimum performance based on the achieved Q factor and a minimum baseline shift of ~18-25 mV as described in table 5.12.

In table 5.6, only the resonant frequency for fully installed PLEXIGLAS (2×1.5mm) sealed sensor inside the mortar are shown instead of tap water. These results show that the changing dielectric constant arising from mixed different % salt changes the voltage correction factor in a large scale concluding the encapsulation of the sensor using 1.5mm thick PLEXIGLAS was not sufficient.

Table 5. 6: Test results of Epoxy and PLEXIGLAS sealed sensor in different dielectric medium

Sensor Description	Sealed Sensors & Resonant Freq. (MHz) [No. refers to %Salt] in Air		Sealed Sensor in Different Medium	Resonant Frequency (MHz)	Voltage equivalent correction factor(mV)	Q-factor
Epoxy sealed (6mm) sensor. See details in fig.**3.20(b)**	0	5.840	Air	5.840 [Average]	NIL	80
	1	5.840	Tap water	5.675	108	34
	2	5.840				
	3	5.830	Mortar	5.702	90	57
PLEXIGLAS **(6mm)** sealed sensor. See details in fig.**3.18(g)**	5.860		Air	5.860 [Average]	NIL	72
			Tap water	5.700	105	40
			Mortar	5.778	54	61
PLEXIGLAS **(air gap)** sealed sensor. See fig.**3.19(c)**	1	5.955	Air	5.950	NIL	85
	2	5.950	Tap water	5.905	28	76
	3	5.950	Mortar	5.915	22	75
PLEXIGLAS **(1.5mm)** sealed sensor. See fig.**3.17(c)**	0	5.905	Mortar	5.550	222	29
	3	5.905	Mortar	5.270	397	25
	5	5.905	Mortar	5.305	375	21

5.11 Sensor performance surrounded by other sensors

In practice, a large volume of sensors will be embedded in a reinforced civil structure to monitor the corrosion behavior of the steel reinforcement and possibly surrounded by iron rebar and wire mesh. As the time domain interrogation has a superior advantage over impedance measurement technique, the sensor response is not affected by any surrounding objects. PCB technology made this sensor inexpensive and available for mass production. In reality, the sensors will be embedded close to each other, hence the effects of other sensors presence nearby a specific sensor has studied here. Experiments

were conducted with a specific sensor and monitored in TDGS by placing several sensors nearby as shown in fig. 5.24 and fig. 5.25 and fig. 5.26.

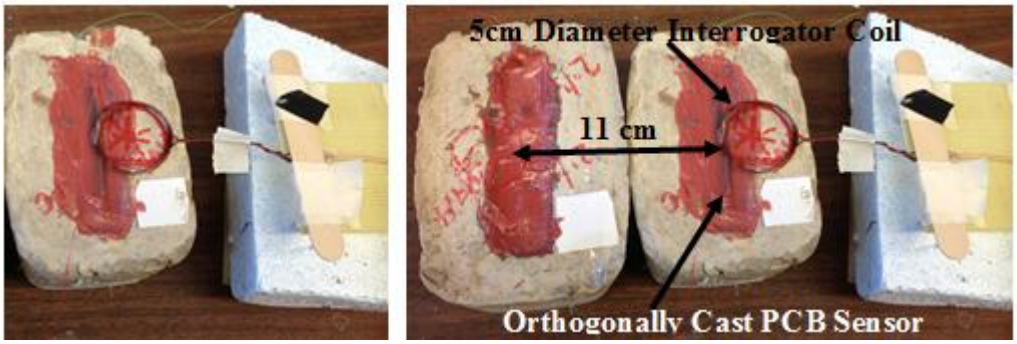

(a) (b)

Figure 5. 24: (a) Only the Monitored Senor (b) Monitored Sensor next to another sensor

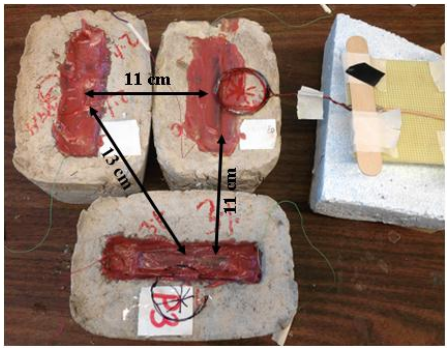

Figure 5. 25: Monitored Sensor next to two other sensors

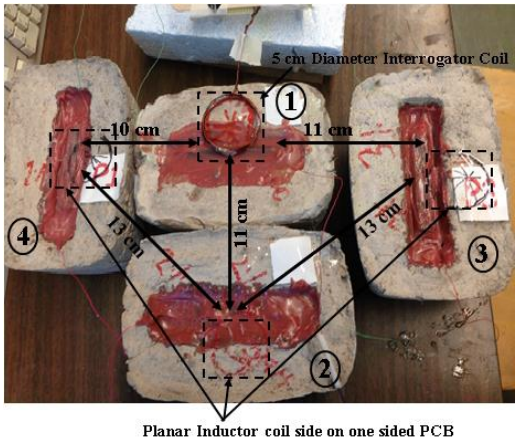

Figure 5. 26: Monitored sensor surrounded by three sensors

Table 5.7 demonstrates the sensor response surrounded by several sensors and the numbering of the sensor has shown in fig. 5.25.

Table 5. 7: PCB Sensor performance with presence of several Sensors

Sensor No.	Resonant Frequency (MHz)	Frequency Change (kHz), Δf	Equivalent Voltage (mV), ΔV
One sensor (1)	5.7687		
Two Sensors (1 &2)	5.7682	0.500	0.3
Three Sensors (1, 2 &3)	5.7661	2.600	1.6
Four Sensors (1, 2, 3 &4)	5.7657	3.000	1.9

5.12 Moisture Diffusivity for Mortar Specimen using Diffusion Test

In this work, a Diffusion test with a 100% relative humidity was done on one of the mortar block to find out the moisture diffusivity of the mortar. The mortar specimen was made using ~0.155 water/mortar ratio. Here, water absorption technique was used to find out the moisture diffusivity of the mortar (Kumaran, M.K, 1999). The dimensions of the cylindrical shape mortar specimen were 15cm diameter and 6cm height. For this test, the mortar specimen was tightly sealed by Para film and edge of the specimen was glued by electrical tape as shown in fig. 5.27. However, only bottom and top of the specimen were exposed for having a clear understanding of moisture flow through bottom to top. The area of the specimen exposed in the water was 0.018 m^2. The density of the specimen was 2000.0 kg/m^3 in dry state. The specimen was submerged in the water and the area of the surface in contact with water was 0.018 m^2. From time to time the specimen was taken out from the water and using an absorbent tissue the wet surface of the specimen was dried to remove the droplets clinging to the surface, weighed and then put back in the

water bath. The increase of weight of the mortar specimen was linearly dependent on the square root of time as shown in fig 5.28.

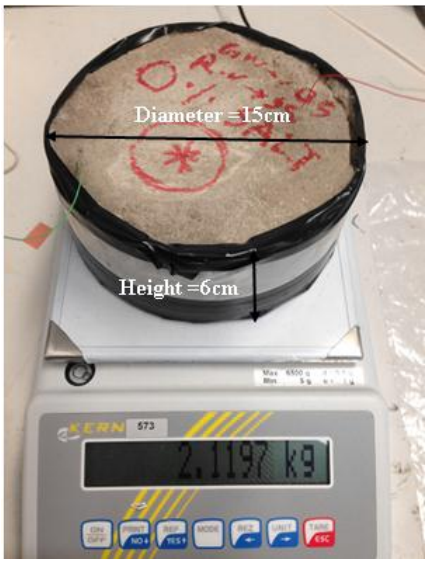

Figure 5. 27: Measuring the Mortar Block taken out from the water bath

The water absorption coefficient, A, was determined from the slope of the straight line in fig 5.27 to be 0.016 kg $m^{-2}s^{-1/2}$. The measured density of the soaked mortar specimen, $w_{l,}$ was 2161 kg/m^3. For direct use of the transport equation, which is not given here, the following eqn. gives an average value for the moisture diffusivity (Kumaran, M.K, 1999).

$$D_w = \left(\frac{A}{w_l}\right)^2 \qquad (5.\ 8)$$

Substituting the value of A and w_l in eqn. 5.12 gives D_w = 5.4×10^{-11} m^2s^{-1}. The moisture diffusivity depends on the materials, water/cement ratio, relative humidity etc. However, the moisture diffusivity of the concrete is in the range of 10^{-14} m^2/s which is 1000 time lower than Quickrete Mason Mix mortar (Samson, Maleki, Marchand, & Zhang, 2008). Therefore, mortar has been used instead of concrete in all of our experiment to carry the

experiment in month than a couple of years but the chemistry of two materials is similar (Perveen, Bridges, Bhadra, & Thomson, 2013).

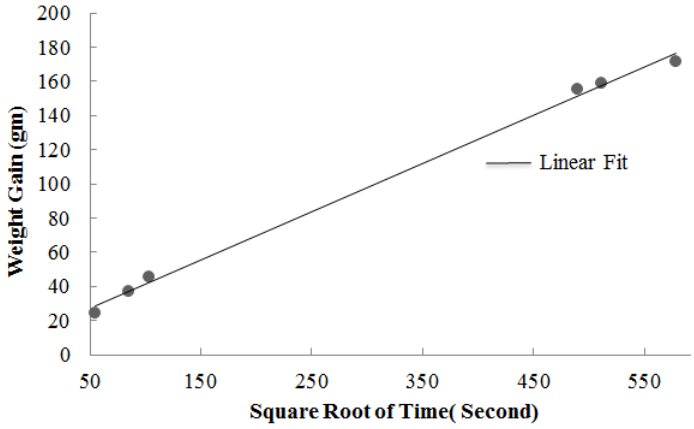

Figure 5. 28: Diffusion test results where the weight gain of mortar specimen was linearly dependent on the square root of time

5.13 Embedded Sensor performance with separation distance

As mentioned in sec. 5.6, the orthogonally coupled sensor limits the interrogation distance from the concentrically coupled sensor as the mutual coupling is the fraction of the flux of the interrogator coil that cuts the secondary coil, and is a function of the geometry of the system ("Resonant inductive coupling", n.d). During an accelerated corrosion test as described in sec. 5.15, the sensor performance was measured with different interrogation distance to determine the corrosion potential error that comes from the changing separation distance between interrogator and sensor coil (Bhadra, Thompson, Kordi, Bridges, & Thomson, 2010). Table 5.8 demonstrates the results for thick (2×6mm) PLEXIGLAS sealed sensor with changing separation distance. In table 5.8, the corrosion potential was extracted from the sensor resonant frequency using eqn. 5.12, was derived for PLEXIGLAS with air gap sealed embedded sensor with adding correction factor ~ 71 mV as described in sec. 5.15.2.

Table 5. 8: PCB Sensor performance with different interrogation distance

Separation Distance, d=cm	Measured Voltage using Agilent 34401A (V=mV)	Resonant Frequency(MHz)	Corrosion Potential using conversion eqn. 5.9
2	-194.80	6.0821	195.60
3	-194.53	6.0828	196.07
4	-194.02	6.0829	196.13
5	-192.19	6.0826	195.93

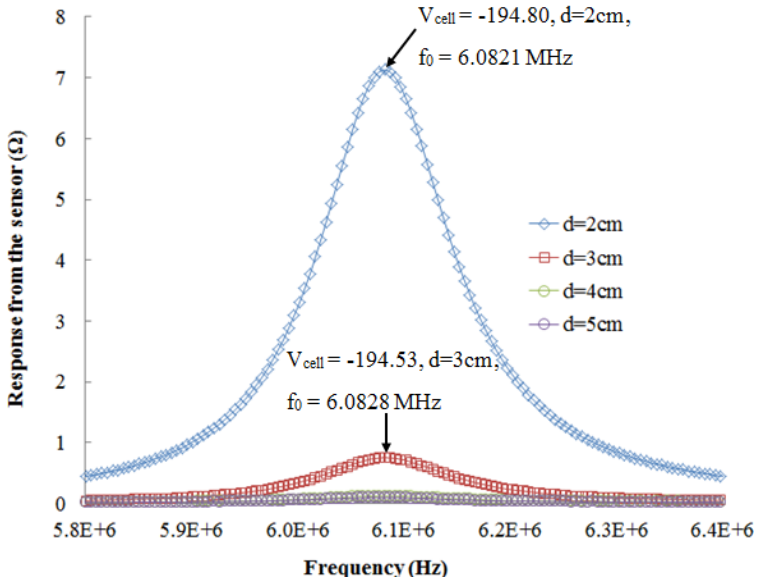

Figure 5. 29: Sensor performance with Separation distance

Fig.5.29 and fig. 5.30 show the graphical representation of the sensor response under different operating conditions. An obtainable resonant peak was detected with a maximum separation distance of 5 cm for orthogonally coupled sensor which gives a measurement error of less than 0.048%. This translates to a voltage resolution of 2.9 mV. Table 5.9 demonstrates the signal to noise ratio of the sensor under test. For signal to noise ratio (SNR) measurement, the same sample was being used as in fig. 28 and fig.29. Whenever the measurement was taken, the direct potential from the steel reinforcement was stable.

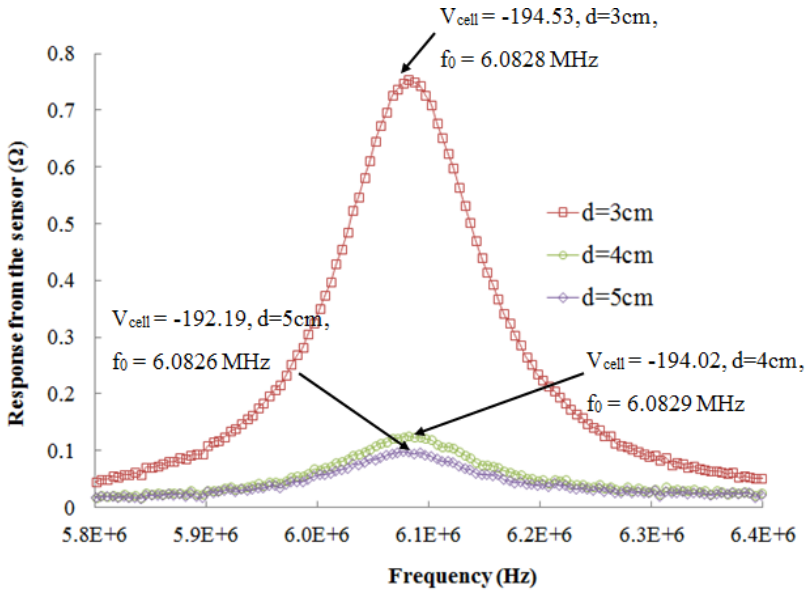

Figure 5. 30: Sensor performance with Separation distance continued

The sensor performance was measured in precision Impedance Analyzer (Agilent 4294A). For SNR calculation the bandwidth of the system was set to 97 kHz and frequency was swept from 5.98 MHz to 6.18 MHz with 300 evenly distributed measurement points with no averaging. However, the maximum resonant frequency shift, 8.8 kHz, for noise comes from the 4cm interrogation distance corresponds to 5.40 mV.

Table 5. 9: Signal to Noise ratio for PCB Sensor with separation distance (Bhadra, S., 2010)

Separation Distance, d=cm	Measured Voltage using Agilent 34401A (V=mV)	Resonant Frequency (MHz)	Measurement error for noise equivalent in mV	SNR(dB)
2	-192.11	6.0800	NIL	58.5
3	-192.17	6.0804	0.25	48.6
4	-192.15	6.0712	5.40	32.1
5	-192.11	6.0733	4.11	25.4

Fig. 5.31 and fig. 5.32 describe the sensor performance as changing SNR with different interrogation distances. A curve fitting algorithm was used to estimate the

sensor resonant frequency but the increasing separation distance imposes surrounding noise giving a maximum, 0.145% measurement error of sensor resonant frequency for an interrogation distance of 4cm.

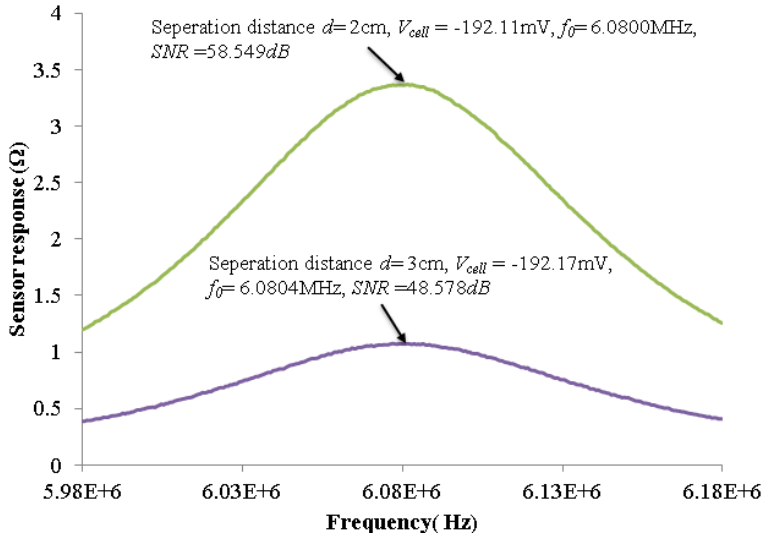

Figure 5. 31: Sensor performance with Separation distance

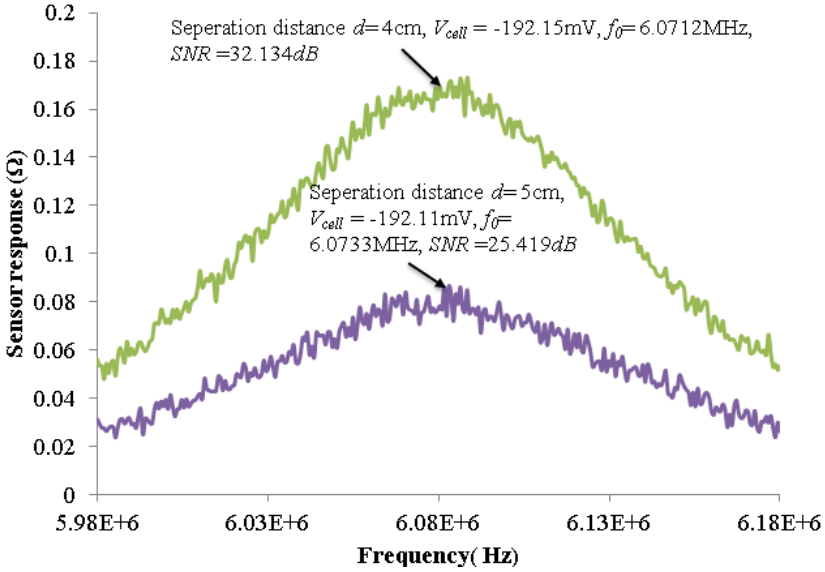

Figure 5. 32: Sensor performance with Separation distance continued

5.14 Moisture effects on the Corrosion Potential of the embedded sensor in mortar

Moisture effects on the measured and extracted (Resonant frequency) corrosion potential was measured from one of the embedded sensor (same sample used in sec. 5.11 and sec 5.13) response kept under in accelerated corrosion test as described in details in sec. 5.15. At the end of the accelerated corrosion test, the mortar specimen (2×6mm Thick PLEXIGLAS Sealed sensor) was taken out from the salt bath and dried in air for 13days. The potential difference was directly measured at the electrodes, V_{cell} = -190.48mV. The obtained resonant frequency for this dry condition was 6.0748 MHz and using eqn. 5.11 the converted voltage for this resonant frequency was 190.78 mV (negative potential) having a small 0.32 mV deviation from the direct measurement. During the previously measured wet condition, a directly measured V_{cell} = -195.80 mV and the obtained resonant frequency was 6.07745 MHz.

Table 5. 10: Moisture Effect on Corrosion of Steel Reinforcement

Condition of Mortar Specimen	Direct Measurement (V_{cell} = mV)	Resonant frequency (MHz)	Converted Potential from resonant frequency(mV)	Frequency Change, Δf (kHz)	otential Change, ΔV, mV from resonant frequency	Potential Change, ΔV, mV from direct measurement
Dry	-190.48	6.0748	190.80	~5 kHz	1.74	5.32
Wet	-195.80	6.0775	192.54			

For this resonant frequency the converted potential was -192.5434 mV showing a deviation of 3.2566mV from the direct measurement. The dry-to-wet resonant frequency difference was 2.65 kHz corresponds to an equivalent potential of 1.74mV (using sensitivity 1.53 kHz/mV because this thick PLEXIGLAS sealed sensor has the sensitivity

same as the epoxy sealed sensor), whereas the direct measurement showed a difference of 5.32mV. Table 5.10 compiles all the described results for determining the moisture effect on the corrosion potential (Sharmistha Bhadra and Douglas J Thomson and Greg, E. Bridges, 2013). Fig. 5.33 shows a prototype sensor block dried for 13 days after accelerated corrosion test. Salt is visible on the surface (each side) of the mortar block indicating that specimen was already saturated with salt.

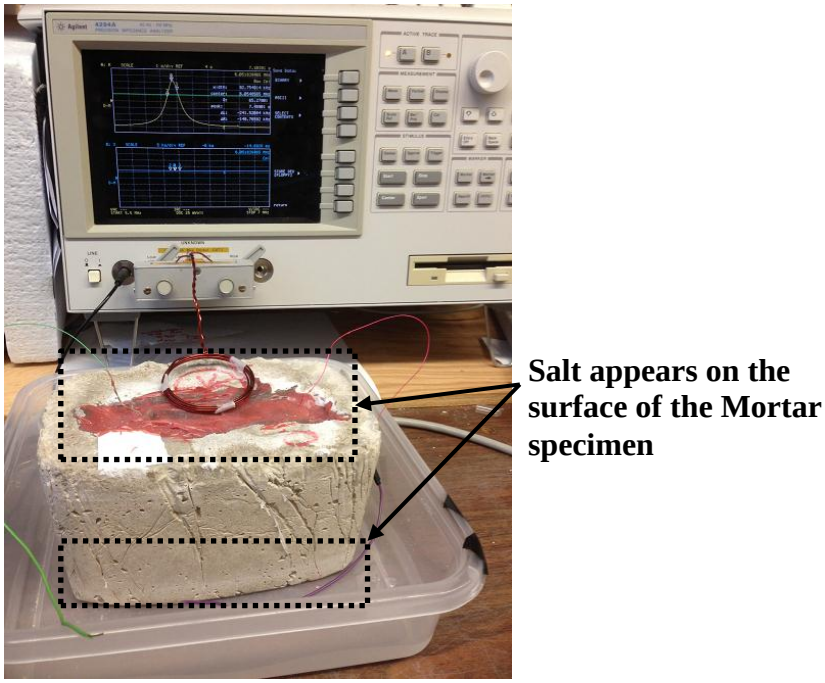

Figure 5. 33: Visible salt on the surface of the mortar block when it was left for drying 8 days after accelerated corrosion test

5.15 Accelerated corrosion Test on PCB sensor in NEW and EXISTING structures

An accelerated corrosion test was carried out on embedded PCB corrosion sensor using sealed sensor described in sec. 3.3.2.2-3.3.2.4. The specimen block is made by Quickrete mason mix (type S mortar, no. 1136). However, the installation of the sensor in

the mortar specimen to simulate the existing structure was slightly different from the demonstrated technique in sec. 5.7 and sec. 5.8. Corrosion in concrete is a slow process because the diffusion coefficient of concrete is much lower than cement based mortar as shown in sec.5.12. The following equation shows how the diffusion coefficient over a distance is related to time

$$< x^2 >= q_i D t \quad (5.9)$$

Where x is the mean distance from the starting point that a molecule will have diffused in time, t. q_i is the numerical constant which depends on dimensionality: q_i =2,4 or 6 for 1,2 or 3 dimensional diffusion. D is the diffusion coefficient (usual units are Cm^2S^{-1}) and t is the time (Crofts, A., 1996), (Perveen, Bridges, Bhadra, & Thomson, 2013). For our accelerated corrosion tests, we have used cement based mortar that has higher diffusion rates than regular concrete.

5.15.1 Making of Mortar specimen to simulate Existing and New Structures

The existing structure already contains corrosion-causing substances. The built-in structure was being made by introducing chlorides (by weight) with mixing pour water of the mortar .First, the mortar specimen was made mixed with 0%(no salt), 1%, 2% and 3% salt by weight of the mixing water (Pakshir & Esmaili, 1998). Afterward a 20mm slot was modeled made in the mortar specimen and left for 30 days for air curing as shown in fig 5.34(a) first block. Thereafter, the sensor was embedded in fresh grout filling the bottom ~15 mm of the slot and left 7 days to cure the grout. After 7days of curing, the slot was filled with construction epoxy (HIT-RE-500 Epoxy Adhesive) in order to simulate conditions that would be used in the field as described in fig 5.33. The sensor

was designed to fit into a 20 mm slot cut into the concrete. This allows the sensor to be installed on existing structures. The size is compatible with the typical 50 mm to 75 mm cover of concrete over steel reinforcing. Table 5.11 explains the mortar/ water ratio and the amount of salt introduced making the existing structure.

Table 5. 11: Composition of ingredients for making mortar specimen

% Salt Mixed Mortar Specimen for both Epoxy & PLEXIGLAS sealed sensor	Mortar weight (gm)	Salt (NaCl) (gm)	Water (gm)	Water/ Mortar Ratio
0%	2757	NIL	~ 450	0.163
1%	2703	4.19(~ 4)	~ 419	0.155
2%	2705	8.4(~8.5)	~ 420	0.155
3%	2747	12.78 (~13)	~ 426	0.155

A block diagram of simulating the existing structure and the installation of sensor for measuring the existing structure is shown in fig. 5.34.

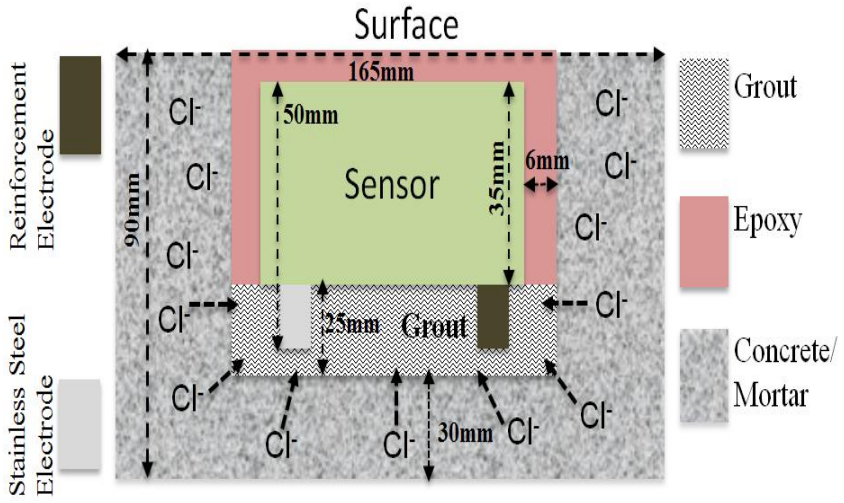

Figure 5. 34: A Block Diagram for simulating the built-in structure contaminated with corrosion causing substances

From this block diagram, the presence of chlorides in the civil structure accelerates the corrosion of two electrodes, gives a significant variation of corrosion potential based on the concentration level of the chlorides. Once two electrodes are embedded in the fresh (no salt mixed) grout and cured for several days, then chlorides from the structure slowly penetrates to the grout and eventually reaches to the electrodes initiating the corrosion of steel reinforcement with presence of moisture and O_2. However, the corrosion rate of the steel reinforcement depends on several factors here such as chloride concentration, exposed area of two electrodes, distance from electrodes end level embedded in the fresh grout to the chlorides mixed level, grout height, porosity of the mortar specimen as well as porosity of grouts. Fig. 5.35 and fig. 5.36 explains the mortar specimen preparation and the sensor installation in the mortar specimen.

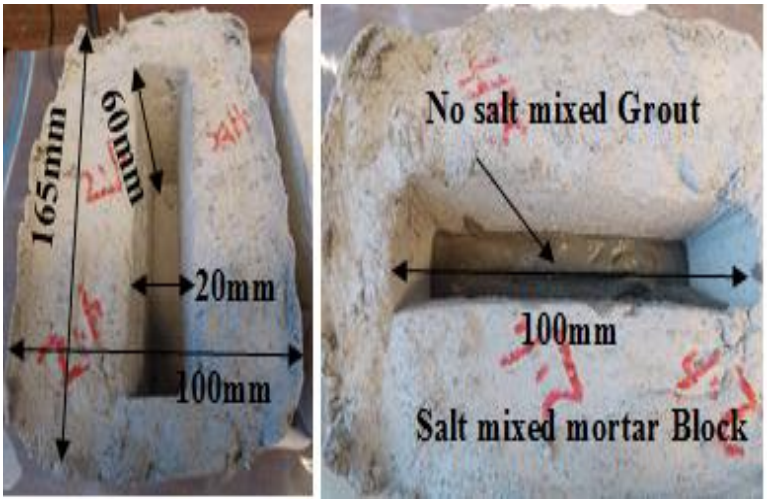

(a) (b)

Figure 5. 35: Making of Mortar specimen

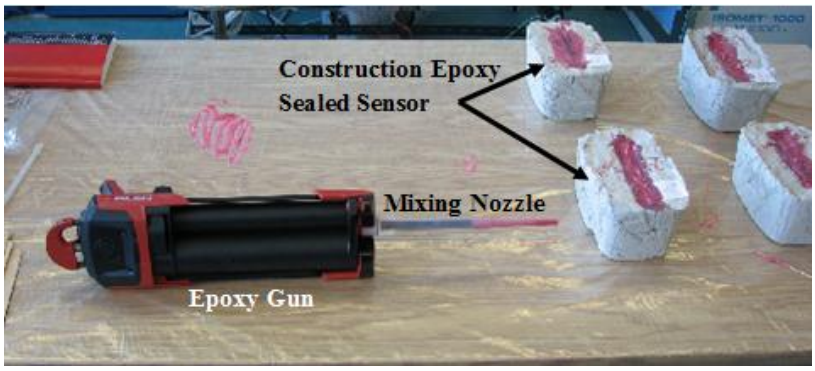

(a) Slot filled by construction Epoxy

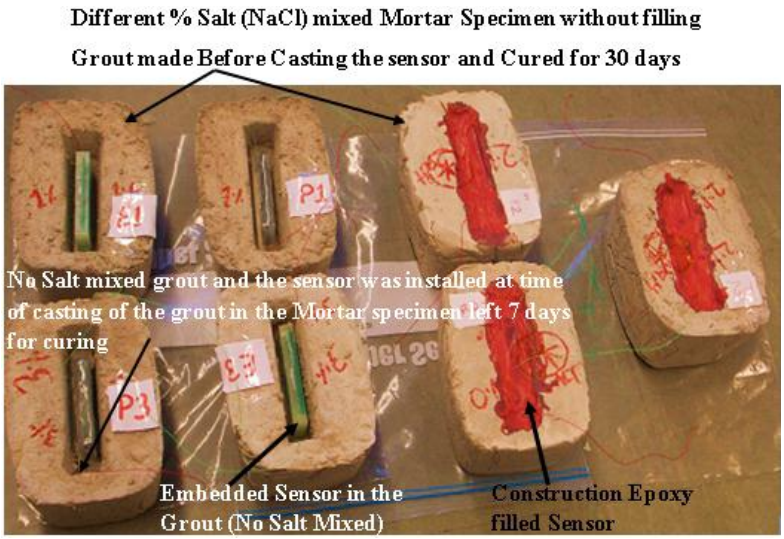

(b) Sensor embedded in the grout and fully embedded sensor inside the mortar filling by construction Epoxy

Figure 5. 36: Different step of preparing the mortar specimen to simulate the existing civil structures

5.15.2 DC Calibration

A DC calibration was done on embedded sensor in the mortar specimen varying the source voltage from -100 mV to 500 mV. During all previous accelerated corrosion tests, in the very first day of experiment the reference electrode had shown some electronegativity compared to the reinforcement electrode, however, when the corrosion was in progress it reverts. It might be the reason of mortar/steel interface attributes. Thus, for the DC calibration the source voltage was varied from -100 mV instead of 0 mV. Fig.

5.37 shows the DC calibration on embedded epoxy sealed sensor which is a linear fit. From the linear curve fit eqn. 5.11 of embedded PCB sensor in the mortar specimen is obtained which relates the negative voltage applied across the two electrodes, V to the resonant frequency of the sensor, f_0 . The slope, ~0.145 MHz / 100 mV is obtained from the linear fit.

$$V(mv) = 727.6 \times f_0(MHz) - 4152.2 \qquad (5.\ 10\ )$$

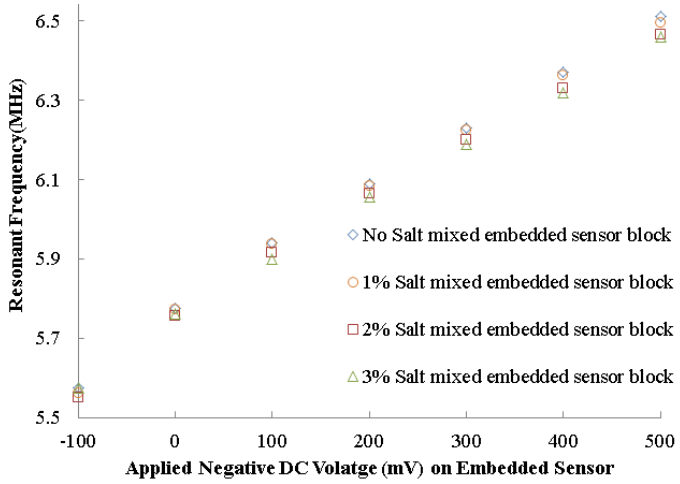

Figure 5. 37: DC Calibration Results of Embedded Sensor (Epoxy Sealed Sensor)

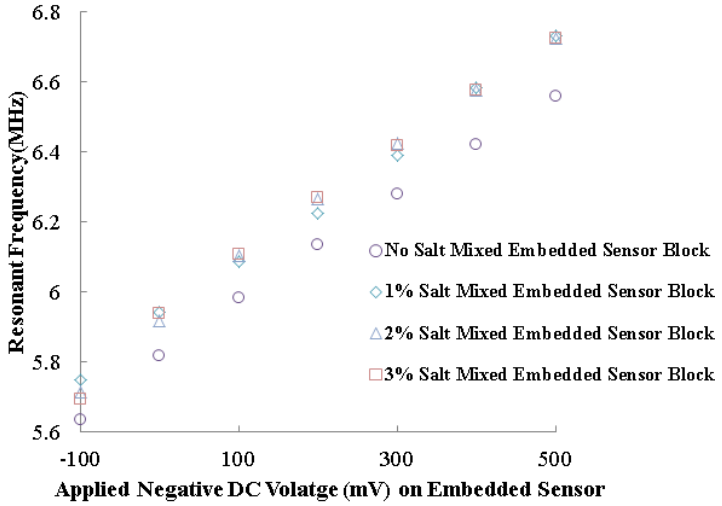

Figure 5. 38: DC Calibration Results of Embedded Sensor (PLEXIGLAS with Air Gap Sealed Sensor)

Furthermore, fig. 5.38 demonstrates the DC calibration on the PLEXIGLAS with air gap sealed PCB sensor as a linear fit, whereas, only the no salt mixed embedded sensor sealed by 2×6mm thick PLEXIGLAS shows the deviation, ~116 kHz over -100 mV to 500mV equivalent voltage deviation ~71 mV from the sensor sealed by PLEXIGLAS with air gap. From the linear curve fit eqn. 5.12 of embedded PCB sensor in the mortar specimen is obtained which relates the negative voltage applied across the two electrodes, V to the resonant frequency of the sensor, f_0.

$$V(mV) = 658.2 f_0(MHz) - 3878.9 \quad (5.\ 11)$$

The slope, ~0.160 MHz/100 mV is obtained from the linear fit. Table 5.12 compiles the sensor response under different operating conditions including their Q-factor, voltage deviation, ΔV and fringing capacitance change, ΔC.

Table 5. 12: PCB Sensor Response under Different Operating Conditions

Sensor No. (No. refers to % Salt)	Frequency in Air (MHz)	Frequency (MHz) of sealed sensor	Frequency (MHz)after fully Installed	Capacitance Change (ΔC), pF, after fully Installed	Equivalent Voltage (mv), ΔV, after fully Installed	Q-factor(f0/Δf) After installation
Epoxy Sealed Sensor [Sensitivity of the sealed sensor = ~1.53 kHz/mV]						
0	5.960	5.840	5.694	1.90	95.4	
1	5.960	5.840	5.702	1.79	90.2	
2	5.960	5.840	5.711	1.67	84.3	~50-68
3	5.960	5.830	5. 696	1.75	87.6	
PLEXIGLAS with Air Gap sealed sensor [Sensitivity of the sealed sensor = ~1.63 kHz/mV]						
1	5.960	5.955	5.925	0.36	18.4	
2	5.960	5.950	5.915	0.42	21.5	~60-80
3	5.960	5.950	5.909	0.49	25.2	

5.15.3 Results

An accelerated corrosion test was carried out on each block for 23 days but the test duration in tap water and 5% salt mixed tap water for each block were not same. Because the premixed chlorides has a significant effect on the corrosion rate of the mortar/concrete based on the concentration level of the premixed chlorides as described in fig. 5.34. However, the accelerated corrosion test was done under 100% relative humidity by tightly sealing the lid of the test jar using Para film shown fig.5. 39. As mentioned in sec. 4.5 that the corrosion rate of the steel reinforcement is influenced by several environmental factors. But the scope of this thesis was to study the effects of chlorides on corrosion behavior of the steel reinforcement. Fig. 5.39 and fig. 5.40 show the accelerated corrosion test set up in TDGS and impedance measurement system.

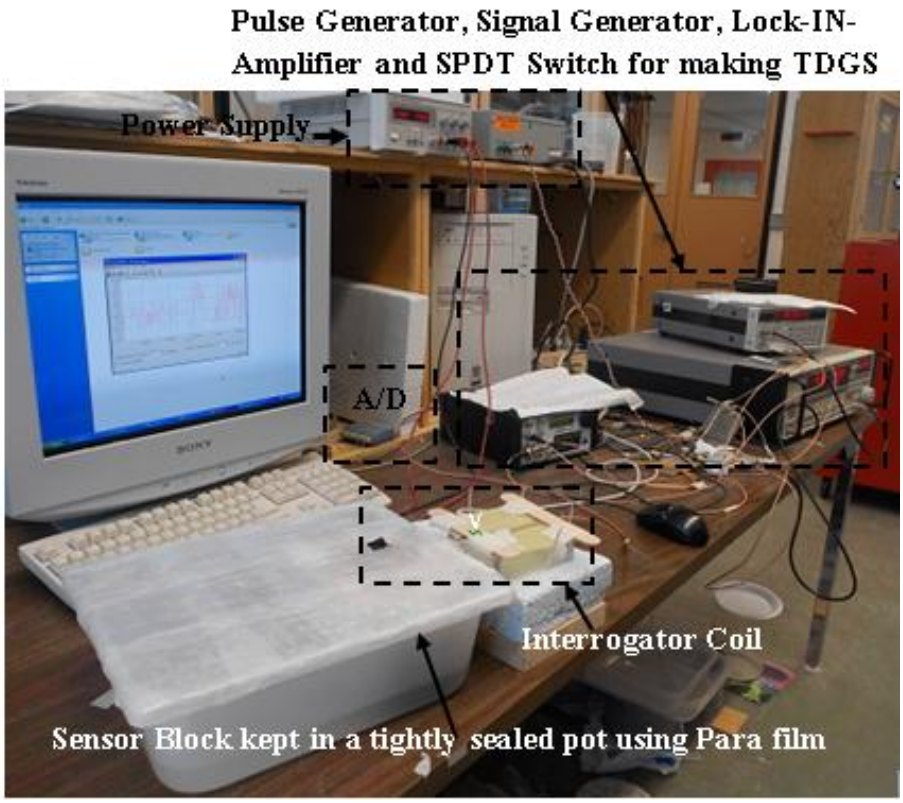

Figure 5. 39: Accelerated Corrosion Test Set up in Time Domain Gating System (TDGS)

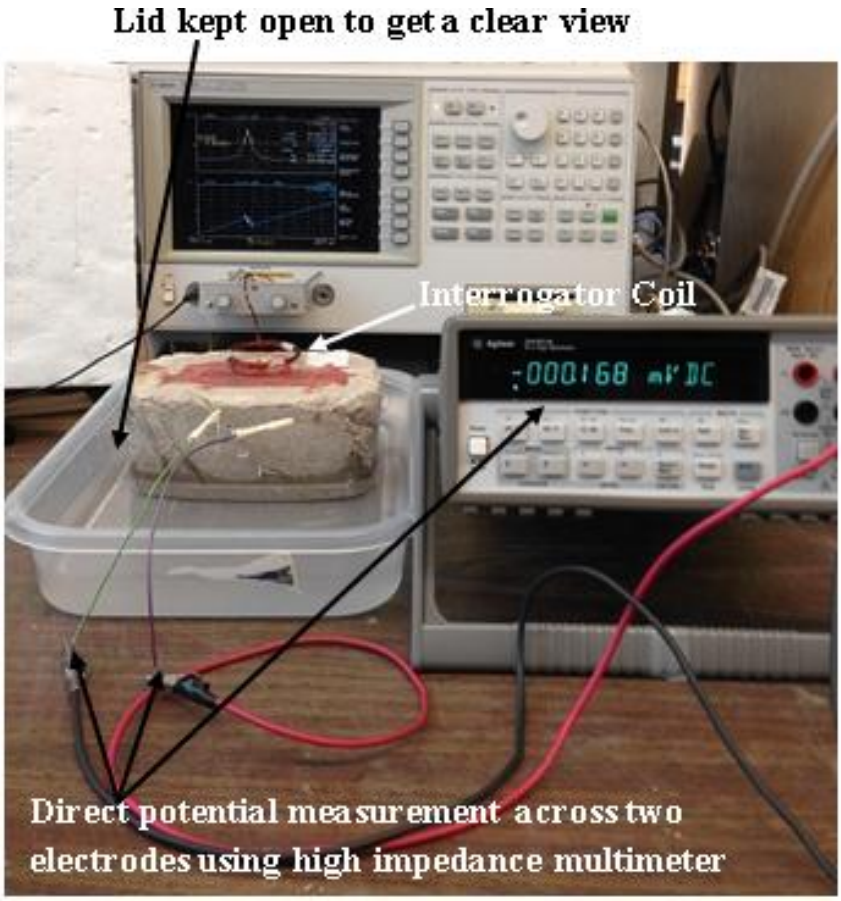

Figure 5. 40: Accelerated Corrosion Test Set up in Impedance Measurement System (Agilent 4294A)

The prototype no salt (0%) mixed mortar specimen was cured 30 days, afterward it was submerged in tap water for 3 days and the sensor resonant frequency was tracked down using TDGS or Agilent 4294A as the measured corrosion potential using a high impedance multimeter (Agilent 34401A or A/D). After 3 days, it was put in a 5% NaCl (salt) by weight mixed solution with water. The corrosion potential was then measured every 20 minutes. The test was carried out for 23 days.

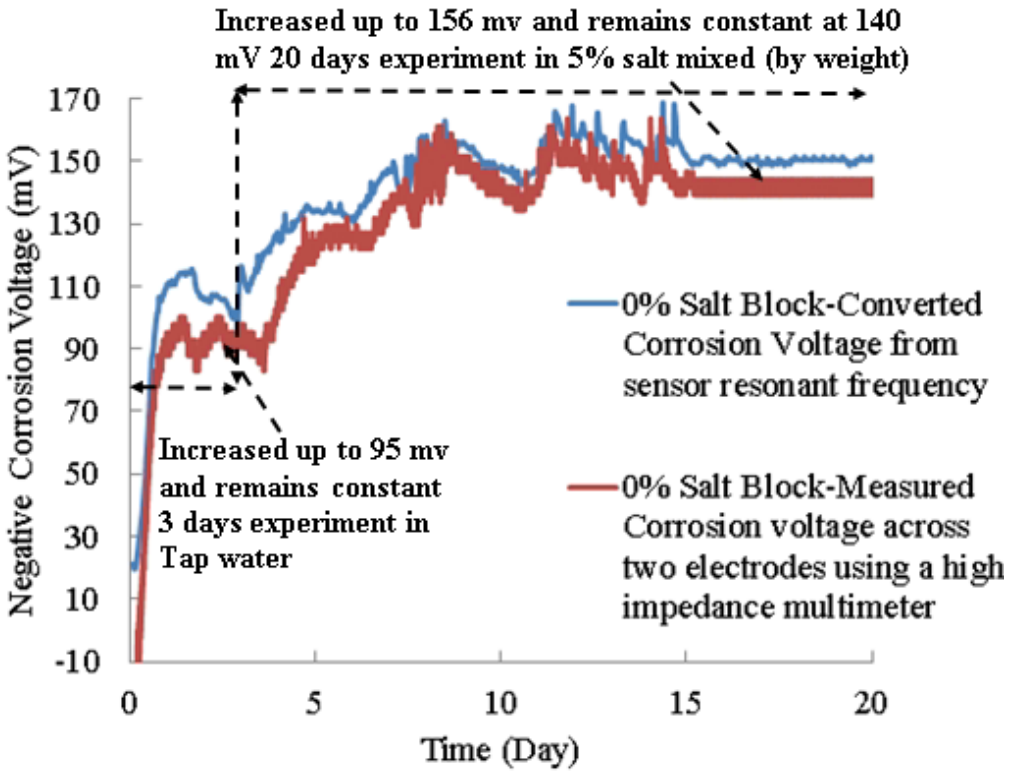

Figure 5. 41: Extracted corrosion potential [no salt mixed Epoxy Sealed Sensor] using equation 5.11 and measured corrosion potential. Note the uncertainty in the measurement is less than 10 mV.

The result of these measurements is shown in Fig. 5.41. In this experiment, the potential across the electrodes increased up to 95 mV and then remained stable in plain water over the 3 days of the measurement. In 5% salt mixed water, the potential further started to increase and it went up to 156 mV over the 20 days of the measurement. It indicates that the chloride front has reached the reinforcing bars and the corrosion process is in progress. The difference of potential between measured and extracted value is less than 15 mV. The possible reasons for this difference is the finite impedance of the cell rather than low impedance which was used to obtain equation 5.11 and 5 mV resolution of A/D which was used to log cell potential.

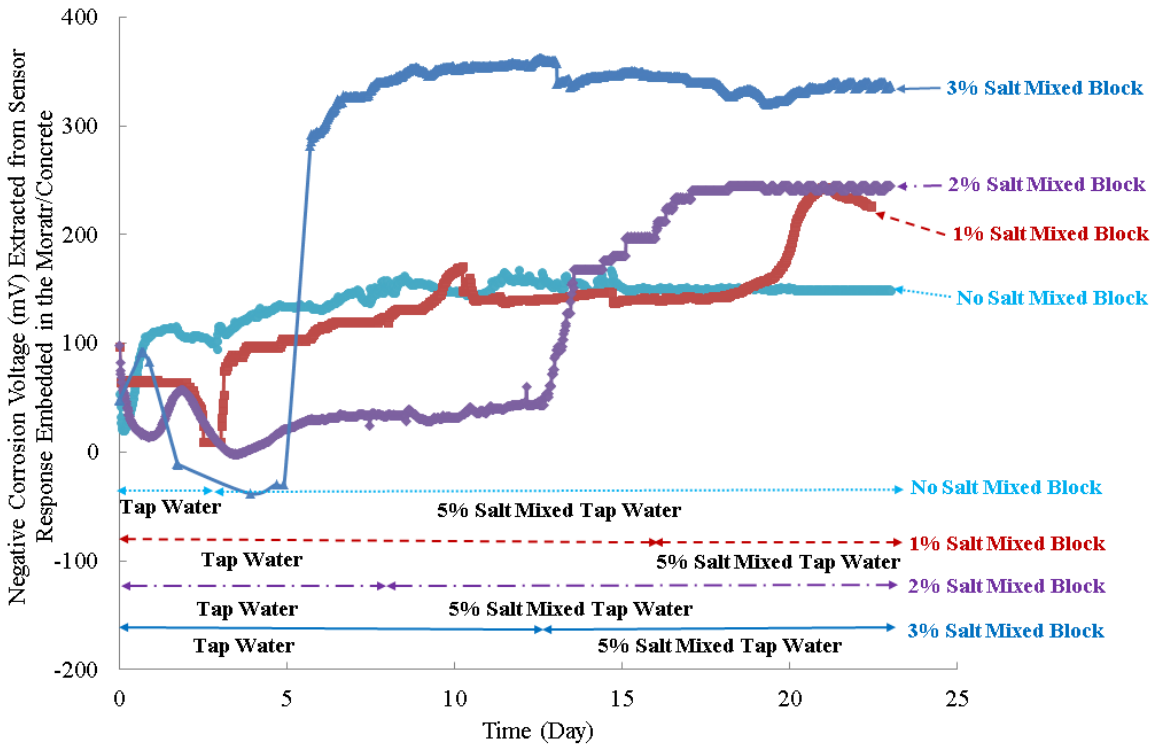

Figure 5. 42: Corrosion potential extracted from embedded sensor in mortar mixed with no salt, 1%, 2% and 3%salt prior embedment of the sensor in the mortar specimen showing how the chloride concentration in the mortar specimen affects the corrosion potential of steel reinforcement using eqn.5.11. [Epoxy Sealed Sensor]

Fig. 5.42 shows the effects of chloride concentration on the corrosion rate of the mortar using collected data from the epoxy sealed sensor response. For 3% salt mixed mortar specimen, it is kept under test for 13 days in tap water, which shows the corrosion potential level up to 345 mV, and then rest of the test was carried out in 5% salt mixed tap water. In this duration of the test, the corrosion potential decreased 20 mV from 345 mV and remains constant at 325 mV, representing the reference electrode is also starting to corrode. The 3% salt mixed block has the highest corrosion potential, and the no salt mixed block has the lowest. The 1% and 2% salt mixed block show almost the same elevated level of corrosion voltage up to 240mV. Fig. 5.42 demonstrates the chloride

effects on corrosion process of steel reinforcement for PLEXIGLAS sealed sensor. An accelerated corrosion test was carried out for 30 days on each block. This corrosion potential was extracted from the response of PLEXIGLAS with air gap sealed sensor.

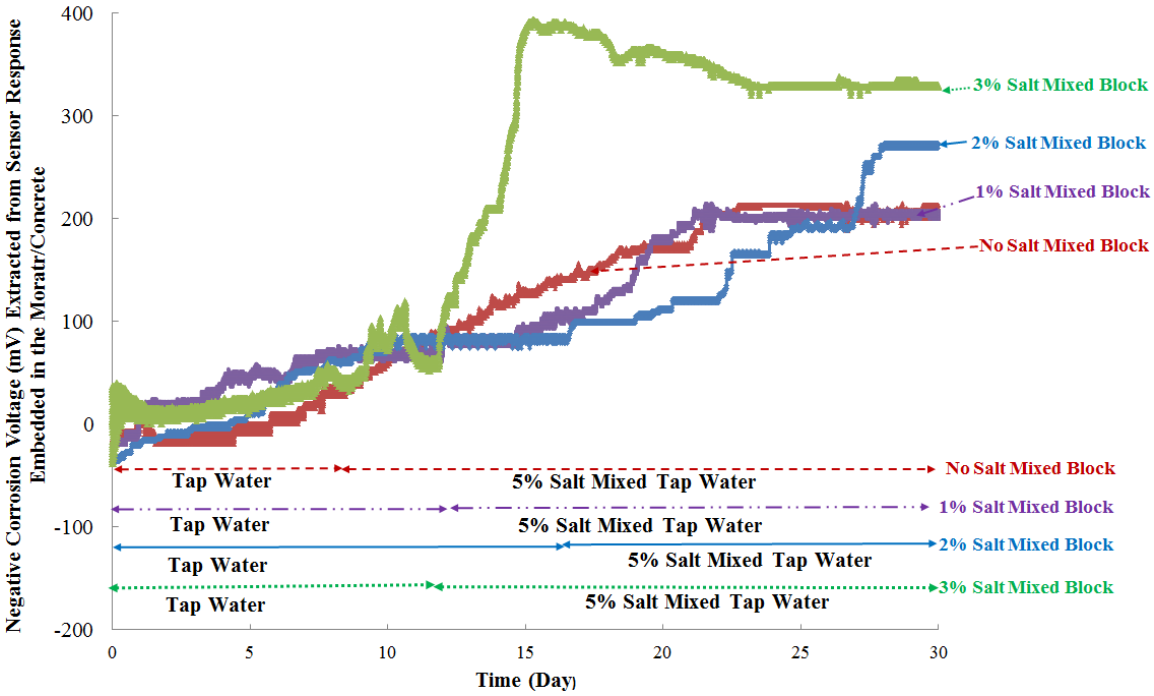

Figure 5. 43: Corrosion potential extracted from embedded sensor in mortar mixed with no salt, 1%, 2% and 3% salt prior embedment of the sensor in the mortar specimen showing how the chloride concentration in the mortar specimen affects the corrosion potential of steel reinforcement using eqn. 5.12. [PLEXIGLAS with Air Gap Sealed Sensor]

As mentioned before, the accelerated test duration in tap water and in 5% salt mixed solution for different salt mixed block were not same. From fig. 5.43, 3% salt mixed block was submerged in the tap water for 12 days showing a rise of negative corrosion potential up to 50 mV. While it was submerged in 5% salt mixed solution, the potential raised up to 391 mV and gradually it became stable at 332 mV. Therefore, a sudden rise of corrosion potential indicates the rate of corrosion initiation how fast the

potential changes as well as the level (numerical value) of potential and the stable potential indicates the corrosion is in progress. Once the corrosion initiation happens, the reinforcement steel loses electrons in anodic and cathodic reaction with presence of moisture and oxygen and gradually rust product forms on the surface of the steel reinforcement. The exposed area of the electrodes are small and whenever rust products forms all over the exposed steel reinforcement, afterward reference electrode starts to corrode that makes potential difference lower which may give false indication of the corrosion rate of the structure. Hence, analyzing the health of a civil structure using this sensor requires considering the previous data collected from this sensor. In fig. 5.42, 2% block was kept in tap water for 12 days show a stable potential level at 83 mV and for rest of the test was in the 5% salt solution shows that the potential level raised up to 273 mV. However, the no salt mixed and 1% salt mixed block show the same elevated level of potential but the potential change rate was different. For the no salt block, the potential from the electrodes steadily changed and became stable at 208 mV. Conversely, the 1% salt mixed block showed a fairly steady potential level at 65 mV in tap water, but in salt water it shows a sudden potential change and became stable at 208mV. The result was expected from this accelerated test based on the existing chlorides in the structure. Mixed chlorides with the mortar have three additional effects on the subsequent corrosion rates. First mixed chlorides results in a coarser capillary pore-size distribution at a constant water-cement ratio (w/c) (Young, 1988), (Hope et al., 2001), (Halamickova, Detwiler, Bentz, & Garboczi, 1995) which allows quicker ingress of additional chlorides, faster carbonation rates and also reduces the resistivity of the concrete. Second, the chlorides alter the pH of the concrete pore solution and its electrical conductivity. However, both of

these factors lead to an increase in the corrosion rate. Finally, the mixed chlorides alter the pH of the solution which affects both the chloride binding and the chloride threshold value for corrosion (Hope et al., 2001). Furthermore, the time duration for the epoxy sealed sensor and the PLEXIGLAS with air gap sealed sensor were not same, though both sealed sensors were installed in similar % salt mixed mortar specimen. So, the probability of this deviation has already been mentioned in sec. 5.15.1, and may come from the mortar specimen which was not uniformly made.

From the above test results in fig. 5.42 and fig. 5.43, it can be concluded that the mixed chloride concentration in the mortar has a significant impact on the corrosion of the steel reinforcement. The mixed higher chloride concentration in the mortar initiates the corrosion earlier, and shows the high corrosion rate. The sensor can monitor the health of the reinforced structure as corrosion potential produced from two electrodes with an average of less than 20 mV resolution using the described encapsulation technique in sec. 5.10.

In fig. 42 and fig. 5.43, it takes almost 5 to 20 days to see the significant corrosion in the cement based mortar structure based on the premixed chloride concentration. However, the embedded sensor may take up to 60 days to see the significant corrosion in the existing reinforced concrete structure. Since chlorides take many years to diffuse into concrete used for civil structures these sensors will respond fast enough to be used in existing structures.

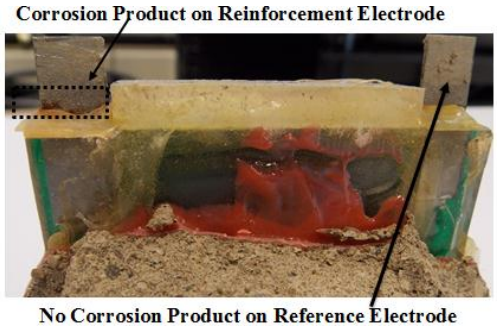

(a) The sensor from no salt mixed Mortar Specimen

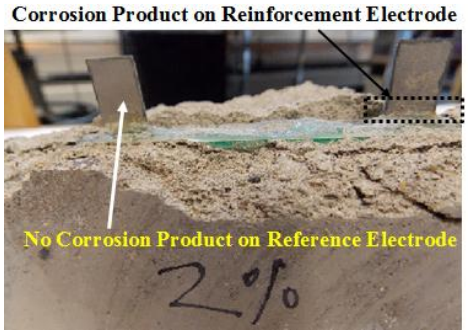

(b) The sensor from 2% Salt mixed Mortar Specimen

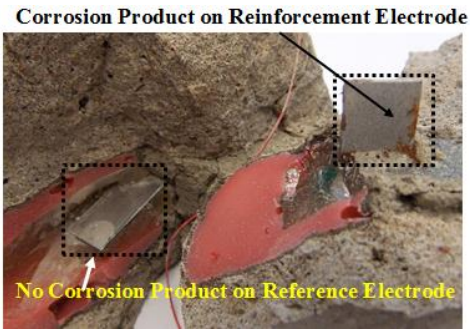

(c) The sensor from 3% Salt mixed Mortar Specimen

Figure 5. 44: The sensors embedded in no salt mixed, 2% and 3% salt mixed mortar specimen were taken out from the mortar specimen almost 1-4 months after the accelerated corrosion tests ended. The sensor from 3% salt mixed has the largest corrosion (rust) product than the sensors from 2% and no salt mixed mortar specimen.

Fig. 5.44 shows the corrosion product on the steel reinforcement of the sensor taken out from the no salt, 2% and 3% salt mixed mortar specimen. We can see that, the sensor from the no salt mixed mortar specimen has more rust on the steel reinforcement with 2% salt mixed specimen. This is because, the sensor from the no salt mixed block was kept inside the mortar more than 3.5 months after the accelerated corrosion test end, compared to the sensors from the 2% and 3% salt mixed blocks.

5.16 Summary

In the conclusion, chapter 5 summarizes the results from the PCB sensor under different operating conditions. Sec. 5.2 shows the fixed capacitor and the varactor modelling of the PCB sensor. Sec. 5.3 demonstrates the sensor performance with the different separation distances between the interrogator and the sensor coil. A DC calibration on PCB sensor is shown in section 5.4 to calibrate the sensor base line. Sec. 5.5 shows the comparison of the PCB sensor results from a TDGS and an impedance analyzer. Sec. 5.6 demonstrates the results from the off axis coupled PCB sensor with the interrogator coil. Sec. 5.7 and sec. 5.8 show the accelerated corrosion tests on the embedded sensors in the different % salt mixed layered cement based mortar specimens and their results from the specimens. Sec. 5.9 and sec. 5.10 demonstrate the optimization process of the PCB sensor encapsulations from the harsh environment in the concrete/mortar structures. A specific sensor performance surrounded by other sensors is shown in sec. 5.11. Sec. 5.12 describes a diffusion test on one of the mortar specimen to find out the moisture diffusivity of the cement based mortar. Sec. 5.13 demonstrates the embedded sensor (in the cement based mortar) performance with different separation distances between the interrogator and the sensor coil. In this research work, the accelerated corrosion tests are carried out in tap water and 5% (by weight of mixing water) salt water. Therefore, sec. 5.14 explains the moisture effects on the extracted corrosion potential from the sensor resonant frequency. Finally, sec. 5.15 describes the accelerated corrosion tests and their results from the eight embedded sensors in the different % salt mixed mortar specimen to simulate the existing civil structures.

Chapter 6: Conclusion and Future Works

This research is focused on a passive wireless corrosion potential sensor for health monitoring of civil structures. The first part of the thesis describes the circuit modeling of the corrosion sensor. The main contribution of this research was optimization of the sensor and implementation in the field which was simulated in field environment created in the lab. Two geometrical designs "cylindrical shape" and "Printed Circuit Board sensor" part of this research were studied in this thesis. The cylindrical shape was optimized using different types of wires, electrodes and interrogator coil sizes. The PCB sensor was optimized using different thickness PLEXIGLAS/Epoxy and different length of the electrodes. The second part of the thesis was organized with the experimental results of both geometrical sensor designs. The sensor response was measured in different dielectric medium and was embedded in cement based mortar to simulate the sensor performance in new and existing civil structures.

The cylindrical shaped sensor was tested only in a new structure. The accelerated corrosion test shows that the sensor can measure the corrosion potential extracted from sensor resonant frequency is less than 20mV from direct measurement across two electrodes. The sensor sensitivity is 0.73 kHz/mV. This design shows a large base line shift in accelerated corrosion test with changing dielectric of the medium. Therefore, for optimization purposes the sensor is designed on Printed Circuit Board. The designed sensor on PCB is optimized using several thicknesses PLEXIGLAS, non-Conductive Epoxy and different lengths electrodes size. However, the enclosed PCB sensor using 2×6mm thick PLEXIGLAS and non-conductive epoxy sealed sensor embedded in cement

based mortar detect the significant corrosion potential almost in 5 to 20 days in existing structures using the novel casting technique described in section 5.15. The level of environmental isolation of less than 95 mV and 25 mV was achieved using sensor enclosing techniques of Epoxy and PLEXIGLAS with air gap sealing respectively. The embedded sensor in the reinforced concrete structures may take up to 60 days to see the significant corrosion. Since chlorides take many years to diffuse into concrete used for civil structures these sensors will respond fast enough to be used in existing structures.

The sealed PCB sensor sensitivity using 2×6mm PLEXIGLAS (with air gap) and non-conductive Epoxy are 1.63 kHz/mV and 1.53 kHz/mV. In comparison to the cylindrical shaped sensor, the PCB sensor has a reduced size of 90mm×50mm. For large scale deployments such as for testing in a large bridge decks, the sensor size need to be reduced. Furthermore, for optimized performance of the off-axis coupled sensor, we need to explore different orientation of the sensor coil with the PCB, and verify with low diffusion concrete using the casting technique described in section 5.15.

From fig. 5.42 and fig. 5.43, a linear relationship can be seen between the chlorides concentration and the potential difference from the different % salt mixed specimens. Using this sensor, the chlorides concentration in the existing civil structures can be detected indirectly from the produced potential across two electrodes. In near future, we will do further tests on different % salt mixed specimen only in the tap water to calibrate the sensor properly to indicate the chlorides concentration in the existing civil structures from the generated potential across two electrodes due to corrosion.

Appendix A

A.1 Inductance Calculation for PCB rectangular planar inductor coil.

```
clear all;
clc;
%planar inductance calculation using synthetic Asymptote where S is the spacing between inductor coil, dout and din are outer and inner diameter of the rectangular planar PCB coil.
S=0.000254;
dout=0.038;
din=0.01;
b1=(din-S)/2;
b2=(dout+S)/2;
a=b1/b2;
%calculation of shape factor for rectangular geometry dlen/dwid<<2:1, shape factor lf= 0.96, where length of the outer coil, dlen=4.8cm and width of the outer coil, dwid=3cm.
lf=0.96;
cf1= (1.07*a^3)-(0.92*a^2) +(0.3*a)+0.82;
% capacitance for solid quarter plate in Pico farad scale.
Aquarter= (b2)^2-(b1)^2;
e0=8.8542e-12;
Cquarter=cf1*e0*sqrt(8*pi*Aquarter)
Cquarterpf=Cquarter*10^12;
%calculation of far field capacitance when h tends to infinity means the ground plane is far from the spiral inductor. W is the turn width of the inductor coil.
W=0.0254;
Ws=W+S;
cf=0.865;
p11=1/(cf*e0*sqrt(8*pi*W*Ws));
p110=1/(cf*e0*sqrt(8*pi*Ws*Ws));
```

```
r0=4*(b1*b1+b1*b2+b2*b2)/(3*(b1+b2));
N=28;
M=(b1+b2)/Ws;
c1=1/(cf1*e0*sqrt(8*pi*Aquarter));
c2=(p11-p110)/(N*M);
c3=1/(4*pi*e0*r0);
c4=c1+c2-c3;
Cquarterfar=1/c4;
%calculation of near field capacitance when h tends to zero, means the
%ground plane is very near to the spiral inductor
h=0.0016;
c5=W/Ws;
Cquarternear= ((e0*Aquarter)/h)*c5;
m=1.42*(c5^0.22)*(h/dout)^0.15;
%c7=(Cquarterfar)^m+(Cquarternear)^m;
c8=Cquarterfar;
% Rectangular spiral Inductor calculation, where Lpcbcoil is the total
28turns inductance.
u0=4*pi*10^(-7);
c6=4*u0*e0*(N^2)*(b1+b2)^2;
L=c6/c8
Lpcbcoil=lf*L;
% formula of capacitance C to ground by synthetic Asymptote
% when h tends to infinity, the inductor appears to sit on the boundary
of a half space of air and dielectric er. This means that the inductor
is sitting on a homogeneous medium with effective dielectric constant
(er+1)/2. The far asymptote of the capacitance to ground is Cgfar and
near asymptote of the capacitance to ground is Cgnear. The synthetic
asymptote of the capacitance to ground is Cg.

cf2=0.9*(1-(din/dout))^(-0.18);
a1=cf2*e0*sqrt(32*pi*Aquarter)
er=4.4;
a2=2/(er+1);
a3=(1/a1)+(c2/4);
Cgfar=1/(a3*a2);
Cgnear=4*er*Cquarternear;
n=1.114*(1-(din/dout))^0.16*(W/Ws)^0.31;
```

```
a4=(Cgnear)^n+(Cgfar)^n;
Cg=(a4)^(1/n);
% Resistance calculation by synthetic asymptote
t=0.007;
k=1.2;
p=1.9;
f=5.96e6;
sig=5.8e7;
Lr=155e-2;
skindepth=1/sqrt(pi*f*u0*sig);
Rdc=Lr/(sig*W*t);
r1=sig*2*(W+t)*skindepth;
Rac=Lr/r1;
r2=(Rdc)^p+(k*Rac)^p;
R=(r2)^(1/p);
```

A.2 Quadratic-curve fitting algorithm for obtaining Resonant Frequency

```
clear all;
clc;
% Directly reading of Number of files from the measurement of coupled
coil sensor saved in Xcel file through MATLAB for obtaining Resonant
frequency, f and v vector contains the frequency column and real
impedance/voltage from the sensor response respectively.
how_many_files=No. of files;
freq=zeros(No. of files,1);
for a=1:how_many_files
    files{a} = strcat(num2str(a));
    fn=[files{a} '.xlsx'];
    nums=xlsread(fn);
    f=nums(:,1);
    v=nums(:,2);
for i=1:800
    p(i)=v(i)*v(i);
end
%a contains the maximum power value

maximum_power=max(p)
```

```
j=1;
%Includes points where power >=0.5a. 1 and fi vector contains the power
and frequency respectively for all those points. Fit 1/1 against fi to
a parabola (ax^2+bx+c). Resonant frequency= -b/(2*a)
for i=1:800
    if p(:,i)>=maximum_power/2
        power(j)=p(i)
        fi(j)=f(i);
        pin(j)=1/p(i);
        j=j+1;
    end

end
    p8=polyfit(fi,power,2);
    f_resonant=-p8(2)/(2*p8(1))
    freq(a)=f_resonant;

end
```

A.3 Self-Inductance and Mutual Inductance Calculation

```
clear all
clc;
%d means the distance (meters)between interrogator coil and the sensor
coil
d=[0.07,0.09,0.103,0.115,0.126,0.145,0.175,0.2];
%zrmeas means impedance at resonance for different distances
zrmeas=[3.3673E+00 1.1915E+00 5.8939E-01 3.0251E-01 2.1393E-01 1.2732E-
01 3.7396E-02 2.3779E-02];
znorm=zrmeas/zrmeas(1);

%u0 is permeability
u0=4*pi*1e-7;
%n1(number of turns in interrogator coil),rw1(radius of interrogator
coil's wire),r1(radius of total interrogator coil)and sig1 is relative
permittivity
n1=4;
rw1=0.0006;
```

```
r1=0.0255;
sig1=5.8e7;
%n2(number of turns in sensor coil),rw2(radius of sensor coil's
wire),r2(radius of total sensor coil)and sig2 is relative permittivity
n2=27;
rw2=1.27e-4;
r2=0.0203;
sig2=5.8e7;
%Resonance frequency of coupled Sensor, s1 is skin depth
freq=3.266e6;
w=2*pi*freq;
s1=1.0/sqrt(pi*freq*u0*sig1);
re1=(2*pi*n1*r1)/(2*pi*rw1*s1*sig1);
s2=1.0/sqrt(pi*freq*u0*sig2);
re2=(2*pi*n2*r2)/(2*pi*rw2*s2*sig2);
re1
re2
%self-inductance interrogator coil
k1=(4*r1*(r1-rw1))/((2*r1-rw1)*(2*r1-rw1));
k=sqrt(k1);
[ke,ee]=ellipke(k1);
l1=((2/k-k)*ke-(2/k)*ee);
ind1=n1*n1*u0*sqrt(r1*(r1-rw1))*l1;
ind1
%self-inductance sensor coil
k1=(4*r2*(r2-rw2))/((2*r2-rw2)*(2*r2-rw2));
k=sqrt(k1);
[ke,ee]=ellipke(k1);
l1=((2/k-k)*ke-(2/k)*ee);
ind2=n2*n2*u0*sqrt(r2*(r2-rw2))*l1;
%Calculation of self-inductance both interrogator and sensor coil in
another method
ind1;
mm1=n1*n1*u0*r1*(log (8*r1/rw1)-2);
mn1=n1*n1*u0*pi*r1/2;
ind2;
mm2=n2*n2*u0*r2*(log (8*r2/rw2)-2);
mn2=n2*n2*u0*pi*r2/2;
```

```
%Calculation of mutual inductance
for j=1:8
dist=d(1,j);
drm(1,j)=dist;
k1=(4*r1*r2)/(dist*dist+(r1+r2)*(r1+r2));
k=sqrt(k1);
[ke,ee]=ellipke(k1)
mfe=((2/k-k)*ke-(2/k)*ee);
mut=n1*n2*u0*sqrt(r1*r2)*mfe
mm(j)=mut
m2(j)=mut*mut;
% when r1<<d, then the above formula reduced to the following one
mmapp(j)=n1*n2*(u0*pi*r1*r1*r2*r2)/(2*dist*dist*dist)
l1rm(j)=ind1;
l2rm(j)=ind2;
end
Lm1=m2/m2(1)
Lm=mm/mm(1)
%for i=1:6
%logms(i)=loglog(Lm1(i))
%logz(i)=loglog(znorm(i))
%end
logms=log(Lm1)
logz=log(znorm)
%calculation of coupling factor using measured and calculated
inductance
CF=mm/sqrt(ind1*ind2)
CF=mm/sqrt(3.32e-06*63.25e-06)

% normalized Coupling factor
Coupling =CF/CF(1)
plot(drm*100,logms,'Red--o',drm*100,logz,'Black--*')
hleg1 = legend ('Normalized Received Signal w.r.t signal at
7cm','Normalized calculated M^2','Location','East');
xlabel('Separation distance between sensor &Interrogator coil (cm)')
ylabel('Normalized Received Signal (log scale)')
```

References

1. Abu Yousef, A., Pasupathy, P., Wood, S. L., & Neikirk, D. P. (2010). Resonant sensors for detecting corrosion in concrete bridges. *Transportation Research Record,* (2201), 19-26. doi: 10.3141/2201-03
2. Alamin, M., Gui, Y. T., Andrews, A., & Jackson, P. (2012). Corrosion detection using low-frequency RFID technology. *Insight-Non-Destructive Testing and Condition Monitoring, 54*(2), 72-5. doi: 10.1784/insi.2012.54.2.72
3. Andrade, C., Alonso, C., & Goni, S. (1993). Possibilities for electrical resistivity to universally characterise mass transport processes in concrete.*2*, 1639-1639.
4. Andringa, M. M., Neikirk, D. P., Dickerson, N. P., & Wood, S. L. (2005). Unpowered wireless corrosion sensor for steel reinforced concrete. *Sensors, 2005 IEEE,* 4 pp. doi: 10.1109/ICSENS.2005.1597659
5. Apostolopoulos, C. A., & Papadakis, V. G. (2008). Consequences of steel corrosion on the ductility properties of reinforcement bar. *Construction and Building Materials, 22*(12), 2316-2324. doi: 10.1016/j.conbuildmat.2007.10.006
6. Apblett, A. W. and Materer, N. F.(2010). Passive wireless corrosion sensor US Patent Specification *7675295 B2*
7. Arup, H. In: AP Crane editor (1983). Corrosion of reinforcement in concrete construction. *London, UK, 151*
8. ASTM C 876-91. (2006). Standard test method for half-cellpotentials of uncoated reinforcing steel in concrete Annual Book of ASTM Standards. vol 03.02, pp 11–6
9. Berg, A., Niklasson, G. A., Brantervik, K., Hedberg, B., & Nilsson, L. O. (1992). Dielectric properties of cement mortar as a function of water content. *Journal of Applied Physics, 71*(12), 5897-903. doi: 10.1063/1.350488
10. Berke, N.S., Hicks, M. in: V. Chaker (Ed.) (1992). Corrosion forms and control for infrastructure. *V.Chaker editor, ASTM STP 1137, American Society of Testing and Materials, Philadelphia,* 207

11. Bertolini, L., Carsana, M., & Pedeferri, P. (2007). Corrosion behaviour of steel in concrete in the presence of stray current. *Corrosion Science, 49*(3), 1056-68. doi: 10.1016/j.corsci.2006.05.048
12. Bhadra, S., (2010). Coupled Resonant Coil Sensors for Remote Passive Monitoring Applications. Unpublished master's thesis for master's degree, University of Manitoba, Winnipeg, MB, Canada
13. Bhadra, S., Bridges, G. E., & Thomson, D. J. (2010). Coupled coil sensor for detecting surface corrosion on steel reinforcement. *2010 14th International Symposium on Antenna Technology and Applied Electromagnetics and the American Electromagnetics Conference (AMEREM/ANTEM 2010),* 4 pp. doi: 10.1109/ANTEM.2010.5552503
14. Bhadra, S., Bridges, G. E., Thomson, D. J., & Freund, M. S. (2011). Electrode potential-based coupled coil sensor for remote pH monitoring. *Sensors Journal, IEEE, 11*(11), 2813-2819. doi: 10.1109/JSEN.2011.2170563
15. Bhadra, S., Thompson, E., Kordi, B., Bridges, G. E., & Thomson, D. J. (2010). Coupled resonant coil sensors with increased interrogation distance. *5th International Conference on Bridge Maintenance, Safety and Management, IABMAS 2010, July 11, 2010 - July 15,* 138-144.
16. Broomfield, J. P., Langford, P. E., Ewins, A. J. In: Berke N S , Chaker, V. and Whiting, D. editors (1990). Corrosion rates of steel in concrete. *ASTM STP 1065, Philadelphia, USA157*
17. Cabrera, J. G. (1996). Deterioration of concrete due to reinforcement steel corrosion. *Cement and Concrete Composites, 18*(1), 47-59. doi: 10.1016/0958-9465(95)00043-7
18. Carino, N. J. & Clifton J.R. (1995). Prediction of Cracking in Reinforced Concrete Structures. Building and Fire Research Laboratory
19. Chan, R.W. M., Ho, P.N. L., & Chan, E.P. W. (1999). Concrete Admixtures for Waterproofing Construction. Retrieved August 8, 2013, from http://www.archsd.gov.hk/media/11756/c315.pdf
20. Chemical formula. Retrieved August 15, 2013, from http://www.chemicalformula.org/rust

21. File:Qew bruecke nf beton kaputt 44 von 46.jpg , Retrieved from November 27 , 2013, from http://commons.wikimedia.org/wiki/File:Qew_bruecke_nf_beton_kaputt_44_von_46.jpg
22. Dielectric Constants of Various Materials Table. Retrieved from August 15, 2013, from http://www.csgnetwork.com/dieconstantstable.html
23. Du, R., Hu, R., Huang, R., & Lin, C. (206). In situ measurement of cl- concentrations and pH at the reinforcing steel/concrete interface by combination sensors. *Analytical Chemistry, 78*(9), 3179-3185. doi: 10.1021/ac0517139
24. Elsener, B., Molina, M. and Bonhi, H. (1993). Corros Sci. 35, 1563
25. Elsener, B., Bonhi, H. In: Berke N S , Chaker, V. and Whiting, D. editors (1990). Corrosion rates of steel in concrete. *ASTM STP 1065 Philadelphia ,USA, 143*
26. Elsener, B., Klinghoffer, O., Frølund, T., Rislund, E., Schiegg, Y. and Böhni, H. (1997). Assessment of reinforcement corrosion by means of galvanostatic pulse technique. *Proceedings of the International conference on Repair of concrete structures, from theory to practice in a marine environment*, Svolvaer, Norway, May 1997, 391-400
27. El-Shazly, A.H.,Wazzan, A.A & Radain, T.A.(2012). Investigation for the Possibility of Improving the Reinforced Concrete Corrosion Resistance Using Polyaniline Coated Steel. *Int. J. Electrochem. Sci.*, 7 , 2416 - 2429
28. Ervin, B. L., & Reis, H. (2008). Longitudinal guided waves for monitoring corrosion in reinforced mortar. *Measurement Science & Technology, 19*(5), 055702 (19 pp.). doi: 10.1088/0957-0233/19/5/055702
29. European Federation of Corrosion. Retrieved August 15, 2013, from http://www.efcweb.org/Working+Parties/WP+Corrosion+of+Steel+in+Concrete/WP+11+History.html
30. Feliu, S., Gonzalez, J.A., Feliu, S. Jr. and Andrade, C. (1989). *Brit. Corros. J. 24, 195.*
31. Galvanic Corrosion. Retrieved August 15, 2013, from http://www.surface.mat.ethz.ch/education/courses/surfaces_interfaces_and_their_applications_II/SIandAII_Ch5_Galvanic_corrosion
32. Glass, G., Page, C. and Short, N. (1991). *Corros. Sci. 32, 1283.*

33. Gurten, A. A., Kayakirilmaz, K., & Erbil, M. (2007). The effect of thiosemicarbazide on corrosion resistance of steel reinforcement in concrete. *Construction & Building Materials, 21*(3), 669-76. doi: 10.1016/j.conbuildmat.2005.12.010
34. Halamickova, P., Detwiler, R. J., Bentz, D. P., & Garboczi, E. J. (1995). Water permeability and chloride ion diffusion in Portland cement mortars: Relationship to sand content and critical pore diameter. *Cement and Concrete Research, 25*(4), 790-802. doi: 10.1016/0008-8846(95)00069-O
35. Heidari, M., & Azimi, P. (2011). Conductivity effect on the capacitance measurement of a parallel-plate capacitive sensor system. *Research Journal of Applied Sciences, Engineering and Technology, 3*(1), 53-60.
36. Honig, W.M. (1965). Wireless passive biological telemetry system. United States Patent Office, US Patent number 3,218,638
37. Hope, B.B., Ip, A.K., and Manning, D.G. (1985). *Cem. Conc. Res.* 15, 525.
38. Hope, B. B. ,Nmai, C. K. et al. (2001). Protections of Metals in Concrete Against Corrosion. *American Concrete Institute(ACI) 222R-01*
39. Hussain, S.E., Rasheeduzzafar, M., Al-Musallan, A. and Al-Gahtani, A.S. (1995). *Cem. Conc. Res.* 25, 15.
40. J.E.I. METALLURGICAL, INC. Retrieved August 8, 2013, from http://www.metallurgist.com/html/DefinitionsR-S.htm
41. Koch, G. H, Brongers, M. P. H., Thompson, N. G., Virmani, Y. P. and Payer, J. H. (2002) Corrosion Costs and Preventive Strategies in the United States. FHWA-RD-01-156
42. Leon-Salas, W., Kanneganti, S., & Halmen, C. (2011). Development of a smart RFID-based corrosion sensor. *Sensors, 2011 IEEE,* 534-537. doi: 10.1109/ICSENS.2011.6127274
43. Materer, N., Apblett, A., & Ley, T. (2011). Passive, wireless corrosion sensors for transportation infrastaructure Oklahoma Transportation Center *OTCREOS7.1-34-F*
44. MG Chemicals. Black Epoxy 832B. Retrieved August 12, 2013, from http://www.mgchemicals.com/products/protective-coatings/epoxy-potting-and-encapsulating-compounds/black-epoxy-832b/

45. Montemor, M. F., Simoes, A. M. P., & Ferreira, M. G. S. (2003). Chloride-induced corrosion on reinforcing steel: From the fundamentals to the monitoring techniques. *Cement and Concrete Composites, 25*(4-5), 491-502. doi: 10.1016/S0958-9465(02)00089-6
46. Morris, W., Vico, A., Vazquez, M.,& De Sánchez, S.R. (2002). *Corros. Sci. 44, 81*
47. Ong, J. B., You, Z., Mills-Beale, J., Ee, L. T., Pereles, B. D., & Keat, G. O. (2008). A wireless, passive embedded sensor for real-time monitoring of water content in civil engineering materials. *IEEE Sensors Journal, 8*(12), 2053-8. doi: 10.1109/JSEN.2008.2007681
48. Pasupathy, P., Zhuzhou, M., Neikirk, D. P., & Wood, S. L. (2008). Unpowered resonant wireless sensor nets for structural health monitoring. *2008 IEEE Sensors,* 697-700. doi: 10.1109/ICSENS.2008.4716537
49. Perveen, K., Bridges, G. E., Bhadra, S., & Thomson, D. J. (2013). An embedded inductively coupled printed circuit board based corrosion potential sensor. *Instrumentation and Measurement Technology Conference (I2MTC), 2013 IEEE International,* 22-26. doi: 10.1109/I2MTC.2013.6555373
50. PMMA. Retrieved from August 15, 2013, from http://www.pmma-online.eu/
51. Portland Cement Association. Retrieved August 15, 2013, from http://www.cement.org/tech/cct_dur_corrosion.asp
52. Reinforced concrete. Retrieved from August 15, 2013, from http://www.britannica.com/EBchecked/topic/496607/reinforced-concrete
53. Resonant inductive coupling. Retrieved from August 11, 2013, from http://en.wikipedia.org/wiki/Resonant_inductive_coupling
54. Riistama, J., Aittokallio, E., Verho, J., & Lekkala, J. (2010). Totally passive wireless biopotential measurement sensor by utilizing inductively coupled resonance circuits. *Sensors and Actuators: A Physical, 157*(2), 313-21. doi: 10.1016/j.sna.2009.11.038
55. Roberts, M. H. (1981). Carbonation of Concrete Made with Dense Natural Aggregates, *Publication Ip6/81, Building Research Establishment*

56. Robinson, M. P., & Clegg, J. (2005). Improved determination of Q-factor and resonant frequency by a quadratic curve-fitting method. *Electromagnetic Compatibility, IEEE Transactions on, 47*(2), 399-402. doi: 10.1109/TEMC.2005.847411
57. Salit Steel. Grades of Stainless Rebar. Retrieved August 12, 2013, from http://stainlessrebar.com/stainless-rebar-is-cost-effective/types-of-stainless-steel-rebar/
58. Samson, E., Maleki, K., Marchand, J., & Zhang, T. (2008). Determination of the water diffusivity of concrete using drying/absorption test results. *Journal of ASTM International, 5*(7), JAI101322 (12 pp.). doi: 10.1520/JAI101322
59. Sharmistha Bhadra and Douglas J Thomson and Greg, E. Bridges. (2013). A wireless embedded passive sensor for monitoring the corrosion potential of reinforcing steel. *Smart Materials and Structures, 22*(7), 075019.
60. Song, H-W. and Saraswathy, V. (2007). Corrosion monitoring of reinforced concrete structures—a review. *Int. J.Electrochem. Sci. 2 1–28*
61. Tang, W., He, X., Pan, T., & Chow, Y. L. (2006). Synthetic asymptote formulas of equivalent circuit components of square spiral inductors. *Journal of Electromagnetic Waves and Applications, 20*(2), 215-26. doi: 10.1163/156939306775777206
62. Tang, W. C., & Chow, Y. L. (2002). Inductance formula of a square spiral inductor on grounded substrate by duality and synthetic asymptote. *Proceedings of 2002 International Microwave Symposium (MTT 2002), , 3* 2069-72. doi: 10.1109/MWSYM.2002.1012276
63. Tang, W. C., & Chow, Y. L. (2002). Simple CAD formula for inductance calculation of square spiral inductors with grounded substrate by duality and synthetic asymptote. *Microwave and Optical Technology Letters, 34*(2), 93-6. doi: 10.1002/mop.10383
64. Tang, W., Zhu, Y., & Chow, Y. L. (2006). Inductance calculation of spiral inductors in different shapes. *2005 Asia-Pacific Microwave Conference,* 3 pp.
65. Tesche, F. M., Ianoz, M. V. and Karlsson, T. (1997). *EMC AnalysisMethods and Computational Models*. New York: John Wiley& Sons Inc.
66. Thomson, D. J., Perveen, K., Bridges, G. E., & Bhadra, S. (2012). Inductively coupled corrosion potential sensor for steel reinforced concrete with time domain gating interrogation. *Sensors and Smart Structures Technologies for Civil, Mechanical, and Aerospace Systems 2012, 8345* 83454P (7 pp.). doi: 10.1117/12.921332

67. Virginia Technologies, Inc. *Embedded Corrosion Instrument*. Retrieved August 12, 2013, from http://www.vatechnologies.com/eciAdvances.htm

68. Watters, D.G. , Jayaweera P., Bahr ,A. J., Huestis, D. L., Priyanhta ,N., Meline, R., Reis R. and Parks, D. (2003). Smart Pebble™: wireless sensor for structural health monitoring of bridge decks. *Proc. SPIE 5057 20–719*

69. Yin, X., Hutchins, D. A., Diamond, G. G., & Purnell, P. (2010). Non-destructive evaluation of concrete using a capacitive imaging technique: Preliminary modelling and experiments. *Cement and Concrete Research, 40*(12), 1734-43. doi: 10.1016/j.cemconres.2010.08.015

70. Young, J. F. (1988). A Review of the Pore Structure of Cement Paste and Concrete and its Influence on Permeability. *Permeability of Concrete, SP-108, American Concrete Institute*, 1-18.

71. Yu, H., Chiang, K. -. K., & Yang, L. (2012). Threshold chloride level and characteristics of reinforcement corrosion initiation in simulated concrete pore solutions. *Construction & Building Materials, 26*(1), 723-9. doi: 10.1016/j.conbuildmat.2011.06.079

72. Zhang, Y., Forsyth, M., Hinton, B. & Wallace, G. (2011). Control of biodegradation of a MG alloy in simulated body fluid. *18th International Corrosion Congress 2011, USA: Australasian Corrosion Association,* 1813-1820